Aluminum matrix nanocomposites for applications in automobile industry

Binghua Ma

Sorbonne Université

Ecole doctorale 397 - Physique et Chimie des Matériaux

Laboratoire de Chimie de la Matière Condensée de Paris

NANOPARTICULES DANS DES MATRICES METALLIQUES POUR DES APPLICATIONS EN AUTOMOBILES

Aluminum matrix nanocomposites for applications in automobile industry

Par **Binghua MA**

Thèse de doctorat de Physique et Chimie Matériaux

Présentée et soutenue publiquement le 27 Mai 2021

Devant un jury composé de :

M. Dirrenberger Justin	Maître de conférence (PIMM, CNAM)	Rapporteur
Mme. Tréguer-Delapierre Mona	Professeure (ICMCB, Université de Bordeaux)	Rapportrice
Mme. Courty Alexa	Professeure (Monaris, Sorbonne Université)	Examinatrice
M. Mazerolles Léo	Directeur de recherche CNRS (ICMPE)	Examinateur
M. Portehault David	Chargé de recherche CNRS (LCMCP, Sorbonne Université)	Directeur de thèse
M. Delalande Stéphane	Ingénieur de recherche (Stellantis)	Co-directeur de thèse
M. Sanchez Clément	Professeur émérite (LCMCP, Collège de France)	Co-directeur de thèse

Table of contents

General introduction

In the last 20 years, the key importance of energy and environmental challenges has paved its way to vehicle consumers. They are becoming more and more aware of environmental issues and are looking for cleaner vehicles. In parallel with the customer's desire, accelerated regulatory constraints on CO_2 emissions and pollutants (such as CO, NO_2) for new vehicles came into force in order to reduce greenhouse gas emissions. In this context, light-weight and electrical vehicles-related materials are one of the most important trends for the development of materials in the transportation sector.

This PhD work aimed at exploring novel metal matrix nanocomposites fabricated by ultrasound-assisted casting techniques to address automotive-related issues: mechanical enhancement and thermal management, with specific emphasis on the processing parameters for the dispersion ability and the interaction between nanosized-inclusion and metal matrix.

Aluminum and its alloys have been largely used in many industrial fields because of their excellent properties, such as lightweight, low cost, good thermal properties and high ductility. But the poor stiffness, strength, and wear properties still limit their applications as vehicle materials. Metal matrix composites are a class of metallic materials containing reinforcements and that can be traced back to the 1970s. Nanoparticles could be applied in a similar manner to enhance the mechanical properties of aluminum-based matrices by the design of metal matrix nanocomposites, which will be discussed in chapter 1. In the same chapter, the mechanisms behind the improved properties of nanocomposites will also be described. Then the techniques used to fabricate metal matrix nanocomposites will be further discussed.

Chapter 2 will present the synthesis and characterization of building blocks for the preparation of nanocomposites for thermal management: core-shell $Bi@SiO_2$ nanoparticles obtained by sol-gel synthesis. Our efforts for decreasing the aggregation state of Bi nanoparticles in silica shell will be presented, including ligand exchange at the surface of Bi nanoparticles. These particles will be used as building blocks of composites in chapter 4.

The incorporation of stiffer and harder reinforcement materials leads to aluminum metal matrix composites combining the properties of both the matrix and the reinforcement phase. Considerable efforts have been deployed to incorporate commercial nanoparticles into metal

matrices. Many recent chemical synthesis methods have widened the range of accessible nanoparticles, especially for boron-based phases, which are interesting for vehicle applications due to their light weight and hardness. Their application as metal matrix inclusions is studied and will be discussed in chapter 3. This chapter will present the fabrication and characterization of HfB_2-Al and SiC-Al nanocomposites. It will present in detail the original set-up we have designed, based on ultrasound-assisted casting, in order to increase the dispersion of nanoparticles in aluminum-based matrices. In the same chapter, the microstructure evolution with different experimental parameters is determined and the mechanical properties of these composites are evaluated by microindentation and nanoindentation tests.

While electrical vehicles are promising systems and have increased market share since several years, the research on the thermal management of battery packs is still in need. Among classic cooling methods, phase change material is a passive strategy relying on heat absorption through melting. Several recent developments focused on metal matrix nanocomposites with phase change materials as inclusions, which are of great interest due to their high thermal conductivity, high mechanical properties and wide working temperature range. Conventional strategies including powder metallurgy and bottom-up fabrication require high fabrication costs. At the operational level, we investigated the liquid phase method: metallic nanoparticles were encapsulated in a shell of SiO_2 to prevent destruction of the particles and macroscopic phase separation. Subsequently, these nanoparticles are incorporated in the molten metal matrix by the ultrasound-assisted process developed in chapter 3. This whole part will be presented in chapter 4, which encompasses the synthesis of phase change nanocomposites, the study of the reactivity occurring at the nanoparticles-matrix interface, and the assessment of the heat absorption ability of the resulting composites.

Overall, this work opens new perspectives for the application of ultrasound-assisted casting to the fabrication of mechanically reinforced and phase change metallic materials that could be potentially applied to fabricate vehicle components. We have also identified specific difficulties in reaching high dispersion of boron-based nanoparticles in aluminum matrices, thus identified future tracks to explore in order to achieve metal matrix nanocomposites with high homogeneity at the nanoscale for a wide range of reinforcement nanomaterials.

Chapter 1

Bibliography and state-of-the-art

This first chapter focuses on bibliographic aspects. First, the notion of metal matrix nanocomposites and their actual/potential applications in the automotive industry are presented. Then, the interest shifts toward two potential applications, mechanical reinforcement and heat management, with overviews of the existing techniques and solutions. Finally, the fabrication methods for nanocomposites are briefly presented.

1.1 Context

Composite materials consist of two or more constituents with different physical and/or chemical features. They can exhibit properties superior to each of the components and to their sum, thanks to so-called synergistic effects.[1] The major constituent is regarded as the matrix phase, and the remaining is called the reinforcement phase(s).[2] Often, the reinforcement phase is stronger, harder and stiffer than matrix phase, enabling improvement of the properties of the matrix. Commonly, composite materials are divided into three main types according to the matrix phase: polymer matrix composites,[3,4] metal matrix composites (MMCs)[5,6] and ceramic matrix composites.[7,8] Especially, MMCs have attracted lots of attention due to their superior properties and wide applications range from aerospace, to automobile industry and to defense.

1.1.1 Metal matrix composites

Metal matrix composites (MMCs) are a class of metallic materials containing reinforcement phase(s) that can be traced back to the 1970s. Researchers managed to improve properties of metals/alloys with ceramic reinforcements by stir casting, rheocasting and powder metallurgy.[9,10] For MMCs, three main types of reinforcement materials can be distinguished: continuous fiber networks and discontinuous reinforcement materials as particles or whiskers[11] (Figure 1.1). Compared to continuous reinforcement, the discontinuous one presents advantages of lower cost and isotropic properties. Generally, there are two main types of reinforcement phases used for MMCs: (a) ceramic reinforcements, such as Al_2O_3,[12,13] SiC,[14,15] TiC,[16] B_4C,[17] and (b) carbon-based materials like graphite, fly ash, etc. To fabricate MMCs, aluminum,[2,18] magnesium,[19,20] titanium[21] and copper[22] are widely used as matrix phases.

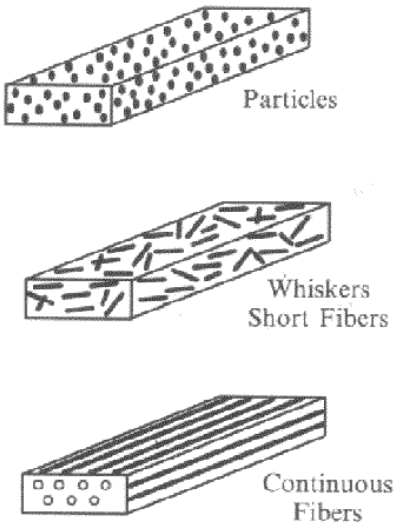

Figure. 1.1 Three types of reinforcement in MMCs[11]

As mentioned above, reinforcement with metallic or ceramic phases can improve hardness of the composite versus the sole matrix, enabling the material to withstand higher load but also providing additional specific properties. The incorporated reinforcement objects could be microsized or nanosized. Micron-scale reinforcement in the metal matrix has been well studied and demonstrated to provide high hardness, elastic modulus, and strength.[23] Reducing the size of the inclusions to the nanoscale brings additional advantages: reduced load (5 to 20% for macroscale reinforcements vs. lower than 5% for nanoscale ones) and increased strength by Orowan hardening and pinning of grain boundaries.[24] Hence, metal matrix nanocomposites (MMNCs) possess in general properties superior to those of composites with microscale reinforcement. Nanoscaled reinforcement materials for MMNCs include graphene, carbon nanotubes and nanofibers, and nanoparticles (such as Al_2O_3, SiO_2, SiC, TiO_2).[5,6]

1.1.2 How can aluminum matrix nanocomposites improve sustainability in the automotive industry?

A new form of mobility represented by the ACER concept (Autonomous, Connectivity, Electrification and Ridesharing) has shifted dramatically the market in the past few years. Based on the latest legislation and current trends dealing with clean vehicles and carbon neutrality, automotive industries have integrated sustainability into their strategy. In this context, the research of light-weight, tough, and functional materials has a growing significance.

The application of nanocomposites for the design of automotive components reflects the search for improved production rate and thermal stability, weight reduction, and less wear parts. All these features contribute to a reduction of CO_2 emissions and of environmental impact. Most of them also enable an increase of the cruising time, which is of great importance in the case of electric vehicles.[25]

Light (density < 2.7 $g \cdot cm^{-3}$) and tough (tensile strength > 350 MPa) aluminum MMNCs are especially interesting for automobile applications. Aluminum and its alloys are already largely used in many industrial fields because of their light weight, low cost, good thermal stability and high ductility. But their poor stiffness, strength, and wear properties still limit their applications.[2] These drawbacks can be circumvented by the design of aluminum metal matrix composites with the addition of reinforcement materials stiffer and harder than aluminum and its alloys.

Apart from traditional mechanical reinforcement, metal matrix nanocomposites can also acquire properties specific to the inclusion nanoparticles. A typical application deals with thermal management of batteries.[26] The combination of phase change inclusion particles and aluminum matrix leads to bifunctional materials with heat management properties and good thermal dissipation.[27] These properties will be detailed in the next chapters.

1.2 Mechanical property improvement

Enhanced mechanical properties is one of the main pursuits for MMNCs fabrications. Below, we present possible strengthening mechanisms and strategies to improve mechanical properties.

1.2.1 Strengthening mechanisms

Most of the work on metal matrix nanocomposites focuses on the improvement of mechanical properties: hardness, rigidity and wear resistance.[23] As the major component, the metallic matrix provides ductility. Its properties depend on the polycrystallinity of its microstructure. Indeed, grain boundaries strengthen the material by acting as barriers to the dislocation movement.

The enlisted strengthening mechanisms for MMNCs encompass load transfer effect, Hall-Petch strengthening, Orowan strengthening, coefficient of thermal expansion (CTE) and elastic modulus (EM) mismatch.[24]

Load transfer effect corresponds to direct strengthening by transferring of the load from the matrix to the reinforcement nano-objects. The reinforcement material is harder than the matrix, thus contributing to strengthening of the overall material. Nardone and Prewo[28] proposed a modified Shear lag model to explain the effect of load transfer on mechanical properties. Since the volume fraction of the reinforcement particles is small, load transfer is small as well. For isotropic particles, the model can be simplified to yield the equation[29] below:

$$\Delta s_{LT} = \frac{1}{2} v_P s_m \quad (1)$$

Where v_P and s_m are the particle volume fraction and the yield strength of the un-reinforced matrix, respectively.

Orowan strengthening. This effect is based on the interaction between nanoparticles and dislocations. It can be ignored for particles with a diameter larger than 1 μm.[30] Dislocations tend to bend around particles and to form dislocation loops with dislocations on the other side

of the particles. These dislocation loops are then pinned onto the nanoparticles, which leads to enhanced strength. At same volume fraction, smaller particles contribute to the higher enhancement of final strength. This effect can be expressed as the equation[31,32] below:

$$\Delta s_{OR} = \frac{0.13 b G_m}{d_p[\left(\frac{1}{2v_p}\right)^{\frac{1}{3}} - 1]} \ln \frac{d_p}{2b} \quad (2)$$

where b, G_m, d_p and v_p are the Burgers vector, shear modulus, particle average diameter and particle volume fraction, respectively. For example, Cao et al.[33] applied ultrasound-assisted casting to fabricate AlN reinforced magnesium alloy AZ91D that exhibited a yield strength of 144 MPa compared to 100 MPa for the nonreinforced alloy. The author ascribed this 44% increase to the Orowan strengthening and the effect of the particles decreasing (or refining) the matrix grain size (see below), contributing to 35.8 MPa and 8.2 MPa, respectively.

Hall-Petch strengthening. The improvement of strength is also related to decreased grain size since grain boundaries hinder dislocation movements.[24] The relationship between grain size (d) and yield strength (Δs_{H-P}) is expressed through the Hall-Petch equation:[34]

$$\Delta s_{H-P} = \frac{k_y}{\sqrt{d}} \quad (3)$$

where k_y is the strengthening coefficient. From equation (3), we can clearly see that the yield strength of nanocomposite is inversely correlated to the grain size. This is true for particle sizes above *ca.* 10 nm. Below, the inverse Hall Petch effect prevails, leading to an opposite dependence versus the grain size.[35] Hence, an optimal grain diameter for Hall Petch hardening is ca. 10 nm.

The addition of particles results in a decrease of the grain size of the matrix through localization of the particles at the grain boundaries, which retards or stops matrix grain growth.[24] The Zener equation[35] shows the relationship between grain size (d_m), particle volume fraction v_p and particle diameter d_p:

$$d_m = \frac{4 a d_p}{3 v_p} \quad (4)$$

where a is a constant. Increasing the particle volume fraction and decreasing the particle size result in reduced grain size, thus leading to enhanced yield strength of metal matrix nanocomposites.

Coefficient of thermal expansion (CTE) and elastic modulus (EM) mismatching. After solidification of the composite, the temperature keeps decreasing to room temperature. Due to the difference of the coefficients of CTEs between the particles and the matrix, stresses are generated at the interface, leading to geometrically necessary dislocations (GND). GND can also generate from the difference of elastic modulus between particles and matrix during straining. The GND density due to CTE and elastic modulus can be calculated from the following equations:[35]

$$\rho^{CTE} = \frac{A?a?T v_p}{b d_p (1-v_p)} \tag{5}$$

$$\rho^{EM} = \frac{6 v_p}{p {d_p}^3} \varepsilon \tag{6}$$

where A is a geometric constant, Δa and ΔT are the differences of the CTE and of temperature, respectively, e is the bulk strain of the composite.

These models could be used to estimate the effect of different parameters of the composites. However, some critical factors are needed to make these models valid: a full density, good adhesion between the reinforcement particles and the matrix, and a uniform distribution of the particles. This is where the understanding and control of the process appear critical.

Plenty of materials have been commercially used as reinforcements. Among them, hard materials have often been chosen as reinforcement phase: covalent hard materials/diamond-like structure (C, CN_x, BN, SiC, AlN); metallic hard materials/metal like structure (TiC, TiN, AlB_2, WC, Ti_2N, TiAlCN…) and ionocovalent hard materials/ionic structure (Al_2O_3, ZrO_2…).[36]

Table 1.1 Commercially available nanoparticles used for reinforcement[37]

Base	Carbide	Nitride	Boride	Oxide
Aluminium		AlN		Al_2O_3
Antimony				Sb_2O_3
Boron	B_4C	BN		B_2O_3
Bismuth				Bi_2O_3
Cerium				CeO_2
Chromium	CrC	CrN	CrB	CrO_3, Cr_2O_3
Cobalt				CoO, Co_2O_3, Co_3O_4
Copper				CuO
Dysprosium				Dy_2O_3
Erbium				Er_2O_3
Europium				Eu_2O_3
Gadolinium				Gd_2O_3
Hafnium	HfC	HfN		HfO_2
Indium				In_2O_3
Iron				Fe_3O_4, Fe_2O_3
Lanthanum			LaB_6	La_2O_3
Magnesium				MgO
Manganese				MnO_2, MnO_3, Mn_2O_3
Molybdenum	MoC, Mo_2C	MoN, Mo_2N	MoB, Mo_2B	MoO_3
Neodymium				Nd_2O_3
Nickel				NiO, Ni_2O_3
Niobium				Nb_2O_5
Praseodymium				Pr_6O_{11}
Samarium				Sm_2O_3
Silicon	SiC	Si_3N_4		SiO_2
Tantalum	TaC	TaN		Ta_2O_5
Terbium				Tb_4O_7
Tin				SnO_2
Titanium	TiC	TiN	TiB_2	TiO_2
Tungsten	WC, W_2C	WN, W_2N	WB, W_2B	WO_3
Vanadium				VO, V_2O_3, V_2O_5
Yttrium				Y_2O_3
Ytterbium				Yb_2O_3
Zinc				ZnO
Zirconium	ZrC	ZrN	ZrB_2	ZrO_2

1.2.2 Strategies to improve mechanical properties

Several strategies have been used to improve the mechanical properties through the mechanisms detailed above, such as selecting suitable reinforcement materials and optimizing particle characteristics (such as size distribution, composition and interfacial bonding), which will be discussed in the following paragraph.

1.2.2.1 Selection of suitable reinforcements

Recent studies on MMNCs focus on the light metal matrix. Among metals, the light alloys of Al, Ti and Mg are desirable as metal matrix. Their properties depend on the reinforcement particle features, more precisely, their morphology, size, load fraction, as well as the quality of the interface with the matrix. Table 1.1 above listed some of the commercial nanoparticles for MMNCs. They can be categorized into several types:

a) Carbon allotropes

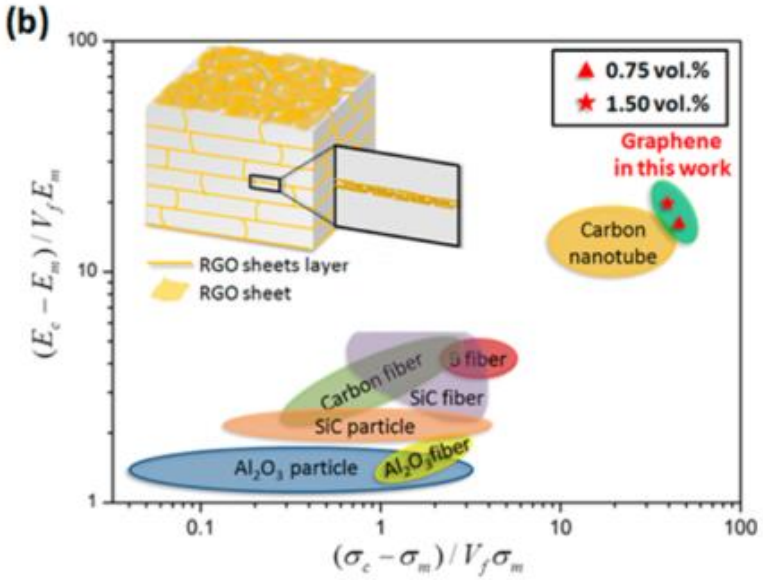

Figure 1.2. Strengthening and stiffening efficiencies of reduced graphene oxide in a reduced graphene oxide (RGO)/Al nanolaminated composite compared to other reinforcement materials in Al matrix composites[38]

Carbon nanotubes (CNTs) are among the most studied strengthening additives for MMC.[39] Their strong sp^2 bonds lead to high elastic stretching properties. For multi-wall carbon nanotubes, the theoretical elastic modulus can reach 600 and 1100 GPa while the tensile strength ranges from 35 to 110 GPa.[40] Bakshi and Agarwal[41] have reviewed the strengthening properties of CNT-Al composites. The record yield strength and elastic modulus are 621 MPa and 110 GPa, respectively.[41]

Other allotropes like nanodiamond and graphene have also been studied for their load-transfer ability and high thermal conductivity. Li et al.[38] fabricated a bulk reduced graphene oxide-reinforced Al matrix composites with nanolaminated microstructure. Compared with the unreinforced Al matrix, these composites showed significantly improved stiffness and tensile strength, with good yield strength (302 MPa) and elastic modulus (87 GPa) (Figure 1.2).

It should be noticed that for all carbon allotropes in Al matrix, a thin layer of Al_4C_3 could be formed by interfacial reaction, at the expense of the reinforcement objects. It then degrades the reinforcement objects but promotes load transfer.[40]

b) Oxides

Oxides like Al_2O_3, ZrO_2, TiO_2, ThO_2 are often added to metallic matrices to provide ductility and fracture toughness from the metallic matrix, creep resistance and high strength from the additives.[11]

c) Nitrides

Nitrides like nanoparticles of Si_3N_4[42] and microparticles of Fe_3N[43] have been investigated to improve mechanical properties. Recent work focused on layered boron nitride. BN nanotubes embedded in an Al matrix possess excellent elastic modulus (750–1200GPa), strength (61 GPa) and good chemical inertness (oxidation up to 950 °C). They strongly improve mechanical properties and thermal conductivity.[44] These values varied with the processing technique.

BN nanoparticles and microparticles have also been embedded in an Al matrix. With powder spark plasma sintering (SPS) and ball-milling, Firestein et al.[45] produced a BN-Al composite, with *in situ* formation of AlB_2 and AlN at the interface. Improved tensile strength of 170 MPa at 500 °C was achieved compared to a value of only 33 MPa for a pure Al sample produced by spark plasma sintering. A nanocomposite reinforced with large-sized cubic BN particles has also been fabricated by cold spray and shows improved abrasive wear resistance.[46]

d) Carbides

Carbides like TiC[47], SiC,[48,49] TaC, WC, B_4C[50] have been investigated by many researchers. SiC is one of the most common reinforcements for MMNCs because of its high strength, low thermal expansion, high thermal conductivity, high hardness, high elastic modulus, high chemical inertness, and its quite good wettability by the Al matrix. Li et al.[51] firstly prepared well mixed Al powder and 10 vol% SiC nanoparticles via ball milling, then hot pressure sintering and hot extrusion were applied sequentially to get an Al/SiC nanocomposite that showed ultrafine Al grains and intragranular SiC nanoparticles. Compared to pure Al alloy, the nanocomposite exhibited superior mechanical behavior as shown from the stress-strain curve (Figure 1.3). The yield strength and tensile strength are improved by 284% and 259%, respectively, compared to the pure Al alloy.

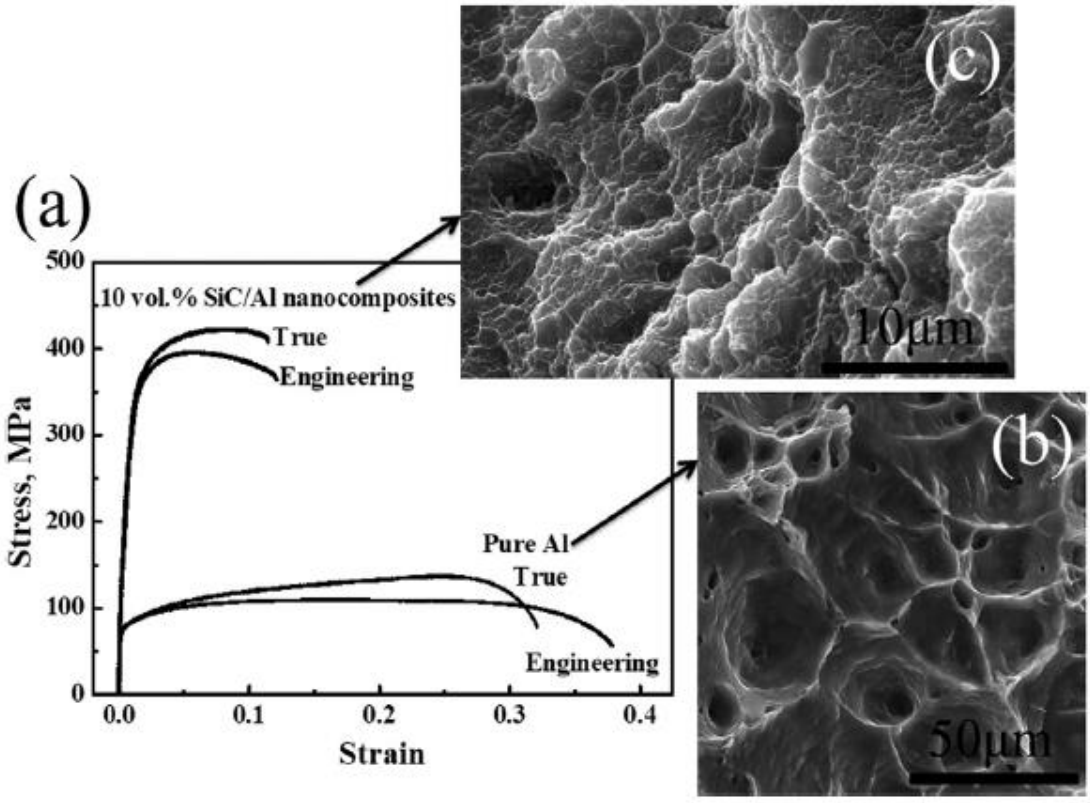

Figure 1.3. Stress-strain curves of a pure Al alloy and a 10 vol% SiC/Al alloy nanocomposite, (b) Fractograph of Al alloy, (c) Fractograph of the nanocomposite.[51]

e) Borides

Among all the ceramic particles used as reinforcements, titanium diboride (TiB_2) has attracted the interest of many researchers because of its excellent resistance to mechanical erosion, higher hardness (960 HV), high melting point (2790 °C) and good thermal stability. Besides, TiB_2 has been used as a grain refiner in Al alloys to suppress the growth of Al grains.[52]

Nanoparticles of TiB_2 about 31 nm diameter were used to reinforce Al by cryomilling and spark plasma sintering (SPS). The strength of the composite was improved by 20% compared with equivalent SPS-consolidated 5083 Al alloy.[52] Nampoothiri et al.[53] re-melted a TiB_2/Al composite prepared by powder metallurgy and treated it with ultrasound process. The sizes of the TiB_2 particles decreased after this treatment, yielding a two times increased yield strength compared to samples before treatment.

AlB_2[54] and ZrB_2[55] were synthesized by *in situ* reaction with boron and with a Al-K_2ZrF_6-KBF_4 system. For example, Tian et al.[55] introduced pre-dried salts (K_2ZrF_6 and KBF_4) wrapped in an aluminum foil into molten 2024 Al alloy to promote the *in situ* reaction in the molten salt between the different precursors. The formed ZrB_2 nanoparticles of ca. 30 to 100 nm were rectangular and were also uniformly distributed in the final composite. ZrB_2-reinforced nanocomposites exhibited higher tensile strength and yield stress.

f) Intermetallic materials

The review of Ward-Close and Doorbar[56] summarized the research on intermetallic matrices. Intermetallic compounds like NiAl and Al_3Ti[2457] have been successfully used as reinforcement phases in MMNCs. The Al–Al_3Ti nanocomposite revealed good mechanical behavior at high temperature, and TiAl–NiAl MMNCs showed low fracture toughness and high hardness.

g) Combination of several reinforcement particles

A combination of several reinforcement particles could produce a synergetic effect. For example, Sujan et al.[49] studied the performance of stir casted Al_2O_3 and SiC reinforced metal matrix composite material. The result showed that the composite materials exhibit improved physical and mechanical properties, such as low coefficient of thermal expansion as low as

4.6 $10^{-6}\cdot N^{-1}\cdot °C^{-1}$, high ultimate tensile strength increased by up to 23.68 %, high impact strength and hardness.

1.2.2.2 Optimized properties of reinforcement

a) Reinforcement uniformity into matrix phase

Non-uniform distribution of reinforcement objects is one of the main obstacles for enhanced mechanical properties.[58] Several techniques have been explored to circumvent this difficulty. Ultrasound-assisted casting is effective to reach an homogeneous dispersion of the reinforcement objects in the matrix phase.[14,59,60] Another method consists in enhancing the wettability of reinforcement objects by the matrix. Pourhosseini et al.[61] successfully modified Al_2O_3 nanoparticles via electroless deposition of Cu, Ni and Co and subsequently applied these particles to reinforce A356 alloy by stir casting. The wettability of the coated nanoparticles was enhanced, resulting in homogeneous distribution in the aluminum matrix. The final mechanical properties (such as microhardness and compressive strength) were then significantly improved, especially for composites encompassing Ni-coated Al_2O_3. Another method to reach dispersion focuses on the ability of the matrix to carry reinforcement objects. Mousavian et al.[62] managed to reinforce an A356 aluminum matrix with SiC ceramic nanoparticles by combining techniques of stir casting and semi-solid extrusion. The authors found that the addition of nickel acted provided a SiC carrier, leading to a uniform dispersion of particles into the aluminum matrix. In view of the mechanical property, the ultimate tensile strength and elongation of the final Al/SiC composite in presence of nickel could reach around 304 MPa and 5.8%, respectively, while the introduction of titanium decreased the elongation ratio.

b) Reinforcement particle size

The size of the reinforcement particles plays a critical role in the mechanical properties of MMCs. For example, a A356 alloy reinforced with nanoscaled TiB_2 possessed higher elongation and tensile strength than with microscaled particles.[63] Another example from Youssef El-Kady et al.[64] deals with alumina-reinforced A356 alloy. Rheocasting and squeeze casting were used to incorporate 60 and 200 nm Al_2O_3 nanoparticles into A356 alloy. The nanocomposite with 60 nm Al_2O_3 particles showed higher ultimate tensile strength, yield

strength and elongation compared to the composite with 200 nm Al_2O_3, while microhardness showed the opposite trend, probably because of the agglomeration of nanoparticles.

c) Volume fraction of the reinforcement phase

The content of reinforcement phase in the nanocomposite is also an important parameter to control the mechanical properties.[20,63–67] Reddy et al.[67] fabricated aluminum metal matrix nanocomposites reinforced by different contents of SiC nanoparticles of 55 nm diameter (0, 0.3, 0.5, 1.0 and 1.5 vol%) via microwave sintering and hot extrusion techniques. Increasing the SiC content from 0.3 to 1.5 vol% enhanced the final yield strength from 66 to 114 MPa, and the ultimate compressive strength from 313 to 392 MPa, respectively. A365/Al_2O_3 metal matrix nanocomposites also showed improved ultimate tensile strength, yield strength and elongation with particle size of 60 nm. However, the excessive incorporation of nanoparticles could be detrimental to mechanical properties. [64] Indeed, Akbari et al.[63] found that increasing the content of TiB_2 nanoparticles into A356 nanocomposites from 0.5 to 1.5 wt% significantly enhanced the final yield stress and ultimate yield strength, while an opposite trend appeared when the nanoparticle content kept increasing to 3.0 wt%. This behavior could be ascribed to increasing particle aggregation.

d) Interfacial bonding

A strong interface between the metal matrix and reinforcement objects is necessary to ensure effective load transfer.[68] Wang et al.[69] utilized reduced graphene oxide (RGO) to reinforce a Cu alloy (in presence of Ti) and found that a TiC layer was formed at the interface of RGO/CuTi composite. The TiC layer led to enhanced interfacial bonding enabling yield strength and tensile strength of 242 MPa and 307 MPa, 24 and 16% higher than those of 2 vol% RGO/Cu composite, respectively. Another example relates to the interface reaction between BN and Al that leads to the formation of AlN and AlB_2. [44] Their formation in Al-based composites is not as deleterious as compared with carbides (Al_4C_3).[70] AlN reinforcement improves the hardness and flexural strength of Al matrix. AlB_2 is also less detrimental to the fracture toughness of Al.[44]

As for the previously described parameters, a tradeoff value exists for interfacial bonding. Indeed, excessive interfacial bonding may deteriorate the mechanical properties of the composite. Zhang et al.[21] applied spark plasma sintering to fabricate Ti/nanodiamond nanocomposites and found the formation of the new phase TiC derived from the reaction between Ti and nanodiamond at the grain boundaries. Small amounts of *in situ* formed TiC was regarded as one of the main strengthening mechanisms since it is likely to induce dislocation pinning. However, larger amounts of TiC (≥ 0.5 wt% nanodiamonds) tended to decrease the mechanical properties of the final nanocomposite.

1.3 Phase change materials for thermal management of Li-ion battery

As mentioned above, MMNCs are potential light-weight materials for thermal control, which is essential for vehicle electrification based on lithium batteries technology. Below, we are presenting major strategies for thermal control of batteries together with a brief overview of phase change materials.

1.3.1 Importance of thermal management of the Li-ion battery

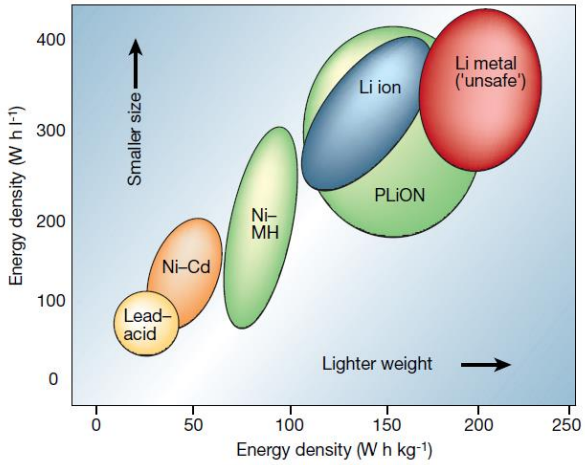

Figure 1.4 Energy volumetric and mass densities of different battery systems.[71]

Electrical vehicles (EVs) including hybrid electric vehicles, plug-in hybrid electric vehicles and battery electric vehicles focus lots of attention because of their ability to reduce greenhouse gas emissions.[72,73] One of the main challenges to develop EVs lies in the energy storage system. Lithium-ion batteries possess some advantages compared to other types of batteries, such as nickel–cadmium and nickel-metal hybrid batteries: a) higher energy density (Figure 1.4), b) higher specific power, c) lighter weight, d) lower self-discharge rates, e) higher recyclability and f) longer life cycle.[71,74] A full battery pack consists in several connected electrochemical cells (in series and/or in parallel).[71]

A traditional cell contains an anode (graphite), a cathode ($LiCoO_2$ layer), a separator and an electrolyte (Figure 1.5). On charging, the cobaltite is oxidized, leaving Li^+, which goes through the separator and inserts into the interlayer space of graphite, which then is reduced. The overall process implies an electric current and an electron transfer through the external circuit.[75] This reaction is reversed during discharge. However, the working temperature affects greatly the kinetics of these reactions, thus the performances, life and safety of Li-ion batteries. Furthermore, temperature changes of Li-ion battery due to environmental conditions and heat release from several cycles of charging and discharging are inevitable.[73] In Tesla's Model 3 car, the battery pack could release more energy (in form of heat) than 6000 iPhone handsets.[76] Therefore, battery thermal management is necessary. We focus below on management of overheating.

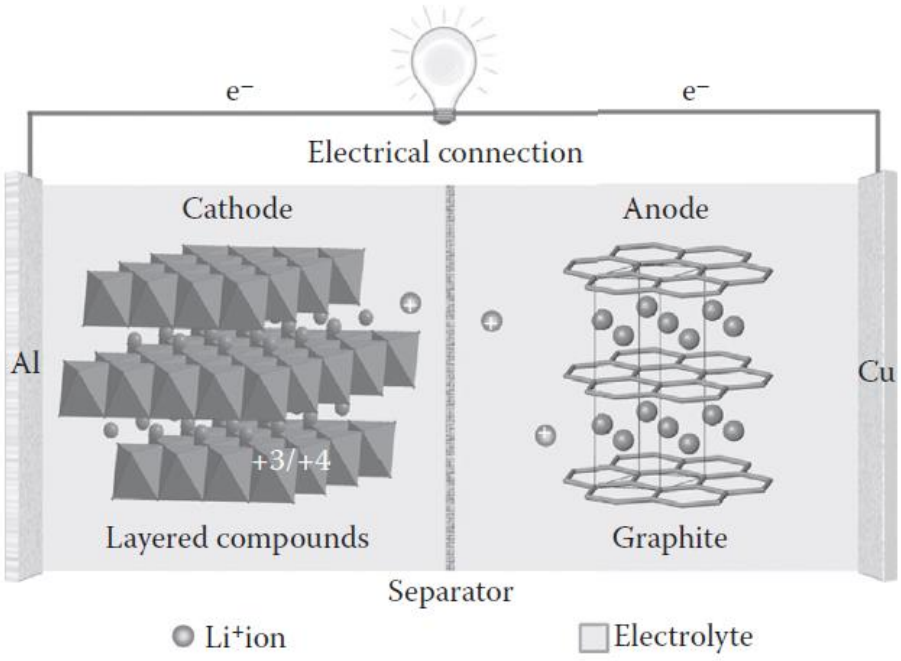

Figure 1.5 Scheme of a traditional Li-ion battery.[77]

Heat generation within Li-ion battery is derived from resistive dissipation, relaxation of the concentration gradient in the cell and chemical reaction.[27,73] It can be simply described as follows:

$$Q = A - B$$

$$A = I(U - V)$$

$$B = I(T\frac{dU}{dT})$$

Q, *A*, *B*, *I*, *U* and *V* are the heat generation rate, resistance loss in the cell, reversible entropic heat of the electrochemical reaction, electric current traveling through the cell, open-circuit voltage and the cell voltage of the Li-ion batteries, respectively.

1.3.2 Cooling strategies

The major role of battery thermal management is to maintain a suitable temperature range and evenly distributed temperature within battery during charging and discharging, even at extreme environmental conditions.[78] The most effective working temperature of Li-ion battery ranges from 15 to 40 °C.[79] That means that the battery should on one hand reduce its temperature when operating temperature increases or environmental temperature is high, on the other hand increase temperature when the environmental temperature is low. The battery thermal management system itself should be compact, light, cost-saving, reliable and easy to operate, to pack and to maintain for its application in electronic vehicles.[80,81] Battery thermal management system could be categorized according to a) medium type, b) power consumption and c) whether it directly contacts with battery or not.[73] Here, we are going to discuss medium-based cooling systems: air cooling, liquid cooling and phase change materials.

Air cooling. The simplest way to cool a battery is to blow air on the battery walls through a fan or a wind tunnel. In this case, during design of batteries, several parameters need to be taken into account, such as the battery layout, airflow or wind speed to minimize the energy consumption and costs. For example, Xu and He[82] improved heat dissipation by simply changing the longitudinal battery pack to a horizontal battery pack, which shortened the airflow path. Furthermore, they found that a double "U"-type duct enhanced heat dissipation performance rather than double "1" type. Around the battery, the air flow takes time to blow the whole system, leading to unevenly distributed thermal gradient. To solve this issue, bi-directional or reciprocating airflow has been implemented, which relies on cell temperature monitoring to actively adjust the airflow direction.

Liquid cooling. Although air cooling could achieve battery thermal management as described above, its efficiency is not sufficient to dissipate heat from an electric vehicle battery pack under a high charge/discharge rate at high working temperature, mostly because of the low thermal conductivity of air.[83,84,79] Thus researchers introduced liquid cooling that involves either direct immersion, or indirect circulation of thee liquid surrounding battery pack. Liquid cooling utilizes coolants such as water, acetone, glycol and oil, and has been proved 3500 times more efficient than air cooling.[85] A cold plate with built-in channels for liquid flowing could

be arranged surrounding battery cells and remove excess heat. Researchers also point out that channel design and geometries should be adjusted depending on the target applications. Cold plate with rectangular channels achieved 5% more heat transfer than one plate with elliptical channel design.[86]

Phase change materials. For air cooling and liquid cooling, an additional electrical source is needed and other accessories such as pump, blower and cold plate are necessary as well, leading to high costs. In this context, researchers have explored alternatives for battery thermal management: phase change materials. The phase change, mostly solid-to-liquid, of organic/inorganic/eutectic phase change materials could extract heat from batteries[87,88] and thus regulate the working temperature to a reasonable range. However, phase change materials (without fixing matrix) have low thermal conductivity and thus have slower regeneration time, which is not effective enough for fast charging-discharging cycles. Researchers have then explored different strategies to improve heat transfer: a) using fixed and non-moving surfaces, b) using phase change material composites, c) impregnating porous materials, and d) adding particles with high conductivity.[79] Li et al.[89] applied a sandwiched cooling element composed of copper metal foam saturated with phase change materials (paraffin) as thermal management for prismatic power batteries. As a control, pure paraffin enabled a dramatic reduction of battery surface temperature and maintained a suitable range of working temperature because of its latent heat absorption and of the natural convection of melted paraffin during melting event. A copper-paraffin composite could further reduce the surface temperature and enhance the uniformity of the distribution of temperature due to the improvement of thermal conductivity.

1.3.3 Metal matrix nanocomposite with phase change materials for temperature

Commonly used phase change materials – organics and salt hydrates – are restrained to applications at relatively low temperature and suffer from limited mechanical resistance, low stability upon cycling and low thermal conductivity. Researchers have incorporated thermally conductive fillers (such as graphite, metallic nanoparticles) and foams (metals and graphite, for instance) to produce phase change composites with improved thermal conductivity. The role of fillers is limited due to a discontinuous structure. Thermal interface resistance between phase

change materials and fillers still prevail. On the opposite, a continuous structure with high thermal conductivity could be obtained after incorporating phase change materials into foams.[90] Due to the difficulties of infiltration process and to corrosion, foams are difficult to implement for phase change materials with high melting temperature.[91] Metallic materials have been found applicable as phase change materials for their high thermal conductivity (~10 to 400 $W\ m^{-1}K^{-1}$), high melting temperature (-40 to 300 °C) and large enthalpy of fusion.[92] Metallic phase change materials are then good candidates for thermal management.

To our knowledge, the first documented work on metal matrix nanocomposites with phase change inclusions was published in the 1990s. Goswami et al.[93] have incorporated Bi into glassy Al-Fe-Si matrix by mixing Bi with the matrix through induction melt spinning. Nanocomposites containing Bi nanoparticles between 5 to 50 nm were achieved. This work was revisited in 2015, with the aim of improving the control of the nanoparticle size. Liu et al.[92] embedded Bi nanoparticles into an Ag matrix by directly adding the desired amount of Bi nanoparticles to molten Ag. The Ag matrix was found efficient to prevent coalescence of Bi nanoparticles and the phase change properties were stable even after 100 melt-freeze cycles. Compared to common organic phase change materials, the incorporation of Bi nanoparticles resulted in 50-100% improvement of thermal energy density. In addition, by tuning nanoparticle size from 8 to 15 nm, the melting temperature of the silver matrix was shifted from 236 to 252 °C. To convert into a less expensive aluminium metallic matrix, Abraham et al.[26] ball-milled a mixture of Al and Bi_2O_3. Subsequently, this pellet was heated and held over 300 °C to promote aluminothermic reduction of Bi_2O_3 and form an Al_2O_3 layer surrounding Bi particles within an Al matrix. The matrix encapsulating Bi inclusions could store thermal energy upon heat-freeze cycles and retained its structure. In the control sample with non-encapsulated Bi inclusions, molten Bi tended to separate from the Al matrix and to accumulate on the surface of materials.

1.4 MMCs fabrication techniques

Most manufacturing techniques for the synthesis of bulk metal matrix nanocomposites have already been reviewed in the literature among which we can cite the review of Bakshi et al.[39] as well as the latest review of Casati and Vedani[24]. Metal matrix composites/nanocomposites

can be produced by many techniques (Table 1.2) mainly composed of solid-state, liquid-state and semisolid-state processes.[2] In the following paragraphs, friction stirring, spark plasma sintering, ultrasound-assisted casting, vortex casting, squeeze casting bottom-up fabrication and electrodeposition are going to be discussed.

Table 1.2 Class and process techniques of powder metallurgy[10]

Class	Process technique	Exemples
Powder metallurgy	Mecanical alloying and sintering	Al/CNT
	Mecanical alloying and hot pressing	Al/Al_2O_3
	Spark Plasma Sintering	BN/Al
	Friction stir	Al/Al_2O_3
Melting and solification	Stir Casting	Al/CNT
	Melt infiltration	
	ultrasound-assisted casting	Al/SiC
	Disintegrate Melt Deposition (DMD)	Al/Al_2O_3
	Selective laser melting (LSM)	Ti/TiC
Semi-Solid Processes	rheocasting and squeeze casting	Al-A356/Al_2O_3
	semi-solid casting (SSC)	Zn-AC43A/β-SiC
Thermal Spray	Hot spraying	
	Cold spraying	nanodiamond –aluminum
Electrochemical and chemical reaction	Electro deposition	Cu/CNTs
	Chemical reaction	Ag/Bi

1.4.1 Powder metallurgy

Powder metallurgy includes all the production processes using metal powders as matrix precursor. It consists of three main steps: mixing metal matrix powders with the reinforcement

phase in the form of powders, consolidating the powders mixture, post-treating the mixture to trigger e.g. sintering.[94–96] The aluminum and/or reinforcement powders are obtained by ball milling. Mechanical alloying, a repeated process of cold welding, fracturing and re-welding of powder particles in a high-energy ball mill, is a fundamental technique for the preparation of MMNCs.[11] Several techniques have been used to perform the compaction of composite powders: hot pressing, cold pressing, cold isostatic pressing (CIP), hot isostatic pressing (HIP), equal channel angular pressing (ECAP) followed by a sintering treatment.

Powder metallurgy produces well-dispersed metal matrix composites with uniform microstructure. It can be used to produce high melting point metals like Ti with less difficulty than liquid metallurgy. However, many treatment steps are necessary, which increases the price of fabrication. The presence of clusters of nanoparticles is also difficult to prevent. The products also show a limited range of shapes that is detrimental to vehicle industry. Therefore, the focus is put in this PhD work on liquid processing. Nonetheless, we describe below some powder metallurgy processes that are the main approaches used up to now to reach MMNCs.

Friction stir processing is one of the powder metallurgy approaches. The introduction of reinforcement objects into aluminum matrix can also be performed by multi-pass friction stir process. The principle is based on three major steps: firstly, fixing the matrix sample; secondly, drilling holes according to a predesigned pattern with pins into the matrix phase; thirdly, inserting nanoparticles into the holes.[97] Multiple passes are necessary for a uniform distribution of reinforcement particles. The friction stir process enables the introduction of more than one reinforcement. For example, Jalilvand et al.[97] applied a friction stir processing. 48 holes were drilled on the Al356 alloy surface. 14 were filled with 80 nm Al_2O_3 nanoparticles and the other 14 were filled with a powder of 155 nm SiO_2 nanoparticles to fabricate the final Al356/Al_2O_3+SiO_2 nanocomposites (Figure 1.6). Microstructural analysis indicated a uniform distribution of nanoparticles inside the passed zone. Compared to the A356 Al alloy and the friction stir-processed A356, enhanced mechanical and corrosion properties were observed for nanoparticles-reinforced A356 alloy. Several processing parameters can be tuned: rotational and velocity, number of passes and tilting angle.[97–100] The major disadvantage lies in the agglomeration of reinforcement particles caused by the inhomogeneous heating and the asymmetric flow of the material during processing.[101]

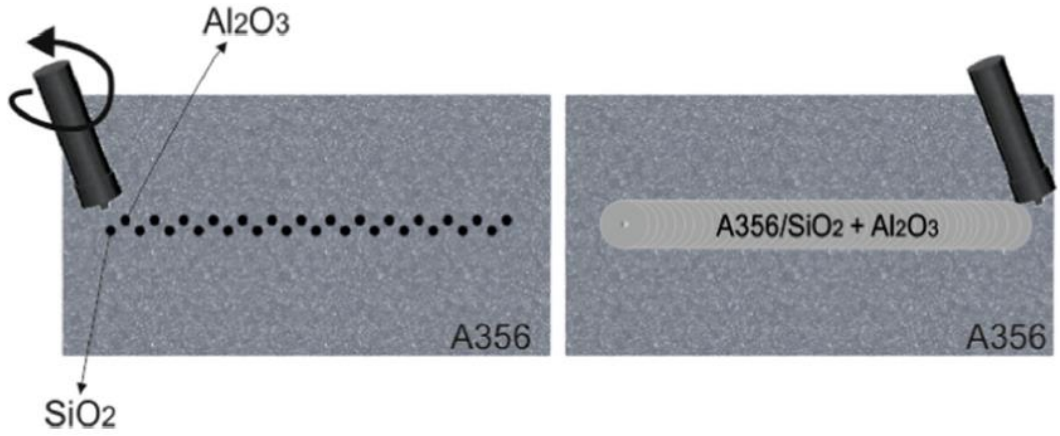

Figure 1.6. Friction stir process for fabricating SiO_2 and Al_2O_3 reinforced A356 nanocomposite.[97]

Spark plasma sintering is a method to consolidate powders to fabricate dense composites. The setup for this technique encompasses a uniaxial press, punch electrodes and a DC pulse current generator (Figure 1.7). The process general consists in four stages: a) creating a vacuum environment, b) exerting pressure, c) heating by DC pulse discharge that goes through the sample, and d) cooling and pressure release stage. This technique possesses several advantages, such as high heating rate, ability to reach enhanced densification with limited grain growth while promoting diffusion mechanisms. Saheb et al.[13] firstly prepared an homogeneous powder made of Al with 10 vol.% Al_2O_3 nanoparticles by ball milling for 24 hours and then processed the mixed powder in a spark plasma sintering setup with sintering temperature of 550 °C, holding time of 20 min, compaction pressure of 50 MPa and heating rate of 200 °C min^{-1}. The final Al/10Al_2O_3 nanocomposite exhibited hardness of 1309 MPa and yield strength of 311 MPa, significantly higher than those of bare aluminum. The Al/10Al_2O_3 MMNC also showed lower thermal expansion. The main mechanisms of SPS sintering is Joules heating of the sample, but further experiments should be performed to elucidate the mechanisms and figure out whether other phenomena such as plasma, sparks or electromigration exist or not.[102]

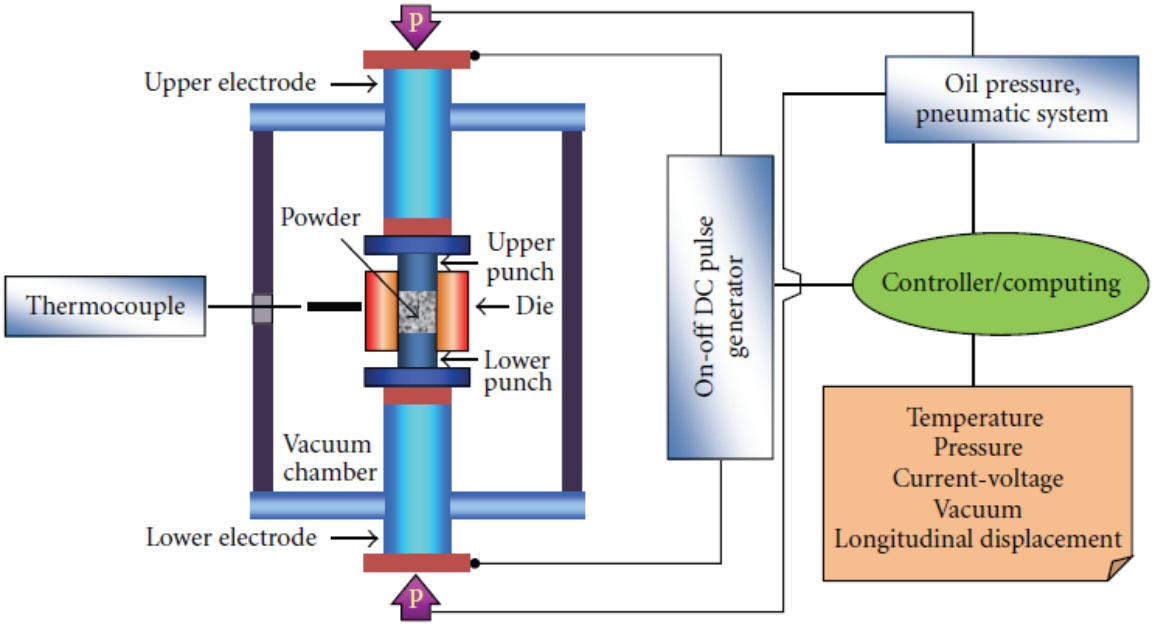

Figure 1.7 Scheme of a spark plasma sintering device.[102]

1.4.2 Liquid state process

In liquid metallurgy techniques, the reinforcement phase is added to the molten metal matrix in order to attain a desirable composition. There are some significant challenges to incorporate nanoparticles in molten metals. Firstly, the melt temperature is relatively high, some nanoparticles are not stable enough in these conditions; second, nanoparticles tend to float on the surface of the molten metal due to the poor wettability of the nanoparticles with the molten metal; third, nanoparticles agglomerate due to attractive Van der Waals force and to the lack of a repulsive force in molten metals; and fourth, nanoparticles are normally pushed to the grain boundary by solidification fronts during solidification.[103]

Three main liquid state processes are discussed here: stir casting, vortex casting, squeeze casting.

1.4.2.1 Ultrasound-assisted casting

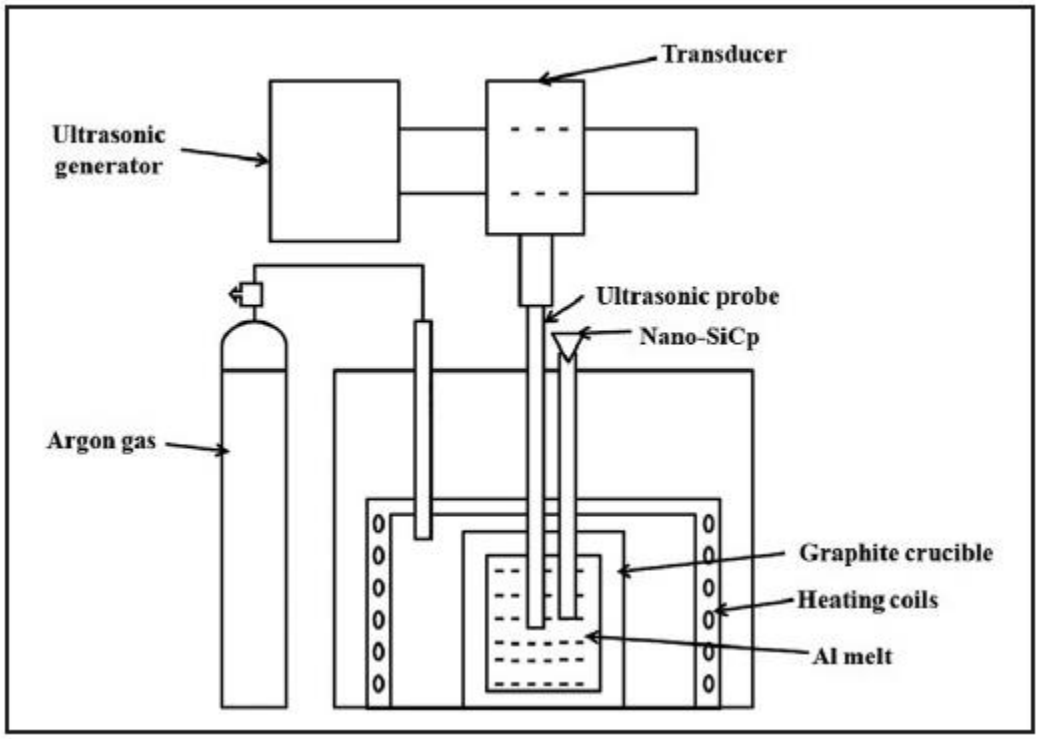

Figure 1.8. Schematic diagram of ultrasonic assisted casting.103

Stir casting has been widely applied as a commercial technique to fabricate MMCs. In conventional stir casting, the metal matrix is firstly de-moistured and heated above its melting temperature. Then the de-moistured reinforcement phase is added into the molten metal, followed by stirring with a stirrer to homogenize the reinforcement/metal matrix mixture. After cooling down in a mold, the final MMCs with desired shape could be obtained. But two main challenges prevail for this technique: one is related to the quantitative incorporation of the objects in the melt, the other one is the homogeneous distribution of the nano-reinforcements because of the high surface-to-volume ratio of the objects and of their poor wettability by the molten matrix, resulting in particle segregation and floating due to the density difference between the matrix and the nano-reinforcement objects.[104,105]

In order to solve these challenges, ultrasonication has been developed to disperse nanoparticles in molten metals (Figure 1.8). Eskin[106] has explained the application of ultrasound treatment to light alloy melts. In melts, the mechanism of cavitation is similar to other liquids. High intensity ultrasonic waves are introduced to generate transient cavitation and acoustic streaming, which are used to refine the microstructure, degas the melt and finally homogenize the distribution of reinforcement nano-objects.[107] During this process, the ultrasonic cavitation produces a strong implosive impact that could on one hand help to well disperse the nano-reinforcements and on the other hand enhance the wettability of the reinforcements by the molten metal.[108]

Table 1.3: Sound propagation rate in different metals and water[106]

The Speed of Sound *c* (Different Values According to References), Melting Point T_m, Density ρ, and Viscosity μ for Some Molten Metals and Water

Metal	T_m, °C	Temperature, °C	*c*, m/s	ρ, g/cm³	μ, mPa·s
Cs	28.6	28.5	967; 983	1.84	0.68
Ga	29.8	30	2740; 2873	6.08	2.04
In	156.2	156	2215; 2320	7.02	1.89
Sn	231.9	300	2270; 2464	6.99	1.85
Bi	271	300	1635; 1640	9.84	1.80
Pb	327.4	327	1790; 1821	10.66	2.65
Zn	419.6	420	2790; 2850	6.57	3.85
Mg	649	650	4065	1.584	1.25
Al	660	666	4561; 4729	2.375	1.3
Cu	1083	1084	3440	8.02	4.0
Water	0.0	20	1482	1.0	1.002

The varied material-dependent propagation sound speed (see Table 1.3), thermal conductivity and viscosity influence the acoustic impedance and the attenuation factor. The surface tension of metal melts is significantly higher than that of water (0.86 N m^{-1} for Al at 700 °C vs. 0.079 N m^{-1} for water at 20 °C), which decreases the dispersion efficiency. In order to achieve a good dispersion and distribution of nano-reinforcements, this other difficulty must be overcome when fabricating MMNCs.[106]

The production of composite materials with particles *via* ultrasound-assisted casting comprises several steps.

Step 1: Preparation of the particles with suitable surface treatment to decrease the surface tension and increase wetting of the reinforcement phase particles by the molten metal. A coating with metal like Cu or Ni, oxidation (like Al_2O_3), degassing and drying is useful to reach an homogeneous dispersion.[24]

Step 2: Preparation of the metal matrix. Additives for surface tension control are useful, especially for the liquid Al melt, which has a high surface tension. A lower surface tension metal like Bi, Pb, Sb, Li, Ca, Mg and Sn can be used to decrease the surface tension of Al.[109]

Step 3: Incorporation of the particles. The simplest technique consists in spraying the particles onto the surface of the melt. This technique works relatively well for magnesium MMCs[19] but has limitations in for MMCs due to the thick oxide film at the surface of the melt and to the high surface tension of the melt. In some cases, mechanical mixing using an impeller under protective atmosphere are combined with ultrasonic mixing.[110] Besides, the ultrasound processing parameters, the melt temperature, duration of processing, size, morphology and content of reinforcement particles can be adjusted to improve the dispersion.[24] One way to incorporate small particles while preventing flotation and macroscopic phase separation is to add the particles to the matrix in the semiliquid state (the temperature of the metal matrix is put between its liquidus and solidus temperature). For instance, SiC nanoparticles were added to a slurry of Mg-18% Zn alloy and dispersed with mechanical stirring. Then the composite material was heated to the liquid state and ultrasonicated to get a satisfying dispersion.[111]

Step 4: Casting and solidification. Ultrasonication in light alloy melts may affect nucleation and release of dissolved gas from the liquid phase. In semiliquid mixture, it influences the structure formation by fragmentation of solid crystals and their distribution.

In order to well understand the effect of ultrasonic stirring on the structure and mechanical properties of MMNCs, Jia et al.[112] applied ultrasonic treatment to incorporate 1 wt.% SiC or Al_2O_3 nanoparticles to aluminum alloy A356. The authors firstly melted the alloy in an induction furnace and then added nanoparticles into molten liquid under

ultrasonic stirring with power of 1.75 kW, frequency of 18 kHz. Subsequent solidification was performed to obtain aluminum metal matrix nanocomposite. The ultrasonic treatment could change the grain structure from dendritic to globular shape and also contribute to reasonable dispersion of nanoparticles into the final composite although some agglomeration still existed. Furthermore, the tensile strength of the nanoparticle-reinforced composites was higher with ultrasonic treatment.

The ultrasound assisted casting is highly dependent on the stability of nanoparticles and wettability of the inclusions by the matrix. Several combinations[1] are proven to be efficient, especially for the SiC/Mg_6Zn couple. Research of novel nanoparticles/metal matrix is still in need to achieve better mechanical properties or other atypic properties.

1.4.2.2 Vortex casting

Vortex casting has been proven useful to uniformly distribute reinforcement objects into a metal matrix. In a typical experiment, the milled reinforcement phase and matrix powders are continuously added to molten aluminum or aluminum alloy under stirring. Another stirring is performed to homogenize the mixtures after several minutes' crystallization. The final MMCs are obtained by shaping in a mold and an extrusion process. However, this method is difficult to be used for the incorporation of nanosized particles as it is difficult to reach high dispersion.

1.4.3 Squeeze casting

Squeeze casting is also a casting technique that involves two main steps: a) reinforcement objects addition into the molten metal matrix under mechanical stirring; b) solidification under high squeeze pressure. This technique can reduce porosity and shrinkage, improve casting yield and enhance properties of the final MMCs.[113] Lü et al.[60] firstly fabricated a millimeter-sized granule composed of 8 wt% SiC nanoparticles in aluminum by dry high-energy ball milling, then remelted and diluted this granule in molten A356 alloy to get final 1 wt% nanoparticles composites under ultrasonication. The molten mixture was poured into a die cavity that was disposed into an environment with 200 MPa squeeze pressure for 30 s until the end of

solidification (Figure 1.9). As a result, the nanoparticles were uniformly distributed into the nanocomposite and tensile strength of squeeze casted MMNCs was 2169 MPa, 25% higher than the non-reinforced alloy matrix.

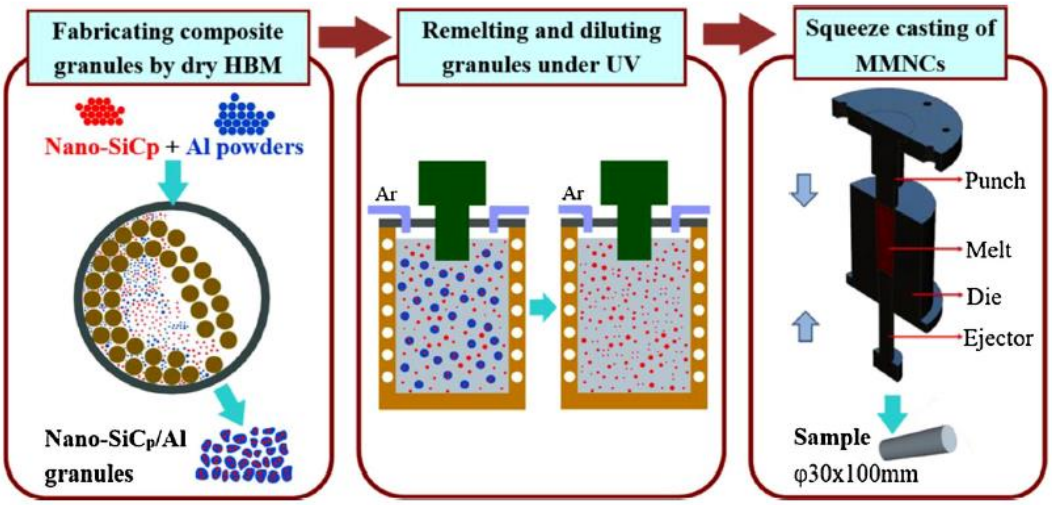

Figure 1.9. Flow chart of the fabrication of squeeze casted A356/SiC nanocomposites.[60]

1.4.4 Other techniques

1.4.4.1 Bottom-up fabrication

Luechinger et al.[114] have fabricated a bismuth and cobalt alloy by combining two immiscible metals at the nanoscale: bismuth and cobalt. Nanoparticles are mixed and pressed into pellets, then sintered to decrease the porosity. This bottom-up approach allows a perfect dispersion of the nanocrystalline phase, which could increase hardness and strength. However, porosity still exists and the fabrication needs pre-synthesized nanoparticles without passivating oxide layer, which is difficult to achieve for highly reductive metals like magnesium and aluminum.

1.4.4.2 Electrodeposition

The group of Akbulut presented a new hybrid nanocomposite thermal interface material (TIMs) relying on copper or silver, boron nitride nanosheets (BNNSs) and organic ligands. The composite was prepared by chemisorption-coupled electrodeposition approach.[115] BN nanosheets were exfoliated and functionalized by bifunctional ligands, which were supposed to link the metal and the BNNSs together through Lewis acid-base interactions. The co-electrodeposition/chemisorption process was then applied, which coupled the electrolytic reduction of metal ions and the chemisorption of functionalized BN nanosheets on the cathode. The thermal conductivity of the final composite was 236–258 W m^{-1} K^{-1} and 306–321 W m^{-1} K^{-1} for physically and chemically conjugated BNNS-silver-ligands materials, respectively, while their hardness varied from 400–495 MPa and from 240 to 360 MPa, respectively. The electrodeposition method is suitable to fabricate coating materials, but is hard to be applied to bulk materials.

1.5 Conclusion and motivation of this work

Faced with energy and environmental challenges and in line with the consumer demand, the Stellantis has been investing for several years in manufacturing vehicles that are more envir onmental friendly. To execute this strategy, the group wishes to invent and fabricate new materials that are light-weight and low cost with high ductility and also with good thermal conductivity. In this context, this PhD work aims to investigate MMNCs with improved mechanical properties and thermal properties. In particular, the fabrication processes must be designed to meet the needs of the current casting process of alloy.

Among the four types of fabrication techniques shown in this chapter, ultrasonic-assisted casting can meet these requirements. The use of ultrasonic treatment is a good way to improve the dispersion of nanoparticles during the casting process of aluminum alloy. This process also offers advantages such as low cost, easy molding process and adaptability to large-scale fabrication.

The literature review of current MMNCs opens many intriguing opportunities for the development of new materials. Regarding the mechanical properties of MMNCs, commercial inorganic nanoparticles have been proven useful to efficiently improve strength and functionality of the metal matrix. The reinforcement nanoparticles must be designed to satisfy the strengthening mechanisms and harsh casting conditions. Boride nanoparticles synthesized by molten salts are good candidates as they are small in size, light, hard and stable at high temperature. At the time when we started this project, there was only two papers available in the literature that used molten salt synthesized nanoparticles (particles size between 10 to 100 nm) as *ex situ* reinforcement.[63] Other related works were published recent years, especially from the group of Li[116] who worked on the incorporation of molten-salt synthesized TiB_2 and ZrB_2 nanoparticles in aluminum. A good dispersion of nanoparticles is essential for the mechanical properties and is a clear bottleneck in the facile fabrication of MMNCs with various reinforcement phases. It requires thorough control of compositional parameters (wettability of the matrix, nature of the compounds) and of processing parameters (heating process, ultrasound treatment power, heating/cooling rate). This part of the work will be explored in chapter 3.

Phase change materials have limited applications in vehicle's battery thermal control because of their low thermal conductivity and low resistance against vibration. Composites made by the incorporation of phase change materials in metal matrices are an interesting candidate for the automobile industry due to their high thermal conductivity, good mechanical properties and wide working temperature range. Conventional strategies for MMNCs design include powder metallurgy and bottom-up fabrication, which require high fabrication costs. Additionally, the working temperature is also limited: phase change only occurs at the melting temperature of pure metal, which is too high in most cases. To overcome these issues, we propose a liquid phase method: metallic nanoparticles (pure metal or alloy) will be encapsulated in an inorganic shell to prevent macroscopic phase separation in the melt. Subsequently, these nanoparticles will be incorporated in molten metal matrix by ultrasound-assisted process. This work will be presented in two parts: chapter 2 will deal with the synthesis of the building block core-shell nanoparticles, chapter 4 will deal with the fabrication of the nanocomposites and their thermal properties.

References

1. Ramanathan, A., Krishnan, P. K. & Muraliraja, R. A review on the production of metal matrix composites through stir casting – Furnace design, properties, challenges, and research opportunities. *J. Manuf. Process.* **42**, 213–245 (2019).
2. Mondal, S. Aluminum or Its Alloy Matrix Hybrid Nanocomposites. *Met. Mater. Int.* (2020) doi:10.1007/s12540-020-00750-5.
3. Petukhova, Y. V. *et al.* Polymer composites containing dispersed VO_2 of various polymorphs: Effects of polymer matrix on functional properties. *Mater. Chem. Phys.* **235**, (2019).
4. Antil, P., Singh, S. & Manna, A. Analysis on effect of electroless coated SiCp on mechanical properties of polymer matrix composites. *Part. Sci. Technol.* **37**, 787–794 (2019).
5. Balamurugan, P., Uthayakumar, M. & Niemczewska-Wójcik, M. Wear studies of copper-fly ash composite under dry sliding conditions. *Mater. Res. Express* **6**, (2019).
6. Song, Y. *et al.* Effect of carbon-fibre powder on friction and wear properties of copper-matrix composites. *Mater. Sci. Technol. (United Kingdom)* **36**, 92–99 (2020).
7. Li, M. *et al.* Microstructure evolution and properties of graphene nanoplatelets reinforced aluminum matrix composites. *Mater. Charact.* **140**, 172–178 (2018).
8. Kim, J. Tensile fracture behavior and characterization of ceramic matrix composites. *Materials (Basel).* **12**, (2019).
9. Ceschini, L.; Dahle, A.; Gupta, M.; Jarfors, A.E.W.; Jayalakshmi, S.; Morri, A.; Rotundo, F.; Toschi, S.; Singh, R. . *Aluminum and Magnesium Metal Matrix Nanocomposites*. (Springer, New York, NY, 2017).
10. Lloyd, D. J. Particle reinforced aluminium and magnesium matrix composites. *Int. Mater. Rev.* **39**, 1–23 (1994).
11. Pardeep, S., Gulshan, C. & Neeraj, S. Production of AMC by Stir Casting – An Overview. *Int. J. Contemp. Pract.* **2**, 23–46 (2013).
12. Ardakani, M. R. K., Amirkhanlou, S. & Khorsand, S. Cross accumulative roll bonding-A novel mechanical technique for significant improvement of stir-cast Al/Al2O3 nanocomposite properties. *Mater. Sci. Eng. A* **591**, 144–149 (2014).
13. Saheb, N. & Khan, M. S. Compressive strength and thermal properties of spark plasma sintered Al-Al2O3 nanocomposite. *Sci. Sinter.* **50**, 1–14 (2018).
14. Kandemir, S. Microstructure and mechanical properties of A357/SiC nanocomposites fabricated by ultrasonic cavitation-based dispersion of ball-milled nanoparticles. *J. Compos. Mater.* **51**, 395–404 (2017).
15. Law, E., Pang, S. D. & Quek, S. T. Discrete dislocation analysis of the mechanical response of silicon carbide reinforced aluminum nanocomposites. *Compos. Part B Eng.* **42**, 92–98 (2011).
16. Cao, C., Ling, H., Murali, N. & Li, X. In-situ molten salt reaction and incorporation of small (10 nm) TiC nanoparticles into Al. *Materialia* **7**, (2019).
17. Dhandapani, S., Rajmohan, T., Palanikumar, K. & Charan, M. Synthesis and

characterization of dual particle (MWCT+B4C) reinforced sintered hybrid aluminum matrix composites. *Part. Sci. Technol.* **34**, 255–262 (2016).

18. Sharma, R., P, S. J., Kakkar, K., Kamboj, K. & Sharma, P. A Review of the Aluminium Metal Matrix Composite and its Properties. *Int. Res. J. Eng. Technol.* **4**, 832–842 (2017).
19. Tjong, S. C. Novel nanoparticle-reinforced metal matrix composites with enhanced mechanical properties. *Adv. Eng. Mater.* **9**, 639–652 (2007).
20. Zhong, X. L., Wong, W. L. E. & Gupta, M. Enhancing strength and ductility of magnesium by integrating it with aluminum nanoparticles. *Acta Mater.* **55**, 6338–6344 (2007).
21. Zhang, F., Liu, S., Zhao, P., Liu, T. & Sun, J. Titanium/nanodiamond nanocomposites: Effect of nanodiamond on microstructure and mechanical properties of titanium. *Mater. Des.* **131**, 144–155 (2017).
22. Kim, K. T., Cha, S. Il, Gemming, T., Eckert, J. & Hong, S. H. The role of interfacial oxygen atoms in the enhanced mechanical properties of carbon-nanotube-reinforced metal matrix nanocomposites. *Small* **4**, 1936–1940 (2008).
23. Ibrahim, I. A., Mohamed, F. A. & Lavernia, E. J. Particulate reinforced metal matrix composites - a review. *J. Mater. Sci.* **26**, 1137–1156 (1991).
24. Casati, R. & Vedani, M. Metal Matrix Composites Reinforced by Nano-Particles—A Review. 65–83 (2014)
25. Veličković, S., Stojanović, B., Ivanović, L., Miladinović, S. & Milojević, S. Application of Nanocomposites in the Automotive Industry. *Mobil. Veh. Mech.* **45**, 51–64 (2019).
26. Abraham, A., Schoenitz, M. & Dreizin, E. L. Energy storage materials with oxide-encapsulated inclusions of low melting metal. *Acta Mater.* **107**, 254–260 (2016).
27. Thomas, K. E. & Newman, J. Thermal Modeling of Porous Insertion Electrodes. *J. Electrochem. Soc.* **150**, A176 (2003).
28. Nardone, V. C. & Prewo, K. M. On the strength of discontinuous silicon carbide reinforced aluminum composites. *Scr. Metall.* **20**, 43–48 (1986).
29. Ramakrishnan, N. An analytical study on strengthening of particulate reinforced metal matrix composites. *Acta Mater.* **44**, 69–77 (1996).
30. Miller, W. S. & Humphreys, F. J. Strengthening mechanisms in particulate metal matrix composites. *Scr. Metall. Mater.* **25**, 33–38 (1991).
31. Zhang, Z. & Chen, D. L. Consideration of Orowan strengthening effect in particulate-reinforced metal matrix nanocomposites: A model for predicting their yield strength. *Scr. Mater.* **54**, 1321–1326 (2006).
32. Zhang, Q. & Chen, D. L. A model for predicting the particle size dependence of the low cycle fatigue life in discontinuously reinforced MMCs. *Scr. Mater.* **51**, 863–867 (2004).
33. Cao, G., Choi, H., Oportus, J., Konishi, H. & Li, X. Study on tensile properties and microstructure of cast AZ91D/AlN nanocomposites. *Mater. Sci. Eng. A* **494**, 127–131 (2008).
34. Hull, D. & Bacon, D. J. *Introduction to dislocations*. (Butterworth Einemann: Oxford, UK, 2001).
35. Sanaty-Zadeh, A. Comparison between current models for the strength of particulate-

reinforced metal matrix nanocomposites with emphasis on consideration of Hall-Petch effect. *Mater. Sci. Eng. A* **531**, 112–118 (2012).

36. Zhang, S., Sun, D., Fu, Y. & Du, H. Recent advances of superhard nanocomposite coatings: A review. *Surf. Coatings Technol.* **167**, 113–119 (2003).
37. Malaki, M., Xu, W., Kasar, A. K., Menezes, P. L. & Dieringa, H. *Advanced Metal Matrix Nanocomposites*. (2013).
38. Li, Z. *et al.* Enhanced Mechanical Properties of Graphene (Reduced Graphene Oxide)/Aluminum Composites with a Bioinspired Nanolaminated Structure. *Nano Lett.* **15**, 8077–8083 (2015).
39. Bakshi, S. R., Lahiri, D. & Agarwal, A. Carbon nanotube reinforced metal matrix composites - a review. *Int. Mater. Rev.* **55**, 41–64 (2010).
40. Peng B, Locascio M, Zapol P, Shuyou L, Mielke SL, Schatz GC, et al. Measurements of near-ultimate strength for multiwalled carbon nanotubes and irradiation-induced crosslinking improvements. *Nat Nanotechnol* **3**, 626–31 (2008).
41. Choi H, Shin J, Min B, Park J, B. D. Reinforcing effects of carbon nanotubes in structural aluminum matrix nanocomposites. *J Mater Res* **24**, 2610–6 (2009).
42. Ma, Z. Y., Lia, Y. L., Zheng, Y. L. F., Bp, J. & Tjong, S. C. Nanometric Si3N 4 particulate-reinforced aluminum composite. **219**, 229–231 (1996).
43. Chaira, D. *et al.* Synthesis of Aluminium – Cementite Metal Matrix Composite by Mechanical Alloying Synthesis of Aluminium – Cementite Metal Matrix Composite. **6914**, (2016).
44. Lahiri, D. *et al.* Insight into reactions and interface between boron nitride nanotube and aluminum. *J. Mater. Res.* **27**, 2760–2770 (2012).
45. Firestein, K. L. *et al.* High-strength aluminum-based composites reinforced with BN, AlB2 and AlN particles fabricated via reactive spark plasma sintering of Al-BN powder mixtures. *Mater. Sci. Eng. A* **681**, 1–9 (2017).
46. Luo, X. & Li, C. Materials & Design Large sized cubic BN reinforced nanocomposite with improved abrasive wear resistance deposited by cold spray. *Mater. Des.* **83**, 249–256 (2015).
47. Kennedy, A. R., Weston, D. P. & Jones, M. I. Reaction in Al-TiC metal matrix composites. *Mater. Sci. Eng. A* **316**, 32–38 (2001).
48. Gopalakannan, S. & Senthilvelan, T. Application of response surface method on machining of Al-SiC nano-composites. *Meas. J. Int. Meas. Confed.* **46**, 2705–2715 (2013).
49. D. Sujan, Z. Oo, M. E. Rahman, M. A. Maleque, C. K. T. Physio-mechanical Properties of Aluminium Metal Matrix Composites Reinforced with Al2O3 and SiC. **6**, 678–681 (2012).
50. Miracle, D. B. Metal matrix composites - From science to technological significance. *Compos. Sci. Technol.* **65**, 2526–2540 (2005).
51. Li, A. B. *et al.* Enhanced combination of strength and ductility in ultrafine-grained aluminum composites reinforced with high content intragranular nanoparticles. *Mater. Sci. Eng. A* **745**, 10–19 (2019).
52. Nampoothiri, J., Harini, R. S., Nayak, S. K., Raj, B. & Ravi, K. R. Post in-situ reaction

ultrasonic treatment for generation Al–4.4Cu/TiB_2 nanocomposite: A route to enhance the strength of metal matrix nanocomposites Jayakrishnan. *J. Alloys Compd.* (2016)

53. Li, M. *et al.* Synthesis and mechanical behavior of nanostructured al 5083/ n-TiB_2 metal matrix composites. *Mater. Sci. Eng. A* (2016) doi:10.1016/j.msea.2016.01.031.
54. Yuan, L., Han, J., Liu, J. & Jiang, Z. Mechanical properties and tribological behavior of aluminum matrix composites reinforced with in situ AlB_2 particles. *Tribiology Int.* (2016)
55. Tian, K. *et al.* Effects of in situ generated ZrB_2 nano-particles on microstructure and tensile properties of 2024Al matrix composites. *J. Alloys Compd.* **594**, 1–6 (2014).
56. Ward-Close, C. M., Minor, R. & Doorbar, P. J. Intermetallic-matrix composites—a review. *Intermetallics* **4**, 217–229 (1996).
57. Hsu, C. J., Chang, C. Y., Kao, P. W., Ho, N. J. & Chang, C. P. Al-Al3Ti nanocomposites produced in situ by friction stir processing. *Acta Mater.* **54**, 5241–5249 (2006).
58. Xiu, Z. *et al.* Microstructure and Mechanical Properties of 45 vol.% SiCp/7075Al Composite. *J. Mater. Sci. Technol.* **31**, 930–934 (2015).
59. Gao, Q. *et al.* Effects of ultrasonic vibration treatment on particles distribution of TiB2 particles reinforced aluminum composites. *Mater. Sci. Eng. A* **680**, 437–443 (2017).
60. Lü, S., Xiao, P., Yuan, D., Hu, K. & Wu, S. Preparation of Al matrix nanocomposites by diluting the composite granules containing nano-SiCp under ultrasonic vibaration. *J. Mater. Sci. Technol.* **34**, 1609–1617 (2018).
61. Pourhosseini, S., Beygi, H. & Sajjadi, S. A. Effect of metal coating of reinforcements on the microstructure and mechanical properties of Al-Al2O3 nanocomposites. *Mater. Sci. Technol. (United Kingdom)* **34**, 145–152 (2018).
62. Taherzadeh Mousavian, R. *et al.* Incorporation of SiC Ceramic Nanoparticles into the Aluminum Matrix by a Novel Method: Production of a Metal Matrix Composite. *Met. Mater. Int.* (2020) doi:10.1007/s12540-019-00604-9.
63. Karbalaei Akbari, M., Baharvandi, H. R. & Shirvanimoghaddam, K. Tensile and fracture behavior of nano/micro TiB2 particle reinforced casting A356 aluminum alloy composites. *Mater. Des.* **66**, 150–161 (2015).
64. El-Kady, E.-S. Y., Mahmoud, T. S. & Sayed, M. A.-A. Elevated Temperatures Tensile Characteristics of Cast A356/Al₂O₃ Nanocomposites Fabricated Using a Combination of Rheocasting and Squeeze Casting Techniques. *Mater. Sci. Appl.* **02**, 390–398 (2011).
65. Vorozhtsov, S. *et al.* The Influence of ScF3 Nanoparticles on the Physical and Mechanical Properties of New Metal Matrix Composites Based on A356 Aluminum Alloy. *JOM* **68**, 3101–3106 (2016).
66. Reddy, M. P. *et al.* Enhancing thermal and mechanical response of aluminum using nanolength scale TiC ceramic reinforcement. *Ceram. Int.* **44**, 9247–9254 (2018).
67. Reddy, M. P. *et al.* Enhanced performance of nano-sized SiC reinforced Al metal matrix nanocomposites synthesized through microwave sintering and hot extrusion techniques. *Prog. Nat. Sci. Mater. Int.* **27**, 606–614 (2017).
68. Hwang, J. *et al.* Enhanced mechanical properties of graphene/copper nanocomposites using a molecular-level mixing process. *Adv. Mater.* **25**, 6724–6729 (2013).

69. Wang, F., Chu, K., Li, Y. biao & Wang, X. hu. Enhanced Interfacial Bonding and Mechanical Properties of Graphene/Cu Composites: A Matrix-Alloying Method. *Phys. Status Solidi Appl. Mater. Sci.* **215**, (2018).
70. Dorri Moghadam, A., Omrani, E., Menezes, P. L. & Rohatgi, P. K. Mechanical and tribological properties of self-lubricating metal matrix nanocomposites reinforced by carbon nanotubes (CNTs) and graphene - A review. *Compos. Part B Eng.* **77**, 402–420 (2015).
71. Tarascon, J.-M. & Armand, M. Issues and challenges facing rechargeable lithium batteries. in *Materials For Sustainable Energy* 171–179 (A Collection of Peer-Reviewed Research and Review Articles from Nature Publishing Group, 2011).
72. Oberthür, S. *The New Climate Policies of the European Union: Internal Legislation and Climate Diplomacy*.
73. Kim, J., Oh, J. & Lee, H. Review on battery thermal management system for electric vehicles. *Applied Thermal Engineering* vol. 149 192–212 (2019).
74. Bukhari, S. M. A. S., Maqsood, J., Baig, M. Q., Ashraf, S. & Khan, T. A. Comparison of Characteristics-Lead Acid, Nickel Based, Lead Crystal and Lithium Based Batteries. in *Proceedings UKSim 2015* 444–450 (Institute of Electrical and Electronics Engineers Inc., 2015).
75. Lowe, M., Tokuoka, S., Trigg, T. & Gereffi, G. *Lithium-ion Batteries for Electric Vehicles*. (Tech. Rep, 2010).
76. Offer, G., Patel, Y., Hales, A., Bravo Diaz, L. & Marzook, M. Cool metric for lithium-ion batteries could spur progress. *Nature* **582**, 485–487 (2020).
77. Yuan, X., Liu, H. & Zhang, J. *Lithium-ion batteries : advanced materials and technologies*. (CRC Press Taylor & Francis Group, 2012).
78. Adair, D., Ismailov, K. & Bakenov, Z. *Thermal Management of Lithium-ion Battery Packs*. (2014).
79. Arora, S. Selection of thermal management system for modular battery packs of electric vehicles: A review of existing and emerging technologies. *J. Power Sources* **400**, 621–640 (2018).
80. Khan, M. R., Swierczynski, M. J. & Kær, S. K. Towards an ultimate battery thermal management system: A review. *Batteries* vol. 3 (2017).
81. Pesaran, A. A. *An Approach for Designing Thermal Management Systems for Electric and Hybrid Vehicle Battery Packs Multi-scale mechanical-electrochemical-thermal coupled modeling framework for lithium-ion battery under mechanical abuse View project*. (1999).
82. Xu, X. M. & He, R. Research on the heat dissipation performance of battery pack based on forced air cooling. *J. Power Sources* **240**, 33–41 (2013).
83. Wu, M. S., Liu, K. H., Wang, Y. Y. & Wan, C. C. Heat dissipation design for lithium-ion batteries. *J. Power Sources* **109**, 160–166 (2002).
84. Nelson, P., Dees, D., Amine, K. & Henriksen, G. Modeling thermal management of lithium-ion PNGV batteries. *J. Power Sources* **110**, 349–356 (2002).
85. Xia, G., Cao, L. & Bi, G. A review on battery thermal management in electric vehicle application. *Journal of Power Sources* vol. 367 90–105 (2017).

86. Fisher, T. S., Torrance, K. E. & Torrance, K. E. *Optimal Shapes of Fully Embedded Channels for Conjugate Cooling*. *IEEE TRANSACTIONS ON ADVANCED PACKAGING* vol. 24 (2001).

87. Al Hallaj, S. & Selman, J. R. *A Novel Thermal Management System for Electric Vehicle Batteries Using Phase-Change Material*. *Journal of The Electrochemical Society* vol. 147 (2000).

88. Jaguemont, J., Omar, N., Van den Bossche, P. & Mierlo, J. Phase-change materials (PCM) for automotive applications: A review. *Applied Thermal Engineering* vol. 132 308–320 (2018).

89. Li, W. Q., Qu, Z. G., He, Y. L. & Tao, Y. B. Experimental study of a passive thermal management system for high-powered lithium ion batteries using porous metal foam saturated with phase change materials. *J. Power Sources* **255**, 9–15 (2014).

90. Ji, H. *et al.* Enhanced thermal conductivity of phase change materials with ultrathin-graphite foams for thermal energy storage. *Energy Environ. Sci.* **7**, 1185–1192 (2014).

91. Zhao, C. Y. & Wu, Z. G. Heat transfer enhancement of high temperature thermal energy storage using metal foams and expanded graphite. *Sol. Energy Mater. Sol. Cells* **95**, 636–643 (2011).

92. Liu, M., Ma, Y., Wu, H. & Wang, R. Y. Metal matrix-metal nanoparticle composites with tunable melting temperature and high thermal conductivity for phase-ch1. Liu M, Ma Y, Wu H, Wang RY. Metal matrix-metal nanoparticle composites with tunable melting temperature and high thermal conductivity . *ACS Nano* **9**, 1341–1351 (2015).

93. Goswami, R. & Chattopadhyay, K. Depression of melting point of multidomained bismuth in aluminum based metallic glass nanocomposites. *Appl. Phys. Lett.* **69**, 910–912 (1996).

94. Sharifi, E. M. & Karimzadeh, F. Wear behavior of aluminum matrix hybrid nanocomposites fabricated by powder metallurgy. *Wear* **271**, 1072–1079 (2011).

95. Arif, S., Alam, T., Ansari, A. H. & Shaikh, M. B. N. Morphological characterization, statistical modelling and tribological behaviour of aluminum hybrid nanocomposites reinforced with micro-nano-silicon carbide. *J. Asian Ceram. Soc.* **7**, 434–448 (2019).

96. Ahmadi, M. & Siadati, M. H. Synthesis, mechanical properties and wear behavior of hybrid Al/(TiO2 + CuO) nanocomposites. *J. Alloys Compd.* **769**, 713–724 (2018).

97. Jalilvand, M. M., Mazaheri, Y., Heidarpour, A. & Roknian, M. Development of A356/Al2O3 + SiO2 surface hybrid nanocomposite by friction stir processing. *Surf. Coatings Technol.* **360**, 121–132 (2019).

98. Nazari, M., Eskandari, H. & Khodabakhshi, F. Production and characterization of an advanced AA6061-Graphene-TiB2 hybrid surface nanocomposite by multi-pass friction stir processing. *Surf. Coatings Technol.* **377**, (2019).

99. Ostovan, F., Amanollah, S., Toozandehjani, M. & Shafiei, E. Fabrication of Al5083 surface hybrid nanocomposite reinforced by CNTs and Al 2 O 3 nanoparticles using friction stir processing . *J. Compos. Mater.* **54**, 1107–1117 (2020).

100. Heidarpour, A., Ahmadifard, S. & Kazemi, S. On the Al5083–Al2O3–TiO2 Hybrid Surface Nanocomposite Produced by Friction Stir Processing. *Prot. Met. Phys. Chem. Surfaces* **54**, 409–415 (2018).

101. Rathee, S., Maheshwari, S., Siddiquee, A. N. & Srivastava, M. A Review of Recent Progress in Solid State Fabrication of Composites and Functionally Graded Systems Via Friction Stir Processing. *Critical Reviews in Solid State and Materials Sciences* vol. 43 334–366 (2018).

102. Saheb, N. *et al.* Spark plasma sintering of metals and metal matrix nanocomposites: A review. *J. Nanomater.* **2012**, 1–13 (2012).

103. Wang, F. *et al.* A synchrotron X-radiography study of the fragmentation and refinement of primary intermetallic particles in an Al-35 Cu alloy induced by ultrasonic melt processing. *Acta Mater.* **141**, 142–153 (2017).

104. Su, H., Gao, W., Feng, Z. & Lu, Z. Processing, microstructure and tensile properties of nano-sized Al2O3 particle reinforced aluminum matrix composites. *Mater. Des.* **36**, 590–596 (2012).

105. Garg, P. *et al.* Advance research progresses in aluminium matrixcomposites: Manufacturing & applications. *Journal of Materials Research and Technology* (2019)

106. Eskin, G. I. E. D. G. *Ultrasonic treatment of light alloy melts, second ed.* (CRC Press, 2015).

107. Eskin, G. I. Cavitation mechanism of ultrasonic melt degassing. *Ultrason. - Sonochemistry* **2**, 20–28 (1995).

108. Cao, G. *et al.* Mg-6Zn/1.5%SiC nanocomposites fabricated by ultrasonic cavitation-based solidification processing. *J. Mater. Sci.* **43**, 5521–5526 (2008).

109. Mohanty, P., Mahapatra, R., Padhi, P., Ramana, C. H. V. V. & Mishra, D. K. Ultrasonic cavitation: An approach to synthesize uniformly dispersed metal matrix nanocomposites—A review. *Nano-Structures and Nano-Objects* **23**, 100475 (2020).

110. Khandelwal, A., Mani, K., Srivastava, N., Gupta, R. & Chaudhari, G. P. Mechanical behavior of AZ31/Al_2O_3 magnesium alloy nanocomposites prepared using ultrasound assisted stir casting. *Compos. Part B Eng.* **123**, 64–73 (2017).

111. Chen, L. Y., Peng, J. Y., Xu, J. Q., Choi, H. & Li, X. C. Achieving uniform distribution and dispersion of a high percentage of nanoparticles in metal matrix nanocomposites by solidification processing. *Scr. Mater.* **69**, 634–637 (2013).

112. Jia, S., Zhang, D., Xuan, Y. & Nastac, L. An experimental and modeling investigation of aluminum-based alloys and nanocomposites processed by ultrasonic cavitation processing. *Appl. Acoust.* **103**, 226–231 (2016).

113. Vijayaram, T. R., Sulaiman, S., Hamouda, A. M. S. & Ahmad, M. H. M. Fabrication of fiber reinforced metal matrix composites by squeeze casting technology. *J. Mater. Process. Technol.* **178**, 34–38 (2006).

114. Luechinger, N. A., Grass, R. N., Athanassiou, E. K. & Stark, W. J. Bottom-up fabrication of metal/metal nanocomposites from nanoparticles of immiscible metals. *Chem. Mater.* **22**, 155–160 (2010).

115. N. Nagabandi, C. Yegin, X. Feng, C. King, J.K. Oh, E.A. Scholar, S. N. & Akbulut, M. Chemically Linked Metal-Matrix Nanocomposites of Boron Nitride Nanosheets and Silver as Thermal Interface Materials. (2018)

116. Javadi, A., Pan, S. & Li, X. Fabrication of High Strength Al Nanocomposites with Populous TiB2 Nanoparticles. *Procedia Manuf.* **26**, 629–632 (2018).

Chapter 2

Synthesis of low melting point $Bi@SiO_2$ nanoparticles

2.1 Introduction

As described in chapter 1, metal matrix phase change nanocomposites are promising candidates for the thermal control of battery packs. To design such nanocomposites, we have selected Bi nanoparticles as proof-of-concept phase change material for their relatively low melting temperature. We focus on an aluminium matrix to target light weight composites. A Bi@Al_2O_3-Al nanocomposite has been successfully prepared previously by powder metallurgy.[1] In their process, a mixture of Al and Bi_2O_3 was ball milled then the pellet was heated and held above 300 °C to promote aluminothermic reduction to form an Al_2O_3 layer surrounding Bi particles within the Al matrix. The Main limitation of its use on battery pack is its high fabrication cost and low adaptability of the temperature range. Therefore, we investigate herein the ability of liquid metallurgy processes to design metal matrix phase change nanocomposites. To do so, we must first elaborate an approach that will avoid the coalescence of molten Bi droplets in the molten aluminium matrix. For this purpose, we seek to protect the Bi nanoparticles against coalescence by a silica shell to prevent nanoparticles coalescence. The objective of this chapter is to present the synthesis and characterization of these building blocks: bismuth nanoparticles encapsulated in a silica shell.

2.1.1 State of the art on the Bi synthesis

Bismuth nanoparticles are of interest for several applications such as catalysis[2] and biomedical contrast agents in computed tomography scan or X-Ray imaging.[3] In the latter case, they are especially good candidates due to their low toxicity and high biocompatibility.[4] The synthesis of bismuth nanoparticles has been performed by using the sol-gel process, solvothermal and hydrothermal methods as well as in microemulsions. Selected examples of syntheses are summarized in Table 2.1.

Back in 2000, Foos et al.[5] applied the inverse micelle method to produce Bi nanoparticles with a high yield and a diameter below 10 nm. The reduction of $BiOClO_4$ occurs in an aqueous solution inside of AOT (dioctyl sulfosuccinate, sodium salt) reverse micelles. A second micelle solution containing inverse micelles was composed of $NaBH_4$ as reducing agent dissolved in aqueous solution with the same [H_2O]/[AOT] ratio. Those two micellar systems

were then mixed under argon under stirring, yielding Bi particles. After washing, 50 mg of nanocrystalline Bi powder could be obtained. The particle size could be adjusted down to ca. 3 nm by changing the [H2O]/[AOT] ratio, but the samples showed high polydispersity.

One of the most prominent colloidal synthesis pathways to monodispersed Bi nanoparticle samples has been proposed by the group of Buhro's group[4,5]. Thermal decomposition of $Bi[N(SiMe_3)_2]_3$, prepared by the reaction between $Na[N(SiMe_3)_2]_3$ and Bi salts, was performed in the presence of a polymer surfactant poly(1-hexadecene-co-1-vinylpyrrolidinone) (PHD-co-PVP) and $NaN(SiMe_3)_2$ at 190 °C for 20 h. This synthesis resulted in a dark Bi colloidal dispersion. The particle size was restricted to around 21 and 24 nm.[4] In order to expand the range of diameter size, the authors modified the synthesis protocol by tuning concentration ratios between $Bi[N(SiMe_3)_2]_3$, PHD-co-PVP and $NaN(SiMe_3)_2$, leading to a tuning of the particle size over a wide range between 3-115 nm and with various morphologies such as Bi nanorods and nanoplates.[4] The authors also applied a hot injection method to reach a diameter ranging from 30 to 45 nm. But the synthesis procedure still shows some limitations: 1) the necessity of an additional step to prepare the $Bi[N(SiMe_3)_2]_3$ precursor, and 2) the unavailability of the stabilizing polymer PHD-co-PVP.[7] $BiCl_3$ can also be used as Bi precursor to obtain Bi nanoparticles with size range of 4-29 nm. These particles were proved as good catalysts for solution-liquid-solid growth of high-quality CdSe quantum wires.[5]

A simpler method has been developed by Scheele et al.,[8] by reducing $Bi(OAc)_3$ with oleylamine (OA) or trioctylphosphine (TOP) in the presence of thiols as stabilizing ligands at lower temperature (60 °C). The resulting Bi nanoparticles were obtained as monodisperse samples, especially for a diameter of 3.3 ± 0.5 nm. The size of the nanoparticles could be increased from 7-9 nm to 10-14 nm by tuning the ratio between thiol and oleylamine, and could be further increased by replacing oleylamine with TOP to get nanoparticles of 40 nm.

A stable suspension of Bi nanoparticles without toxic organic residue is one of the main challenges for the application of Bi nanoparticles in the field of biomedicine. Solvothermal synthesis and hydrothermal synthesis have been developed afterwards. Wang et al.,[9] applied solvothermal synthesis approach for Bi nanoparticles with different shapes. $NaBiO_3$ was

reduced by ethylene glycol in presence of the capping polymer of poly(vinyl pyrrolidone) (PVP) or a trace amount of Fe^{3+} at 200 °C. By tuning the ratio of PVP and Bi, also the amount of Fe^{3+}, the authors could achieve different shapes for the crystals such as spheres when the PVP/Bi ratio was 0, and nanocube when the ratio was 1.6. In presence of a trace amount of Fe^{3+}, the PVP/Bi ratio of 1.6 resulted in nanobelted crystals. Microwave heating could also assist this approach.

Theoretically, hydrothermal synthesis is difficult to be applied to fabricate oxidatively prone elements such as bismuth, which is prone to get oxidized in water. Brown et al.[10] developed an aqueous synthesis of Bi nanoparticles based on a pH-dependent solubility equilibrium. An aqueous solution of $Bi(NO_3)_3 \cdot 5H_2O$ was reduced by $NaBH_4$ at pH 7.4 in the presence of dextran as a stabilizer. The nanoparticles were stable between pH 7 and pH 12. Increasing the synthesis pH inside this range could slow down the reaction rate and lead to more dispersed Bi nanocrystals. However, the shape of nanoparticles was not well controlled.

The main reported methods for the synthesis of Bi nanoparticles have been presented above. In our work, we were particularly interested in obtaining bismuth nanoparticles smaller than 40 nm, since these particles exhibit a depression of the melting point around 250 °C, lower than the melting point of bulk Bi at 271 °C,[11] which could enable a decrease of the phase change temperature in the final metal matrix nanocomposites. The quantity of the product in each batch is also a critical factor because these nanoparticles will serve as precursors for the synthesis of nanocomposites, which requires more than 100 mg of nanoparticle for each lab-scale (see chapter 3) synthesis. Solvothermal and hydrothermal methods are attractive in this respect, but the samples are highly polydisperse and these syntheses often result in large particle size over 40 nm. We then selected the method developed by Scheele et al.[8] as it could satisfy the requirements described above.

Table 2.1 Representative examples of synthesis methods for Bi nanoparticles.[4]

Method	**Reductant**	**Stabilizing agent**	**shape**	**Particle size range**	**Reference**
Hydrothermal (80 ℃)	$N_2H_4 \cdot H_2O$	Na oleate	nanospheres	25-40 nm	Wang, Y, 2009.[12]
Hydrothermal (160 ℃)	$N_2H_4 \cdot H_2O$	PSS	nanospheres	60-90 nm	Yang, H., 2013.[13]
Hydrothermal (90 ℃)	$N_2H_4 \cdot H_2O$	PEG	nanobelts	10-50 nm	Ma, D., 2015.[14]
Hydrothermal (90 ℃)	NaH_2PO_2	Tartaric acid	nanobelts	10-100 nm	Ma, D., 2012.[15]
Hydrothermal (RT)	$NaBH_4$	starch	nanocrystals	10-20 nm	Xia, F., 2014.[2]
Chemical reduction in DMSO (RT)	$NaBH_4$	Sodium citrate	nanocrystals	3.3 nm	Velasco-Arias, D., 2012.[16]
Solvothermal (185 ℃)	EG	PVP, DMSO	nanospheres	200-400 nm	Li, J., 2009.[17]
Solvothermal (200-300 ℃)	TEG	PVP	nanospheres	60 nm	Kim, H.J., 2015. [18]
Solvothermal (198 ℃)	EG	PVP, urea	Microspheres nanospheres	400-800 nm	Chen, G., 2009. [19]
Microwave-assisted solvothermal	DEG; urea	Sodium citrate	nanospheres	100-600 nm	Wu, J., 2010. [20]
Microwave-assisted solvothermal	EG	EG	Microspheres nanospheres	45 nm-10 mm	Estrada-Flores, M., 2016. [21]
Thermal reduction (140-180 ℃)	-	-	nanospheres	170 nm	Carotenuto, G., 2009.[22]
Colloidal synthesis (315 ℃)	OA	OA	nanospheres	10-70 nm	Wang, Z., 2014. [23]
Colloidal synthesis (180 ℃)	$NaN(SiMe_3)_2$	PHD-co-PVP in DIPB	nanodots	3-115 nm	Wang, F., 2008.[6]
Photochemical synthesis in toluene	-	TMSC	amorphous nanoparticles	20 nm	Breitwieser, D., 2015. [24]
Photochemical synthesis in propylene carbonate	OA	OA, n-heptane	nanoparticles (unspecified shape)	10 nm	Brütsch, L., 2017. [25]
One-pot cementation method (150 ℃)	Fe (powder)	-	nanowires	60 nm width	Wang, Q., 2007. [26]
One-pot cementation method (RT)	Zn (powder)	-	nanotube arrays	3-5 nm width >1 mm length	Yang, B., 2003. [27]
Two-pot cementation method (RT)	Zn, Al (compact form)	MD, MA, SA	nanoparticles (unspecified shape)	10-120 nm	Reverberi, A., 2018.[4]

Colloidal synthesis (200 ℃)	Reduction of $Bi[N(SiMe_3)_2]_3$ by TOP	PHD-co-PVP or OA	nanoparticles	4-29 nm	Wang, F., 2010. [7]
Colloidal synthesis (178 ℃)	-	1-dodecanethiol	nanoparticles	~22 nm	Wei, B. 2016 [3]
Colloidal synthesis (40-60 ℃)	Reduction of $Bi(OAc)_3$ by oleylamine/TOP	1-dodecanethiol	nanoparticles	7-9 nm	Scheele, M. 2009 [8]
Colloidal synthesis (T = 80 ℃)	TOP	1-dodecanethiol	nanoparticles	6-27 nm	Son, J. S., 2011 [28]
Colloidal synthesis (100 ℃)	-	HAD	nanoparticles	10-24 nm	Yarema, M., 2010[29]
Colloidal synthesis (RT)	$NaBH_4$	1-decanethiol and EDTA	nanoparticles	2-10 nm	Marchak, D. 2013[30]
Colloidal synthesis (315 ℃)	OA	OA	nanoparticles	30-60 nm	Wang, Z., 2013[31]

Abbreviations:

PSS: Poly(sodium 4-styrene-sulfonate)

PEG: Polyethylene glycol

EG: Ethylene glycol

PVP: Polyvinylpyrrolidone

DMSO: Dimethyl sulfoxide

DEG: diethylene glycol (DEG)

PHD-co-PVP: poly(1-hexadecene-co-1-vinylpyrrolidinone

MD: Maltodextrin

MA: D-Mannitol

SA: Saponin

TOP: trioctylphosphine

OA: Oleylamine

HAD: hexadecylamine

EDTA: Ethylenediaminetetraacetic acid

2.1.2 State of the art on the growth of silica shell to encapsulate bismuth particles

The synthesis of silica coated metallic nanoparticles has been well studied for nanoparticles such as silver and gold.[32] Among the numerous applications of metal@silica core-shell nanoparticles, most biological applications of nanoparticles require a good control of the surface state of nanoparticles. The implementation of a silica shell helps to graft specific reactive functions such as antibodies or fluorophores.[32] Among all synthesis methods, we should cite two main processes: a) the Stöber process, a sol-gel process where the Si precursor (typically tetraethyl orthosilicate (TEOS)) is hydrolyzed and condensed in an alcohol-ammonia-water solution;[33] b) the use of a reverse microemulsion before condensation.[34]

The growth of a silica shell on Bi nanoparticles has been less studied in the literature. Lee et al.[35] developed Bi nanotube@SiO_2 core-shell structures by atomic layer deposition. Chen et al.[36] reported Bi@SiO_2 nanospheres of 100 nm via *in situ* reduction of Bi_2O_3@SiO_2 by $NaBH_4$. Luo et al.[37] synthesized around 80 nm Bi@SiO_2 with 5 to 20 aggregates encapsulated in the same silica shell. The synthesis method was not described in the article. Li et al.[38] synthesized 40 - 60 nm Bi nanoparticles in acidic solution at 80 °C, then the authors grew a 2 – 5 nm SiO_2 layer on the Bi nanoparticles by the Stöber process. Li et al.[39] succeeded to achieve monodisperse core-shell objects. Spherical Bi nanoparticles (70–75 nm) were synthesized by thermal reduction of $Bi(NO_3)_3$ in dodecanethiol at 178 °C. Then, a 40 nm-thick SiO_2 shell was grown by employing the reverse-microemulsion method: Bi nanoparticles were dispersed in cyclohexane and treated with ultrasonication, then polyoxyethylene, nonylphenylether and ammonia solution were added and stirred for 24 h.

In view of the facility of the synthesis and of the quantities of product achievable, the Stöber process has been applied in our work.

2.2 Synthesis and characterization of Bi nanoparticles

Firstly, we applied the protocol developed by Scheele et al.[8] for the synthesis of Bi nanoparticles. This protocol consists in reducing bismuth acetate in oleylamine in the presence of 1-dodecanethiol as ligand at 60 °C following a hot injection protocol, the experimental details are described herein:

Bismuth acetate (1 mmol) was mixed with 1- dodecanethiol (11.1 mL) and heated to 45 °C for 45 min under vacuum. The reaction flask was then purged with N_2 and heated to 60 °C. Oleylamine (22.2 mL) was quickly added under stirring and the reaction mixture was maintained at 60 °C for 24 h. Finally, Bi nanoparticles were washed twice by an ethanol/chloroform mixture (20/1 vol./vol.) and then re-dispersed in ethanol.

The powder X-ray diffraction (XRD) patterns confirmed that Bi nanoparticles were obtained (Figure 2.1a). TEM images (Figure 2.1b) showed that the sample consists in bismuth nanoparticles with diameter around 25 nm with a relatively narrow size distribution. Contrary to the literature in which nanoparticles of 12-14 nm were obtained by this process,[8] the nanoparticles we synthesized are larger and the sample is more polydisperse. We then evaluated the impact of a range of parameters to understand this difference. In brief, the particle size distribution did not exhibit significant dependence on the origin and purity of the reagents, on the synthesis temperature (60 ± 2 °C), neither on the reaction duration from 20 to 24 and 28 h. When the reaction time was decreased to 6 h, the nanoparticles (figure 2.1c) were more faceted. The only remaining synthesis parameter is the injection speed and/or the heating ramp after the injection. These parameters have not been described in the original article of Scheele et al.[8] Then, we have attempted to preheat oleylamine at 55 °C before injection. The resulting nanoparticles shown in figure 2.1d exhibit smaller particle size ranging from 4 to 24 nm with a wide range of morphologies compared with the sample prepared by hot injection of room-temperature oleylamine (figure 2.1b). Because the final nanoparticles are dedicated to the design of phase change materials relying on the melting temperature decrease of nano-sized bismuth, nanoparticles smaller than 30 nm are sufficient for this study as this size range corresponds to a noticeable decrease of the melting temperature.[40] Thus, we selected nanoparticles of 25 nm diameter (figure 2.1b) from room temperature oleylamine injection for the following steps.

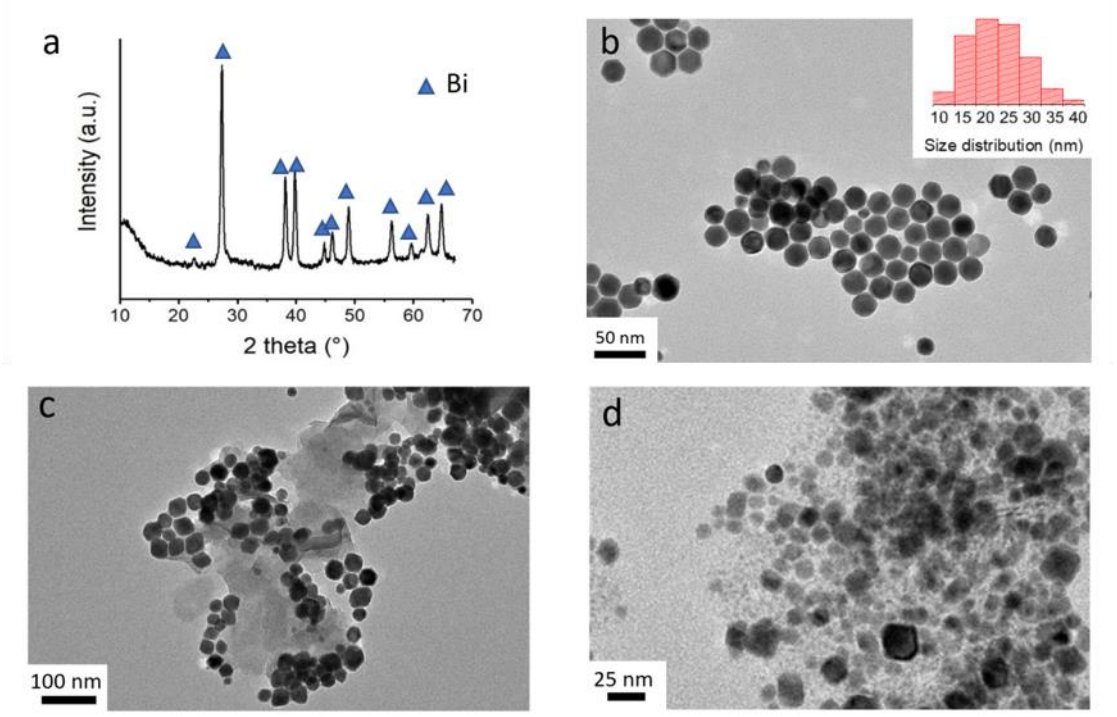

Figure 2.1. (a) Powder XRD pattern and (b-d) TEM images of Bi nanoparticles synthesized (b) at 60 °C for 24h from room-temperature oleylamine injection, (c) at 60 °C for 6h from room-temperature oleylamine injection, the low contrast part around nanoparticles are the organic residue. (d) at 60 °C for 24h from 55 °C oleylamine injection.

2.3 Synthesis and characterization of Bi@SiO_2 nanoparticles

In a second step, the bismuth nanoparticles washed with 2 centrifugation-dispersion cycles with ethanol and chloroform and were coated by a thick silica shell *via* the Stöber method.[33] The protocol is as follows:

Tetraethyl orthosilicate (TEOS) was dissolved in absolute ethanol at a concentration of 0.38 mol L^{-1}. 10 µL of this diluted TEOS solution and 100 µL of ammonia (30%) were subsequently added to 1 mL ethanolic bismuth suspension at [Bi] = 6.10^{-4} mol.L^{-1} under vigorous stirring. The mixture was heated to 40 °C for 3 hours. After cooling down, it was washed two times with ethanol.

The silica shell obtained is clearly observed on TEM images, with a lower contrast than that for the Bi core (Figure 2.2a). Its thickness was around 7 nm. TEM (Figure 2.2a) shows that the silica shell actually embeds several particles, forming aggregates with size up to 160 nm. Since the shape of aggregates is irregular, here we characterize its size with the area distribution (Figure 2.2c). The area varies from ~1500 nm^2 to ~20000 nm^2. The area of a single core nanoparticle is ~ 1500 nm^2, and the area of the largest object observed correspond to the 14 times the size of single object. Since nanoparticles partially overlap in TEM image, the largest objects possess *ca.* 20 nanoparticles inside the same silica shell.

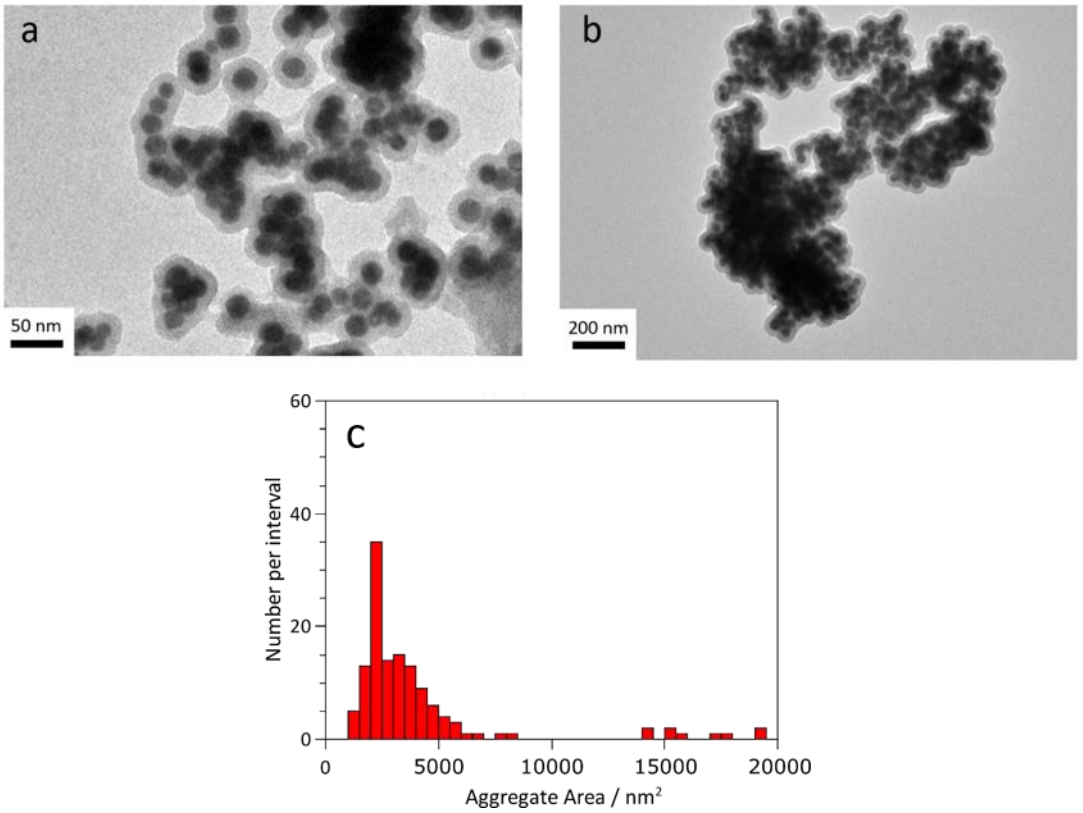

Figure 2.2. (a, b) TEM images of Bi@SiO_2 nanoparticles with silica shells prepared by the Stöber method. The Bi particles in (a) were washed 2 times before encapsulation. The corresponding size distribution is shown in (c). The Bi particles in (b) were washed 5 times before encapsulation.

This aggregation phenomenon is usual for the encapsulation by the Stöber process of poorly stable ethanolic suspensions of small nanoparticles.[34] The number of washing cycles of the initial particles strongly influences the size of the final objects as well. With subsequent centrifugation and washing steps, nanoparticles are more aggregated and yield Bi@silica aggregates larger than 1 micrometre after 5 washing steps (figure 2.2b). One explanation could be the removal of the stabilizing ligands on the surface of nanoparticles after washing. This phenomenon has been well described in the literature for gold nanoparticles,[41] in which repeated washing removed the ligands, yielding irreversible aggregation. As repeated washing results in aggregation of nanoparticles, no more than two washing steps were applied in order to preserve the suspension's stability in ethanol. We then attribute the formation of $Bi@SiO_2$ aggregates during silica growth to the low dispersibility of Bi nanoparticles in ethanol. By taking inspiration from the case of gold nanoparticles,[42,43,32] we applied ligand exchange to incorporate a functionalized thiol molecule that would ensure higher dispersibility of the particles in ethanol in the ligand monolayer. The ligand exchange protocol is described below:

After the synthesis of Bi nanoparticles and two washing cycles with ethanol and chloroform, the particles were redispersed in ethanol. A given quantity of ligand, varying from 0 to 5 ligand per Bi surface unit (nm^2), was solubilized in ethanol and was added into the reaction medium, followed by heating to 40 °C for 1 h in a closed vial in an oven.

At the end of their synthesis, the pristine Bi nanoparticles were covered by 1-dodecanethiol as ligand. Mercaptoundecanoic acid (MUA) and mercaptohexadecanoic acid (MHA) (Table 2.2) were assessed to perform ligand exchange. The thiol group is expected to graft on the surface of the nanoparticles and the acid group is expected to improve the dispersion ability in ethanol *via* hydrogen bonding. Different lengths of the spacer chain between MUA and MHA were used to tune the hydrophobicity of the ligand and of the nanoparticles.

Table 2.2 Molecular structure of MUA and MHA

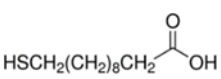

MUA

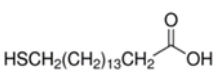

MHA

The quantity of ligands is also inspired from the case of gold nanoparticles. The total coverage ratio of thiol on gold surface was 5 thiol·nm^{-2}.[43] Series of experiences have been performed to study the influence of the exchanged ligand on the aggregation state of Bi cores within the silica shell/matrix. Figure 2.3 shows the similarity of the dispersibility of samples with or without MUA. Therefore, MUA does not appear as an efficient molecule to trigger ligand exchange and/or dispersion of the Bi particles.

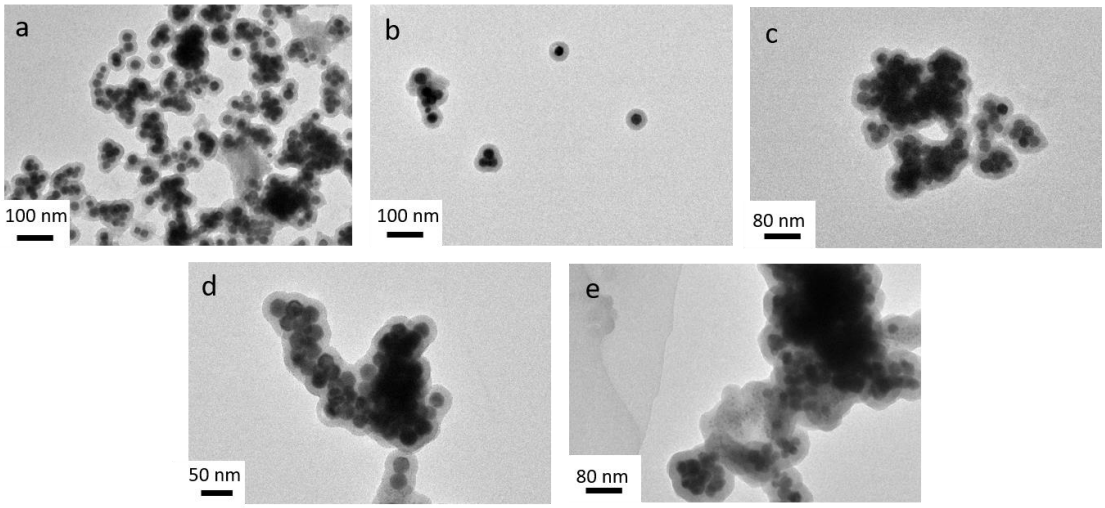

Figure 2.3. TEM images of Bi@SiO$_2$ nanoparticles from Bi nanoparticles washed during 2 cycles before further silica coating: (a) without ligand exchange; (b,c) ligand exchange with 1.5 MUA nm^{-2} (d) ligand exchange with 3 MUA nm^{-2} (e) ligand exchange with 5 MUA nm^{-2}.

In order to verify the efficiency of ligand exchange before growth of the silica shell, we observed the bismuth nanoparticles *via* TEM just after ligand exchange (in ethanol) and then after redispersion in an apolar solvent (hexane). Here, we should notice that the TEM grids were prepared by drop casting of nanoparticles' suspensions onto carbon-coated copper grids, which triggers further aggregation during evaporation. Nonetheless, we could not detect significant differences in terms of dispersibility between bare particles and ligand exchanged ones (figure 2.4a-c): aggregates of around 15 nanoparticles down to single nanoparticles were both observed in each sample. The effect of ligand exchange was not significant in ethanolic

suspensions. After redispersion in hexane, we observed aggregates around 200 nm, 400 nm and even larger than 800 nm for the samples without ligand exchange, exchanged with MUA and exchanged with MHA, respectively (figure 2.4d-f). The increased aggregation state with exchange of ligands indicated that ligand exchange actually occurred, but the increase of the hydrophobicity of the ligand didn't improve the dispersion in hexane, which could be ascribed as the influence of organic residuals as observed in TEM images. The aggregation state observed from the pristine ligand-exchanged Bi nanoparticles was maintained after growth of the silica shell (figure 2.5). The difficulty to reach a stable suspension of Bi nanoparticles is then the bottleneck that hinders isolation of single Bi@SiO_2 nanoparticles. This could arise from the reaction medium's composition (e.g. side product residuals from the Bi nanoparticles synthesis) and from intermolecular interactions between thiols, thiolates and Bi-thiolate complexes, which probably show differences in complexing abilities on different metal surface.

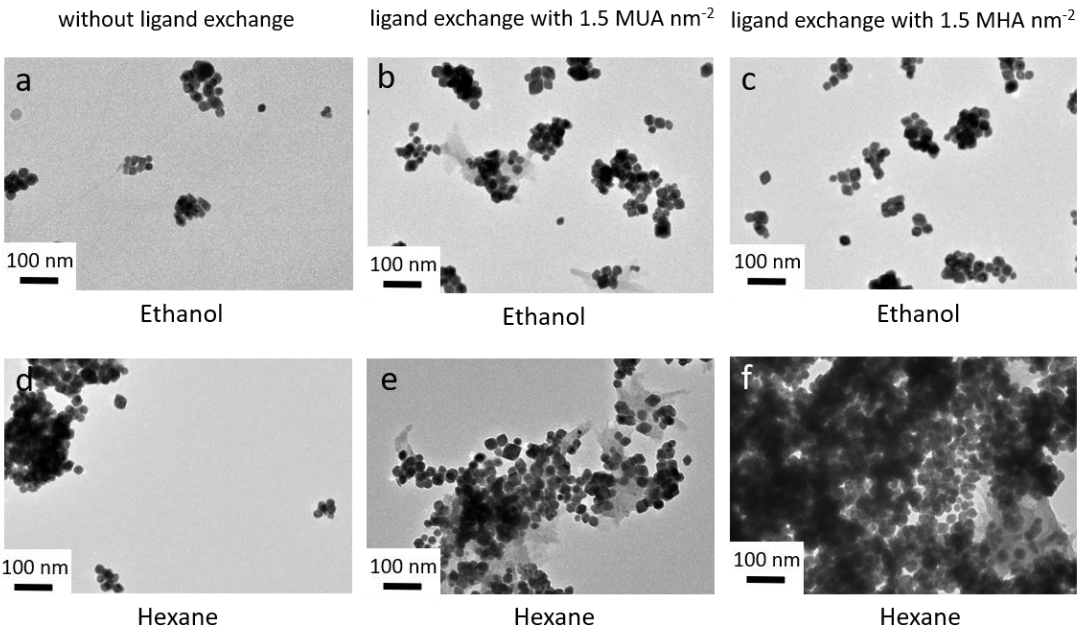

Figure 2.4 Influence of ligand exchange on the dispersibility of bismuth nanoparticles. (a-c) TEM images of Bi nanoparticles after two washing cycles and redispersion in ethanol: (a) without ligand exchange; after ligand exchange with (b) MUA and (c) MHA. (d-f) TEM images of corresponding nanoparticles shown in (a-c), centrifuged at 2000 rpm and redispersed in hexane: (d) without ligand exchange; after ligand exchange with (e) MUA and (f) MHA before redispersion. Low contrast layers around nanoparticles correspond to the organic residuals from the synthesis.

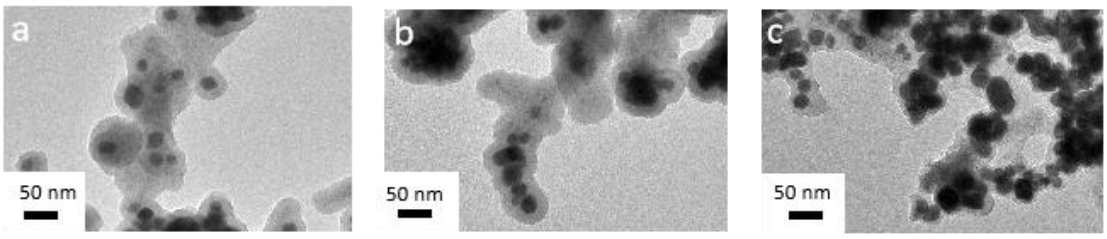

Figure 2.5 TEM images of Bi@SiO_2 samples for initial Bi nanoparticles after two washing cycles and coated with silica (a) without ligand exchange, with ligand exchange by (b) MUA and (c) MHA before silica encapsulation.

2.4 Conclusion

In this work, we succeeded in synthesizing core-shell Bi@SiO_2 nanoparticles with 25 nm Bi core and 7 nm silica shell. Clusters of several particles are embedded in the silica, forming aggregates of size up to 160 nm. By tuning the number of washing cycles of the pristine Bi nanoparticles, the most dispersed samples contain 1 to 15 nanoparticles that are encapsulated in the same silica shell. Single Bi nanoparticles encapsulated in silica shells have already been achieved for particles larger than 40 nm by the reverse-microemulsion method[39] and by acidic solution synthesis followed by Stöber method.[38] The encapsulation of Bi particles smaller than 30 nm by silica is still a challenge. Compared to previous results on silica-encapsulated Bi nanoparticles with particle size below 30 nm, which showed aggregates of 5 to 25 nanoparticles[37] and more than 20 nanoparticles[36] encapsulated in the same silica shell, our protocol shows enhanced dispersion of the Bi cores, although we could not obtain only single cores. Nevertheless, these nanoparticles meet the requirements described in the introduction: the particle size is small enough to trigger a decrease in the melting temperature and the synthesis was successfully scaled-up to 80 mg of product per batch. Another unexpected advantage is that the large size of the silica aggregates could facilitate the identification of the reaction between silica and aluminium. This part will be discussed in detail in chapter 4.

We have developed a two-step synthesis combining colloidal synthesis of Bi and Stöber method. The ligand exchange with two well-known ligands for gold system is not efficient in the case of bismuth particles. The dispersibility after the exchange of ligands is a complex phenomenon, which depends greatly on the experimental conditions. Several mechanisms are in competition between surface binding species like thiols, thiolates, Bi-thiolate complexes. External parameters such as solvent or atmosphere also influence the exchange, as well as the terminal functional group and the chain length. In the future, simulations could be carried out to further understand surface binding and then identify more suitable ligands. The reverse microemulsion method could also be a promising direction. The aqueous droplets in oil are uniform in size and usually smaller than 100 nm. They could act as nanoreactors and produce narrow-size distributions of core-shell nanoparticles.[34]

Chapter 3
Metal matrix nanocomposites with improved mechanical properties

3.1 Introduction

One of the key challenges in fabricating metal matrix nanocomposites by liquid metallurgy processes lies in the harsh conditions of the nanoparticles feeding and dispersion process at high temperature (over solidus or liquidus of aluminum alloys, generally over 550 °C). Indeed, the stability of nanoparticles at high temperature should always be kept in mind in order to obtain the final material. In the past decades, classic aluminum matrix nanocomposites have relied on commercial nanoparticles with a limited choice.[1] Recent progress in the *in situ* growth of oxide, boride and carbide nanoparticles has shown some promises in the increase of nanoparticle loading and in the interfacial bonding between nanoparticles and metal matrix.[2,3,4] In particular, the reaction of K_2TiF_6 amd KBF_4 in molten mixtures of aluminum and fluoride salts enabled the *in situ* formation of TiB_2 nanoparticles in different aluminum alloys.[4] However, two main concerns still exist: one is related to the difficulty to control the particle size and the other one lies in the presence of impurities in the final products.[4,5,6,7,8] The continuous development of nanoparticle synthesis approaches, especially the emergence of molten salts synthesis offers an alternative solution.[9] Several classes of nanoparticles including borides, nitrides, carbides and silicides have been synthesized using molten salt solvents.[10] The use of inorganic molten salts as high temperature solvents (300 to 900 °C) could lead to nanoparticles that are stable at the processing temperature of liquid metallurgy. As-synthesized nanoparticles possess well-controlled particle size and they could be easily dispersed in water or alcohols after several washing. All these developments taken together, nanoparticles prepared in molten salts appear as interesting potential precursors to create new metal matrix nanocomposites. Nevertheless, there are still several issues to overcome to reach this aim, such as the demixation of nanoparticles powders from the molten matrix during their incorporation and during solidification.

In this work, we aimed at designing boride-aluminum nanocomposites in the presence of 99.9% pure aluminum and of an aluminum alloy $AlSi_7MgCu$ (Table 3.1) by synthesizing *ex situ* the nanoparticles. Boride nanoparticles are hard and light-weight and are promising candidates to further reinforce light-weight alloys. In this chapter, we attempt to establish the suitability of boride nanoparticles synthesized in molten salts as a potential reinforcement for aluminum-based matrices. HfB_2 was selected as a target because it is a superhard material, with

a predicted Vickers hardness of 30.5 GPa,[11] It also contains hafnium, which is expected to facilitate the electronic microscopy observations and chemical detection in the final composites and will then be a useful probe to reach a proof-of-concept material. The dispersion behaviour of the nanoparticles in molten aluminum and its effect on the enhancement of mechanical properties are evaluated. The results are then compared with those obtained for reference SiC-based nanocomposites, a well studied aluminum-based matrix system.

Noticeably, at the time when we started this project, there were only two articles available in the literature that used molten salt synthesized nanoparticles (particles size between 10 to 100 nm) as external reinforcement.[12] But other related works have been published recently, especially from Li Group[13] who worked on the incorporation of molten-salt synthesized TiB_2 and ZrB_2 nanoparticles in aluminum. However, none of them have applied hafnium boride nanoparticles as reinforcement so far.

Alloying elements of alloys for cast parts									
Alloy	Composition tolerances (contents in %)								
	Si	Fe	Cu	Mn	Mg	Ni	Zn	Ti	Other elements
$AlSi_7MgCu$	6.5 7.5	<0.2	0.4 0.6	<0.1	0.28 0.4	< 0.05	< 0.1	0.08 0.20	< 0.1

Table 3.1 Aluminum alloy $AlSi_7Mg_{0.3}Cu_{0.5}$ composition[14]

3.2 Materials and methods

3.2.1 Preparation of nanoparticles

HfB_2 nanoparticles were prepared in molten salts as previously reported.[15] 0.5 mmol of hafnium (IV) chloride, 1 mmol of sodium borohydride and 2.5 g of eutectic mixture LiCl/KCl powders were ground together with a Retsch MM400 ball miller for 2 minutes at 20 Hz. The reaction medium was heated in a carbon crucible under argon flow at 900 °C for 4 h. After cooling down to room temperature, the nanoparticles were washed with 12 cycles of centrifugation-redispersion in water.

The synthesis of amorphous boron nanoparticles was similar to HfB_2 nanoparticles. 6 mmol of sodium borohydride was grounded with 5 g of eutectic LiI/KI. The medium was heated at 800 °C for 1 h. SiC nanoparticles with a diameter of 35 nm were purchased from Nanomaker, France.

3.2.2 Preparation of nanocomposites

HfB_2-Al and SiC-Al nanocomposites were prepared by ultrasound-assisted casting of a mixture composed of nanoparticles and aluminum. Two sets of experiments were designed. The first approach involved a direct introduction of nanoparticles into the molten metal. The metal matrix was heated at the desired temperature for 5 minutes. The desired amount of nanoparticles powder was packed in an aluminum foil and dipped into the molten metal at 720 °C. A steel spatula was used to stir the melt for 2 minutes. Then, a high-power ultrasonic probe made of niobium with tip diameter of 4 mm (QSonica sonicator Q500A-220, USA) was applied to disperse the nanoparticles for 5 minutes, with an interval of 5 s on / 5 s off at 30% of the nominal power. Finally, the sample was cast in an alumina crucible. For characterization, the middle part of the sample was cut and analyzed.

In the second approach, 2 g of aluminum powders (325 mesh, 99.99%) were added into an suspension containing the desired quantity of nanoparticles powders into 2 mL of ethanol, dispersed by sonication at 80 °C as setpoint for 1 hour. Then the mixture was dried in a vacuum oven at 40 °C for 1 h, followed by pressing into a pellet under 8 tons for 2 minutes. Subsequently, the pellet and 1 g of pure Al beads were heated by an induction oven at 720 °C under argon atmosphere in an alumina crucible. After dwelling for 1 min, ultrasounds were applied as described above to disperse nanoparticles for 5 minutes, with an interval of 5 s on / 5 s off. The final composites were obtained by cooling down the melt in the crucible. They were then cut by diamond wire saw for further analyses.

3.2.3 X-ray diffraction

X-ray diffraction was performed with a D8 Bruker diffractometer operating with CuKα radiation in Bragg-Brentano configuration. The ICSD reference card 30422 was used for the indexation of the HfB_2 structure.

3.2.4 Transmission electron microscopy

For transmission electron microscopy (TEM), the nanoparticles were dispersed in ethanol, then one drop was evaporated on carbon-coated copper grids. For the prepared composites, TEM thin foils were prepared by a rectangle of 3*3*0.5 mm cut in the middle of the sample. The polishing step was then performed by diamond disc to get a 200 μm thick sample and the thickness of the centre was further reduced to 50 μm by using a precision dimpling instrument (Model 515, South Bay Technology). Ion milling was performed for the final thinning. TEM images were recorded on a Tecnai spirit G2 microscope operating at 120kV. The STEM images and STEM-EDX mapping were recorded with a JEM 2100Plus UHR microscope, and were both performed at 200 kV. The size distribution of nanoparticles was determined by counting 150 to 200 nanoparticles from TEM images.

3.2.5 Scanning electron microscopy

The microstructure of the nanocomposites was characterized by scanning electron microscopy (SEM). The samples were mounted in polyfast resin (Struers), followed by a series of polishing steps through 1000, 2400, 4800 grit papers (Buehler) then with 3 μm and 1 μm diamond suspensions. For SEM observations, the samples were directly attached on a SEM holder using carbon tape. They were then observed under scanning electron microscopy (SEM, Hitachi S-3400N and Hitachi SU-70 microscope) equipped with an Oxford X-Max 50 mm2 EDS detector. Image analysis was performed with the Fiji software. The grain size distribution was measured by ImageJ from optical microscope images and SEM images.

3.2.7 Dynamic Light Scattering

The average hydrodynamic diameter of HfB_2 aggregates dispersed in water was determined by dynamic light scattering (DLS) in the Zetasizer Nano ZS90 (Malvern Panalytical).

3.2.7 Microhardness tests and nanoindentation tests

The Vickers hardness was measured with a load of 0.05 kg, dwell time 10 s using Wilson VH1102 microhardness testers.

The nanoindentation measurements were realized using a Nano Indenter XP® equipped with a Berkovich tip. The hardness was measured at the unloading process using Oliver and Pharr method. 400 measurements were achieved on a matrix of 21*19 with a distance of 10 µm at a depth of 1 µm to obtain a mapping of mechanical properties. The distance between two scratches was 10 µm. A matrix of 6*5 with a depth of 3 µm was performed to obtain an average measurement of mechanical properties.

3.3 Results and discussion

3.3.1 Preparation and characterizations of nanoparticles

HfB_2 nanoparticles were prepared by molten salts synthesis.[15] Different contrasts observed by TEM (figure 3.1a) confirm the core-shell structure of the nanoparticles. TEM shows a diameter of the contrasted core of 4 to 14 nm. This core shows high contrast, which is ascribed to a crystalline character and to a higher electron density, due to the Hf content. The powder XRD pattern (figure 3.1b) is fully indexed along the hexagonal HfB_2 structure. The crystallite size of HfB_2 calculated according to the Scherrer formula is 8 nm, in agreement with TEM, thus indicating that the core is single crystalline and made of HfB_2. A less contrasted layer of ca. 3 nm shown covers the surface of HfB_2 nanoparticles, corresponding to a layer of amorphous boron as described in a previous study.[15] The diameter measured by DLS on an aqueous dispersion is about 400 nm, which is much larger than the TEM data, indicating the formation of aggregates. These objects are clearly observed by TEM, which indicates that the amorphous shell embeds several particles. According to X-ray photoelectron spectroscopy (XPS) published in a previous work,[15] the boron surface is partially oxidized for the nanoparticles washed with water.

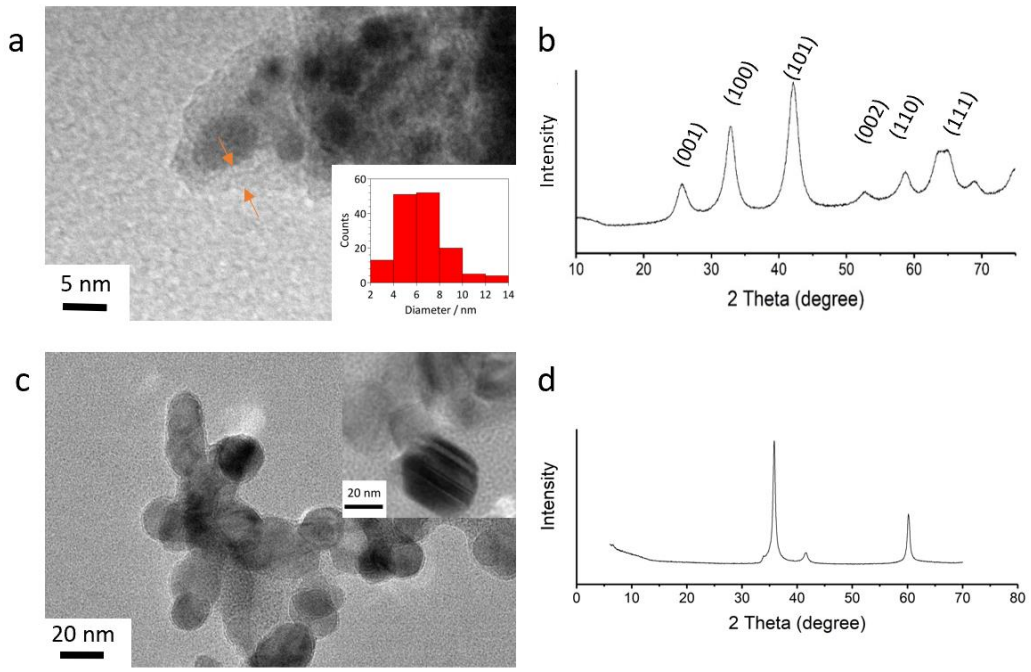

Figure 3.1 TEM images (left) and powder XRD patterns (right) of (a,b) HfB_2 nanoparticles coated with an amorphous boron-rich layer, as shown between two arrows; (c,d) of commercial SiC nanoparticles, respectively.

Commercial SiC nanoparticles were purchased from Nanomakers. The particle size ranges from 20 to 50 nm, with an average diameter of 35 nm. Defects can be observed inside the commercial nanoparticles (figure 3.1-c). The powder XRD pattern (figure 3.1d) confirms that SiC is the only crystalline phase.

3.3.2 Preparation of metal matrix nanocomposites

To overcome the difficulties of directly loading the nanoparticles powders in the melt (see Appendix S3.1), which are mainly ascribed to the poor wettability and high volume of nanoparticles in powder form, we used a two-step process to introduce nanoparticles in the melt:

a) dispersing the nanoparticles in ethanol in the presence of 325 mesh aluminum micro-powder, then pressing the slurry into a pellet;

b) diluting the pellet in molten aluminum under ultrasonication.

Pressing of the pellet at room temperature without heating prevented the coalescence of the nanoparticles and excluded the potential reactivity between Al micrograins and the boron shell of the nanoparticles before the dispersion process.[12]

The experimental setup is shown in figure 3.2a. Ultrasonic waves generate cavitation and acoustic streaming, which is most likely to refine the microstructure, break aggregates and homogenize the distribution of nanoparticles.[16] However, most commercial ultrasound microprobes for < 5mL volume are made by Ti alloy. This material is not applicable in our case because of the erosion of the Ti rod in molten aluminum[17] and the reactivity with the nanoparticles, especially their boron shell. A niobium tip of 4 mm diameter has been specially designed by the supplier company to limit the contamination of the samples (figure 3.2b). We further designed the shape of the crucible, as shown in figure 3.2c, to increase the dipping depth of the ultrasonic tip. The tip was dipped in 2 mL of molten aluminum at a depth of 3 mm, corresponding to 60% of the depth of liquid Al. This set-up is suitable for preliminary studies without the need to scale up the synthesis of nanoparticles.

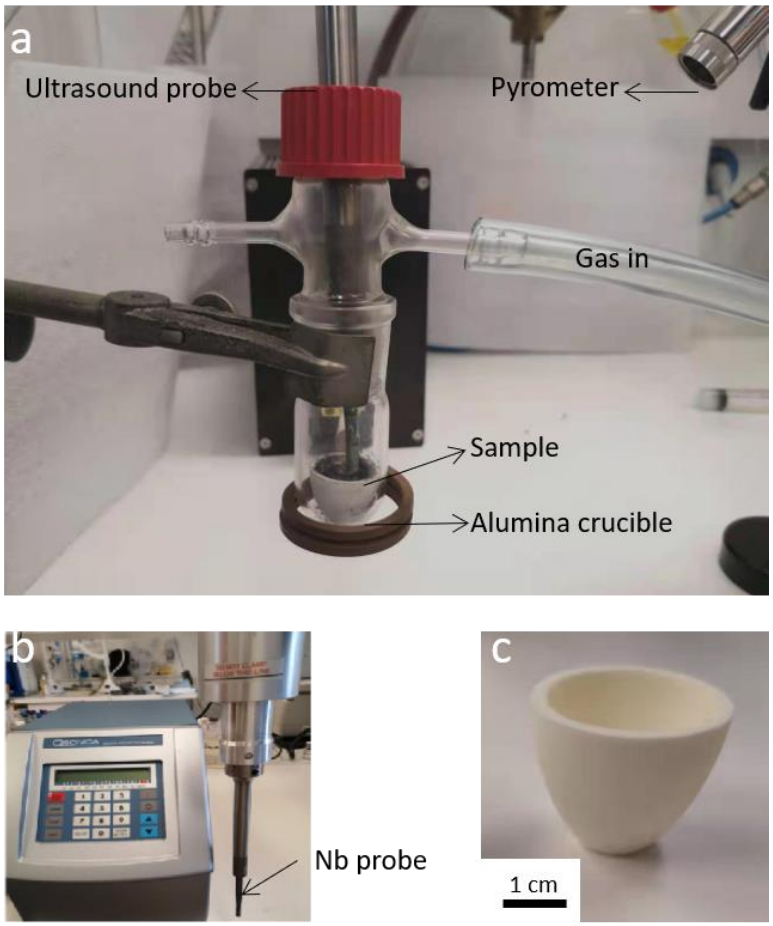

Figure 3.2 Experimental setup for incorporating nanoparticles into a molten metal by coupling induction heating and high temperature ultrasonication. a) reaction system, b) sonicator with Nb probe, c) alumina crucible.

Furthermore, the ultrasound treatment power and intervals have also been tuned. Previous works have shown that the mechanical properties of composites prepared by discontinuous ultrasonic treatments were better enhanced than with the continuous ultrasonic treatments due to enhanced dispersion.[16] In our study, an interval of 5s on/ 5s off was applied for all experiments. Considering the liquid splash at high power and pore formation at intermediate power, we chose to work at an intermediate ultrasound power at 30% of the maximum power followed by 30 s degassing with a low power of 10%. These conditions were then set as a model for the following experiments.

More details for the improvement of the process can be found in appendix S3.1.

3.3.3 Microscopy analysis of HfB_2 and SiC nanocomposites

HfB_2-Al nanocomposites

Several experiments were performed by dispersing 0.8 vol.% HfB_2-Al nanoparticles into aluminum using conditions defined in 3.3.2. The experimental parameters are presented in table 3.2 (P83). Broad peaks from XRD patterns (Appendix 3.5) confirmed that the phase was maintained. Low intensity peaks at 28° and 41° might be indexed along the AlB_{12} phase, which may arise from the reaction between molten aluminum and the boron-rich shell of the nanoparticles.

These samples were further analyzed by electron microscopy coupled to EDS. Figures 3.3a,b show SEM images of HfB_2-Al nanocomposites prepared in a resistive furnace, with ultrasound treatment through a Nb tip for 5 minutes, followed by cooling down in liquid nitrogen. Aggregation of HfB_2 particles was observed along the Al grain boundaries of the final metal matrix rather than a uniform distribution within the matrix. EDS analysis measurements (Figure 3.3c and d) yield a heterogeneous composition between the boundaries and the grains, which indicated that HfB_2 nanoparticles were segregated towards grain boundaries.

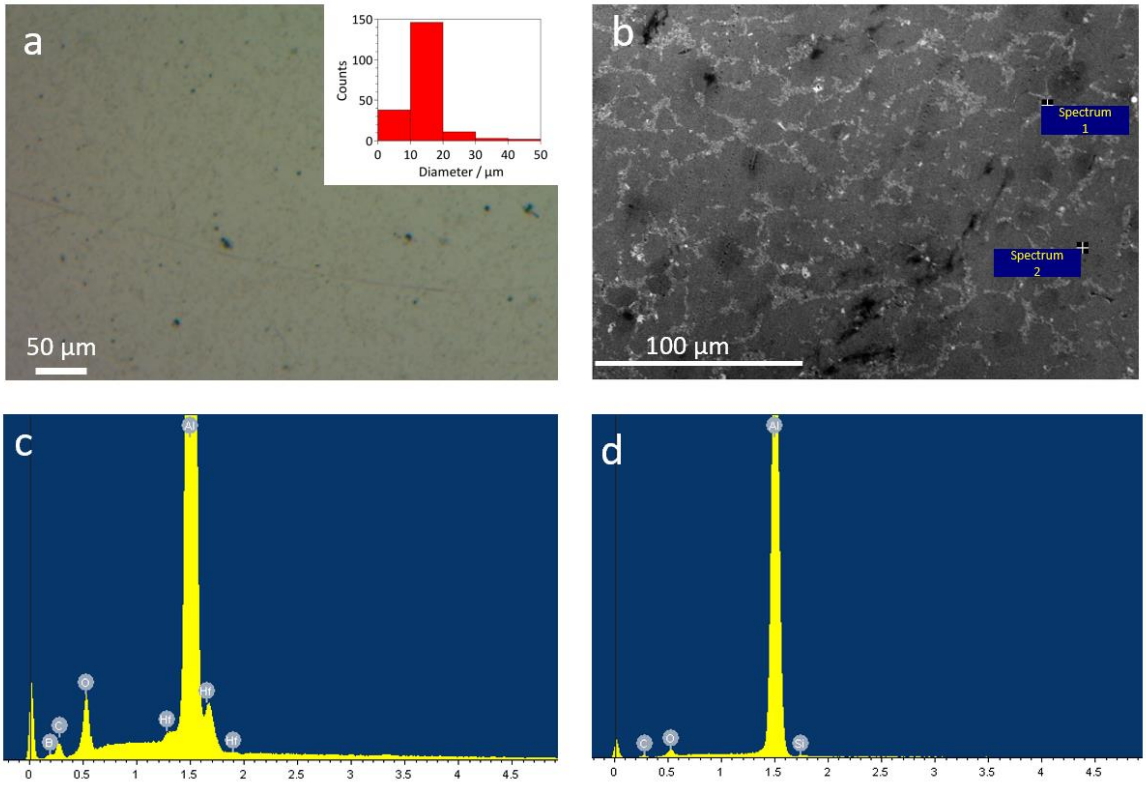

Figure 3.3. Characterization of a 0.8 vol% HfB_2-Al nanocomposite prepared with ultrasound treatment by Nb tip for 5 minutes and cooled down in the liquid nitrogen. (a)Optical image and size distribution of Al grains. SEM image (b) and EDS analysis of a grain boundary (c, corresponding to the point of spectrum 1 in b) and inside the Al grain (d, corresponding to the point of spectrum 2 in b). Dark and grey contrasts correspond to aluminum and to aggregates of nanoparticles, respectively.

TEM images (figure 3.4) also showed that nanoparticles formed into sub-micron aggregates at the Al grain boundaries and no separated nanoparticles could be found in Al grain. Compared to the initial nanoparticle precursors, HfB_2 nanoparticles could maintain their size after the harsh melting process at high temperature (figure 3.4a) although their morphology slightly changed from sphere-like particles to faceted particles (figure 3.4b). The HfB_2 crystal structure was confirmed according to the lattice spacing observed by HRTEM, also indicating the thermal stability of HfB_2 nanoparticles.

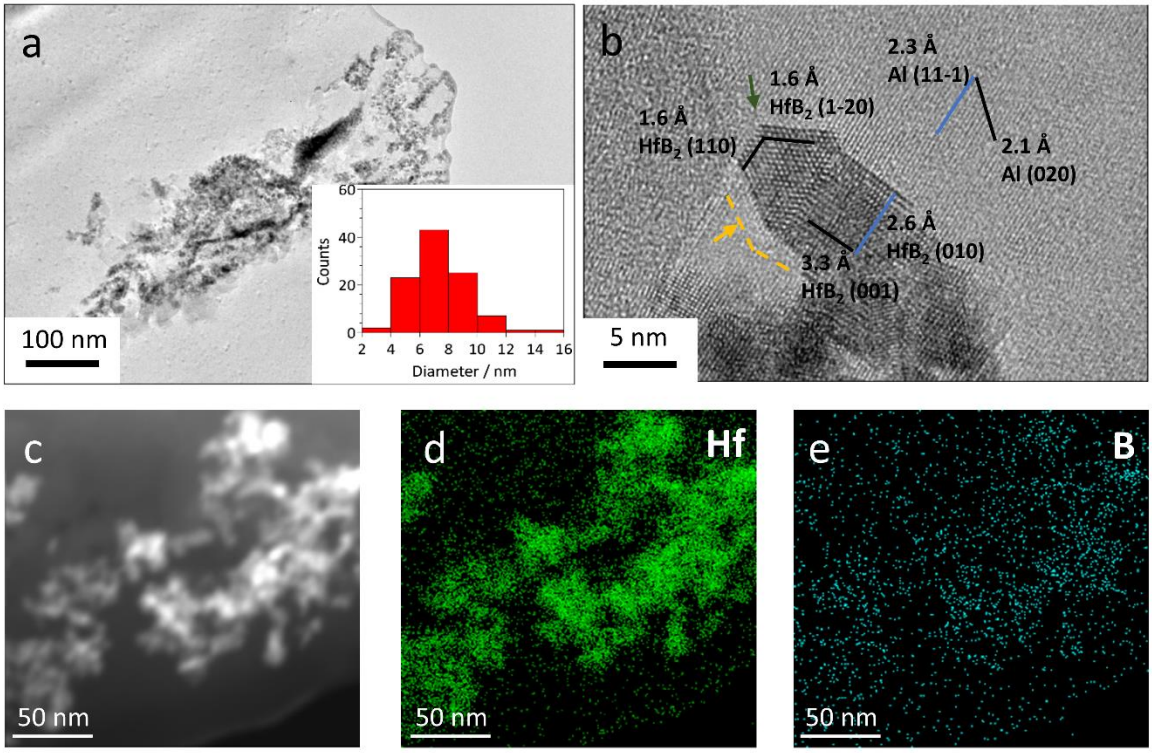

Figure 3.4. (a,b) TEM images of a 0.8 vol% HfB_2-Al nanocomposite prepared by 5 min sonication in a resistive furnace followed by liquid N_2 quenching. Dark and light parts correspond to HfB_2 nanoparticles and to the aluminum matrix, respectively. (c-e) STEM-EDS mapping showing the overlap of Hf (d) and (e) B elements in the aggregates

The state of the interface between aluminum and nanoparticles could reveal the reactions and events during nanoparticle composite synthesis. We have focused on interfaces between crystalline HfB_2 nanoparticles and the Al matrix as was observed in figure 3.4b. Three relationships have been observed at interface between HfB_2 nanoparticles and Al:

a) $(010)_{HfB_2}//(111)_{Al}$ as shown by blue lines. In fact, these plane presents the best match (d=0.26 nm) with $(111)_{Al}$, which should promote the epitaxial crystallization of the Al grain.

b) A distortion of lattice fringes extending up to 1 nm from the interfaces (green arrow). The mismatch between other HfB_2 facets and Al lattice planes, except for the plane couple described above, could disturb crystalline order of Al near the interface, and thus cause Al lattice distortions near the interface.

The combination of possible epitaxial relationship (a) and lattice distortion (b) implies that the HfB_2-Al interface could be semi-coherent, which is expected to favour the mechanical properties.[18] The modification of the shape of the nanoparticles implies also that the particles undergo facet reconstruction, favouriting (010) facets epitaxially oriented versus $(100)_{Al}$ planes.

c) Amorphous-like defects. (yellow arrow, within yellow dashes) This could be attributed to the reactivity of the matrix with the *ca.* 2 nm thick amorphous boron-rich layer exhibited by the initial nanoparticles. The size range of this area at the interface between HfB_2 and Al in figure 3.4b is consistent with the thickness of the pristine layer. According to the Al-B phase diagram (Appendix 3.6),[19] AlB_2 and AlB_{12} could form above 500°C. Although the kinetics of the reaction between nanoscaled boron (in the form of the nanoparticles' shell) and molten Al are unknown, a previous study showed that AlB_2 AlB_{10} and AlN form at the interface between BN nanotubes and aluminum after 10 minutes at 650°C,[20] which is corresponding to conditions similar to those used in our experiment. The Gibbs free energy for the formation of aluminum boride from Al and boron is similar to the one for the reaction described in the literature,[20] so the presence of crystalline aluminum boride is highly possible in our sample. No fringe is observed, probably because this phase is not well oriented.

The identification of the nature of the boron-rich shell is necessary to differentiate boron from the Al matrix. It is a strong challenge as boron cannot show contrast differences in the presence of Al. We performed high resolution TEM in a region where the Al matrix was not well oriented: Al fringes cannot be observed (Appendix 3.7). A crystalline layer around 2 nm shows lower contrast compared with the 4 nm dark core. The HRTEM micrograph cannot be indexed satisfactorily along structures such as Al, Al_2O_3, Hf, HfO_2, HfB_2, HfB, AlB_2, AlB_{10}, but could be attributed to AlB_{12}, in agreement with XRD (Appendix 3.5).

SiC-Al nanocomposites

A 0.8 vol% SiC-Al nanocomposite was obtained *via* the approach detailed in the previous section. It showed results similar to HfB_2-Al nanocomposites: nanoparticles mostly segregated at the grain boundaries according to SEM images (figure 3.5a-e). Figure 3.5f shows a TEM image of a SiC nanoparticle in a 200 nm Al grain. This indicates that part of the SiC particles

are located inside the grains, witch is according to the previous literature,[16] and contrary to our TEM observations for HfB_2-Al composites.

In fact, one of the main challenges for the preparation of metal matrix nanocomposites is that nanoparticles tend to segregate towards the grain boundaries at the solidification fronts upon cooling down. This phenomenon can be explained by several reasons: a) in both SiC and HfB_2 samples, nanoparticles form aggregates in the solid state due to attractive Van der Waals forces, while the applied ultrasound cavitation and acoustic streaming in molten metal is not sufficient to disperse aggregates into single particles. HfB_2 are also initially located into a boron-rich layer that embeds irreversibly several particles together. b) during solidification, attractive Van der Waals forces and interfacial forces overcome the Brownian motion and viscous drag force,[21] leading to particle aggregates, c) SiC and Al have a rather large equilibrium lattice mismatch,[22] which is detrimental to interfacial stability and energetically disfavors an homogeneous dispersion, d) The presence of a passivation oxide layer onto Al, as shown by EDS mapping, may also impact the wetting behaviour of Al on SiC.

Previous works have been performed to improve the dispersion of nanoparticles within SiC-Al alloy nanocomposites.[23,24,25] A better dispersion has been achieved by Lu et al., where diluted granules are prepared by powder metallurgy and dispersed into a molten Al alloy by ultrasonication. Although micro-sized clusters were observed, nanoparticles were not totally pushed to the grain boundaries.[21] An even better dispersed nanocomposite could be achieved by changing the composition of the matrix to tune the wettability and the rheology, such as for the dispersion of SiC in Mg-Zn alloys.[26]

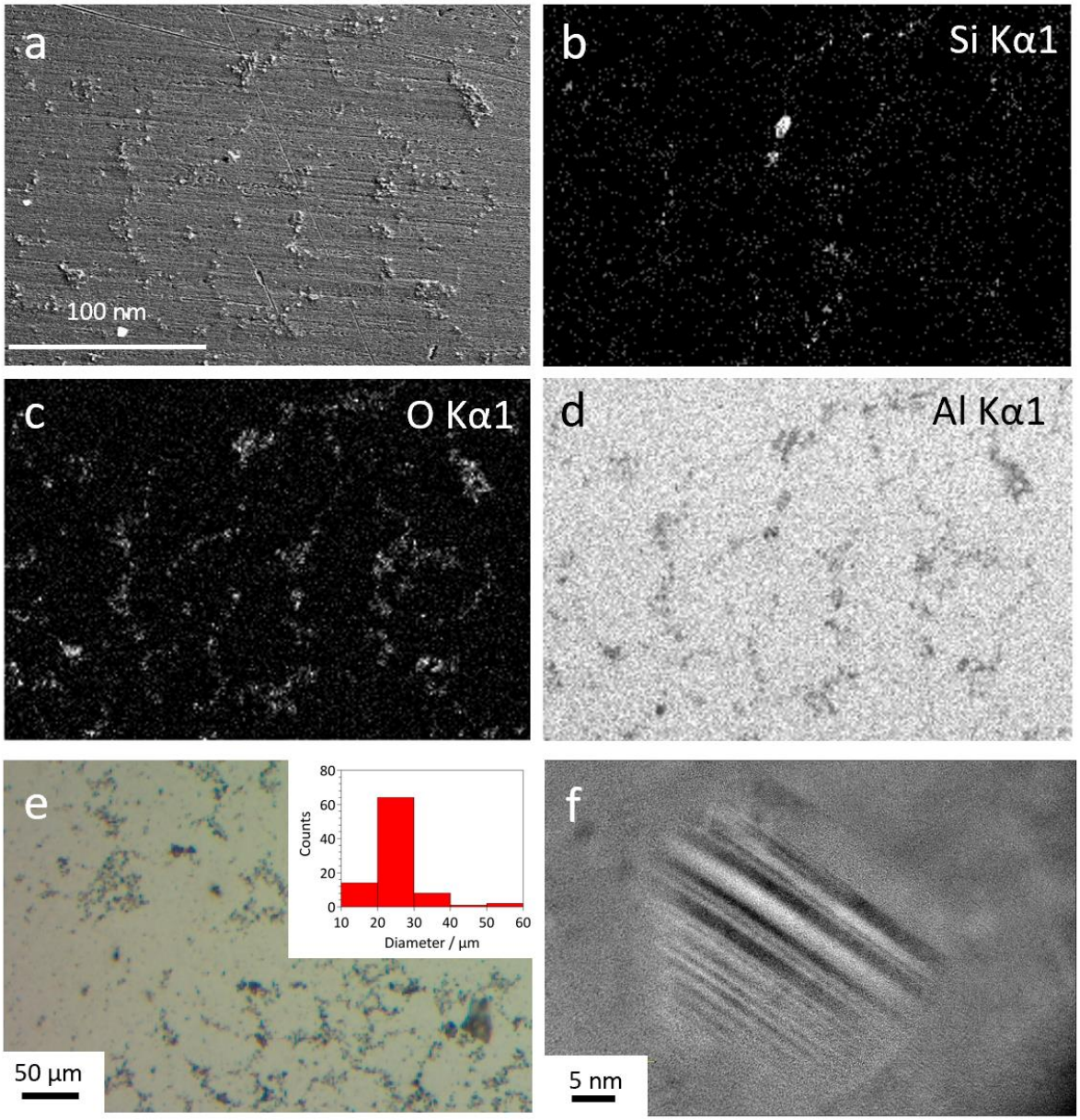

Figure 3.5. Microscopic images of a 0.8 vol% SiC-Al nanocomposite prepared with ultrasound treatment by Nb tip for 5 minutes and cooled down in liquid nitrogen. (a) SEM micrograph, (b-d) SEM-EDS mapping, (e) Optical microscopy image of the composite (inset shows the grain size distribution), (f) TEM image of a SiC nanocrystal in the composite.

Compared to HfB_2/Al composites, SiC-Al composites exhibited a larger Al grain size (figure 3.3a and 3.5e). This result suggests that HfB_2 creates more effectively heterogeneous nucleation sites of aluminum grains during cooling and solidification, which could be ascribed

to the local structural rearrangements caused by the semi-coherence of the interface between HfB_2 and Al and to the AlB_{12} interphase compared with the misfit between Al and SiC. Nanoparticles in HfB_2-Al composites are nonetheless more segregated than that in the SiC-Al composites, which could be ascribed to the strongly aggregated initial state of HfB_2 nanoparticles.

HfB_2-$AlSi_7Mg_{0.3}Cu_{0.5}$ nanocomposites

We have further assessed the possibility to prepare light weight matrix composites with the $AlSi_7Mg_{0.3}Cu_{0.5}$ foundry alloy. Considering the difficulties to decipher Si arising from the alloy from the one that may arise from incorporated SiC nanoparticles, only HfB_2-based nanocomposites were realized. A pellet consisting of pure Al and nanoparticles was prepared and incorporated in molten $AlSi_7Mg_{0.3}Cu_{0.5}$ at 600 °C. The melting of the pellet took around 5 minutes. Then, ultrasound treatment was applied for 5 minutes with an Nb tip. The solidification of the material was carried out using liquid nitrogen quenching.

The optical microscopy images (figure 3.6a) highlight the Si phase in dark grey colour. SEM-EDS mapping (figure 3.6b-g) suggests that hafnium is located in the grain boundaries rich in Si phase. According to the precedent results, it is not surprising that nanoparticles were segregated to the grain boundaries.

We also investigated the effects of the nanoparticles on the structure of the metal matrix during solidification. A pure aluminum pellet was added to $AlSi_7Mg_{0.3}Cu_{0.5}$ alloy and prepared by the same method (Appendix 3.9). Comparing the sample without treatment (Appendix 3.10) and the sample treated by ultrasounds (Appendix 3.9), we observed globular grain structures after ultrasound treatment. This phenomenon is in accordance with previous reports.[1,16,27] When the nanoparticles were incorporated to the alloy, the microstructure of the alloy was slightly refined, with Al grains of an average size of 90 μm. The globular shape was also modified. However, this behavior is less marked than with HfB_2-Al samples. As a matter of fact, the solute present in the alloy is responsible of constitutional undercooling during solidification, which plays a primary role in decreasing the size of the grains. The grain size in the alloy is then dominated by the composition of the alloy.

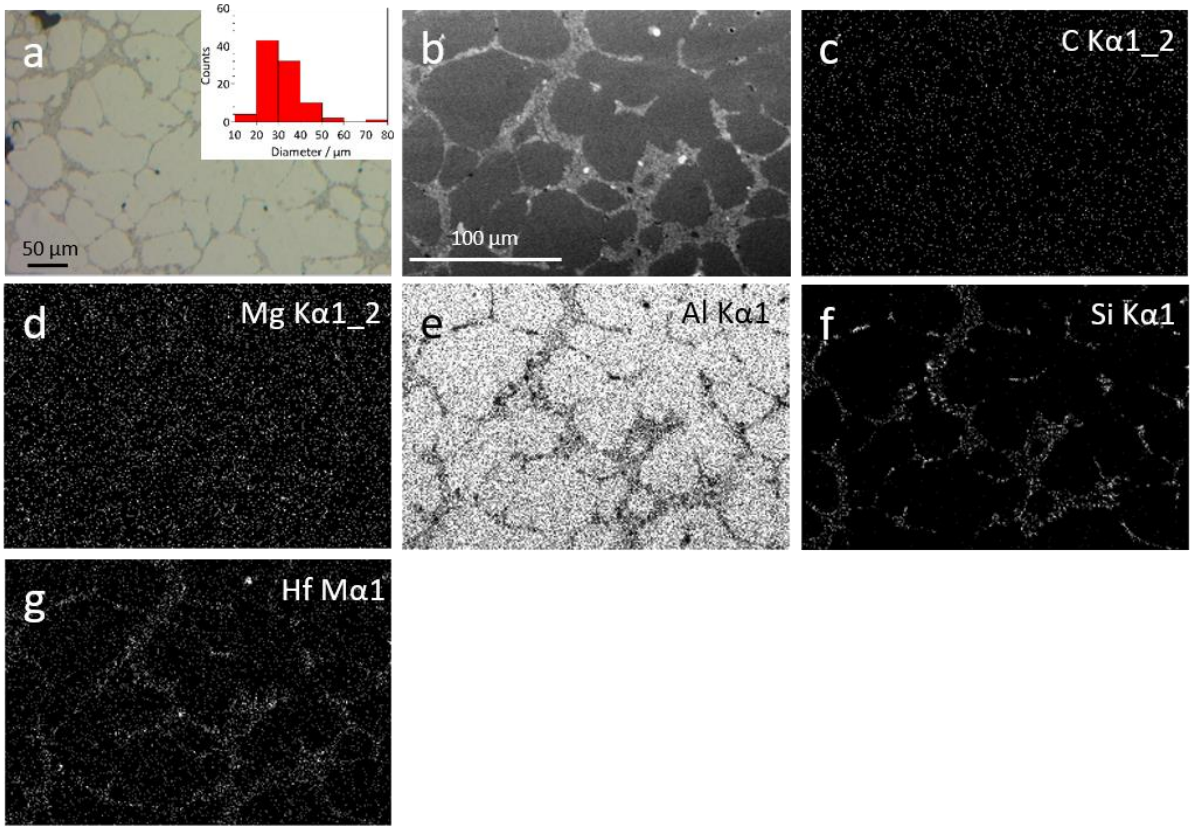

Figure 3.6. Microscopy observations for a 0.8 vol% HfB_2-$AlSi_7Mg_{0.3}Cu_{0.5}$ nanocomposite prepared with ultrasound treatment by Nb tip for 5 minutes and cooled down in liquid nitrogen. (a) Optical microscopy image and corresponding size distribution of Al grains, (b) SEM micrograph and (c-g) corresponding SEM-EDS maps

3.3.4 Decrease of the matrix grain size

Influence of different cooling rates on the microstructure of HfB_2 and SiC nanocomposites

As described earlier, wettability and viscous drag force are the key factors that may maintain the nanoparticles dispersed in the metal grains and enable them to resist the solidification front.[28] However, the control of the freezing conditions has also an influence on the microstructure. Increasing the cooling rate can form a refined network of nanoparticles by quenching the samples, thus leading to high modulus for the metal matrix grains.[29] Therefore, the microstructure was assessed for 0.8 vol% nanoparticles-Al nanocomposites obtained by three different cooling methods:

a) For samples heated in the resistive furnace, metallic samples are always inside an alumina crucible during cooling. Relatively slow cooling is achieved by air cooling of the quartz tube. The solidification time is 2 minutes from 720°C to 660°C. The cooling from operating temperature to room temperature takes 2 hours (around 6°C min^{-1}).

b) For samples heated in the induction furnace, only the metallic melts are heated, the crucible is only heated by contact with the Al melt. As the heating time is short (10 minutes), we expect that the crucible is colder than in the case of the resistive furnace and the cooling rate is then higher. The molten metal returned to the solid state in around 10 s after heating. The cooling from operating temperature to room temperature takes approximately 40 minutes (around 18°C min^{-1}).

c) Another series of samples was obtained by resistive heating and cooling relatively quickly by immersion in a liquid nitrogen bath. The sample was cooled to the temperature of liquid nitrogen (no more bubble appears) in 10 minutes, with a cooling rate of around 100 °C min^{-1}.

Firstly, the homogeneity of the microstructure was investigated. In conventional air freezing, the microstructure of the sample on the top, middle and bottom section was homogeneous. Nucleation occurs homogeneously inside the sample and Al grains grew in an anisotropic fashion. For the samples cooled by liquid nitrogen, presented in Appendix 3.11, the microstructure at the core of the sample remains homogeneous, but the top and the bottom areas show completely different morphologies. The homogeneous core might be due to the presence of an important temperature gradient between the core and the surface of the sample. It is accepted that liquid on the surface solidifies almost immediately when the sample is plunged in liquid nitrogen. Top view images showed large grains around 60 μm. In this region, the liquid metal was in contact with the alumina crucible, which is a low heat conductor. Fewer nucleation sites are formed at the low cooling rate region. The nucleated grains grow into a macroscopic grain during solidification. Thus, the 100 μm layer on the surface and in contact with the crucible are not considered for further analysis.

Analysis of the average grain size reveals a refinement of the microstructure with the increase of the heating rate. Indeed, 0.8 vol% HfB_2-Al samples cooled at different rates showed

an average grain size of 120, 78 and 20 µm for cooling rates 6, 18 and 100°C min^{-1}, respectively. (figure 3.7) SiC-Al nanocomposites also follow the same trend. Liquid nitrogen cooling is therefore proven to be the most efficient among the three methods assessed to refine the microstructure of MMnCs.

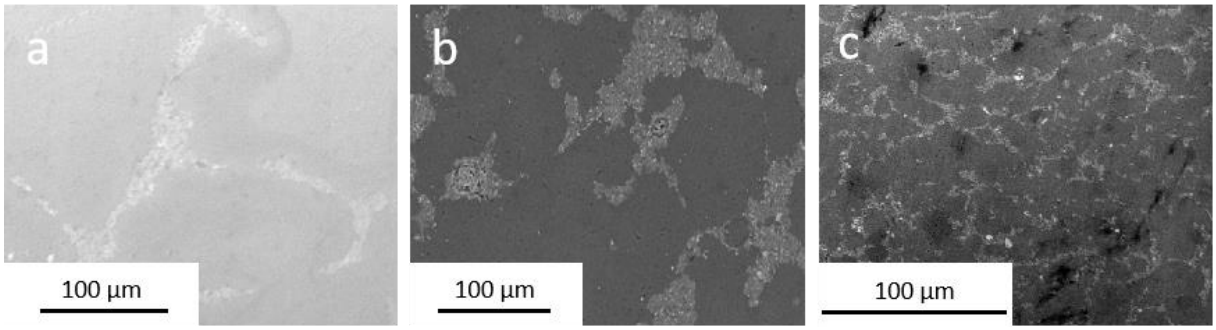

Figure 3.7. 0.8 vol% HfB_2/Al prepared with a cooling rate of (a) 6, (b)18 and (c) 100 °C min^{-1}

A common cooling method in the industry is water quenching. The difference between water quenching and liquid N_2 quenching has been studied in the course of this PhD work (appendix 3.12). Regarding the average grain size for different cooling methods, liquid nitrogen quenching showed similar grain refinement behavior (82 µm with natural cooling, 48 µm for water cooling and 41 µm for liquid nitrogen cooling). Considering the wide distribution of grain size, the difference between these two cooling methods was not significant. Even though the temperature of liquid nitrogen is much lower than that of water, the formation of N_2 bubbles at the surface of hot metal inhibits heat transfer and then decrease the cooling ability of liquid nitrogen, thus explaining the similar microstructure of water and N_2-cooled samples. Water cooling and liquid nitrogen cooling could both be applied with variable sets of parameters.

Influence of the inclusions load on the microstructure of nanocomposites

Aiming at improving the dispersion of nanoparticles, we compared a series of composites prepared at identical conditions (5 minutes ultrasound treatment by Nb tip, cooling by liquid nitrogen) but with different inclusion loads.

Optical microscopy images (Figure 3.8) indicated a surprising increase of grain size with the inclusion load. In line with previous SiC-Al nanocomposites without extra dispersion methods,[16] a volume ratio of 1.5 % is hard to achieve. This phenomenon might be explained by

macro-segregation observed e.g. in the samples at 2.4 vol% of inclusions. This phenomenon could relate to the viscosity and its impact on the dynamics of the solidification front during the solidification process. Therefore, a ratio of 0.8 vol% was kept as a model.

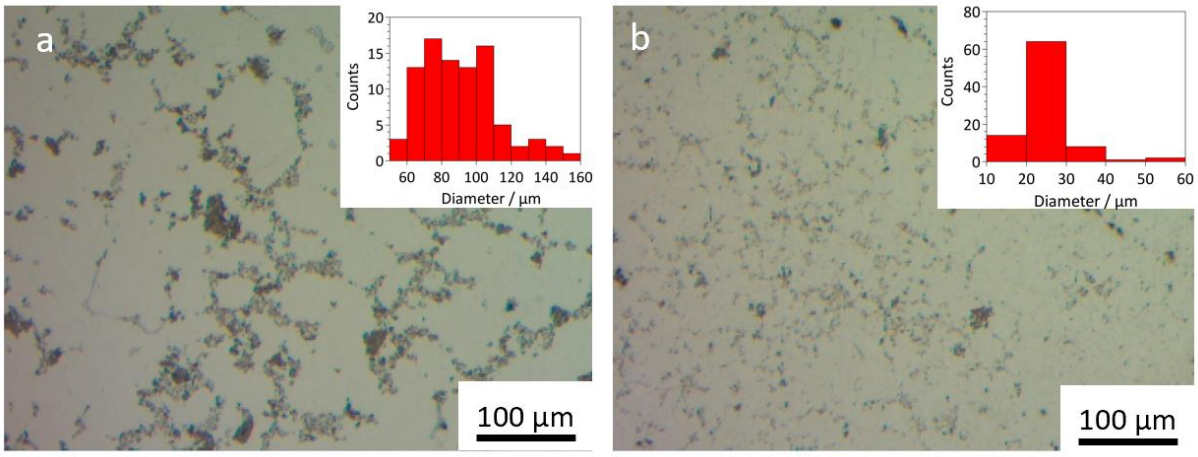

Figure 3.8. Optical microscopy images of 2.4 vol% SiC-Al (a) and 0.8 vol% SiC-Al

3.3.5 Mechanical tests

Microhardness measurements

The mechanical properties were firstly investigated by microhardness measurements and then compared to the pure reference samples prepared in the same way (table 3.2). For all experiments, the hardness at grain boundaries (rich in nanoparticles) was much higher than the value within the grain, as expected from the analysis of microstructure. Considering the inhomogeneity, an average of measurements on grain boundaries and inside the grains was also calculated.

Table 3.2. Microhardness tests for aluminum nanocomposites

Sample	Ultrasound treatment time	Cooling method	Average hardness (HV 0.05)	Average Al grains (HV 0.05)	Average grain boundaries (HV 0.05)	standard deviation (HV 0.05)
Al	5 minutes	Air, in crucible	24.9	/	/	1.3
0.8vol% HfB_2-Al	5 minutes	Air, in crucible	40.4	25.7	69.3	18.1
2.4vol% SiC-Al	5 minutes	Air, in crucible	45.9	32.9	78.9	22.2
0.8vol% HfB_2-Al	5 minutes	Liquid N_2	34.9	29.2	39.4	5.0
2.4vol% SiC-Al	5 minutes	Liquid N_2	43.3	36.1	52.0	5.4
0.8vol% HfB_2-Al	30 minutes	Liquid N_2	33.0	31.0	34.4	1.0
0.8vol% SiC-Al	30 minutes	Liquid N_2	40.9	33.2	52.7	4.9
Al-$AlSi_7Mg_{0.5}Cu_{0.5}$	30 minutes	Water	67.2	48.1	80.7	9.8
0.8vol% HfB_2-Al-$AlSi_7Mg_{0.5}Cu_{0.5}$	30 minutes	Water	71.7	51.7	91.6	12.8
$AlSi_7Mg_{0.5}Cu_{0.5}$			97.9	80.7	126.8	16.5
Al	5 minutes	Liquid N_2				
Al $AlSi_7Mg_{0.5}Cu_{0.5}$	5 minutes	Liquid N_2				
0.8vol% HfB_2-Al $AlSi_7Mg_{0.5}Cu_{0.5}$	5 minutes	Liquid N_2				

*HV 0.05: micro vickers hardness measured with a load of 0.05 kgf.

For nanocomposites containing 0.8 vol% of nanoparticles (SiC and HfB_2) sonicated for 30 min and quenched by liquid nitrogen, the measured hardness (table 3.2) for nanocomposites was notably greater than the hardness of the base material: average Hv_{SiC} = 40 HV and Hv_{HfB2} = 33 HV compared to 24 HV in pure Al. The increase of the hardness of > 40% is likely due to the presence of hard nanoparticles at the grain boundaries, which enhances the hardness of the final composites. In order to understand in more depth the mechanisms underlying hardness increase, it is worth characterizing average hardness values inside Al grain. The average Hv inside the Al grains for the sample 0.5vol% SiC-Al is 32.2 HV, higher than the value for pure Al (24 HV), this notable increase is more likely to be attributed to the presence of SiC

nanoparticles trapped inside the grains, as observed by TEM and discussed above. The average hardness of HfB_2-Al inside the grains has no significant improvement compared with that of pure Al, thus confirming full segregation of HfB_2 particles at grain boundaries. At fixed concentration, the average hardness for 0.8 vol% SiC nanocomposites was slightly greater than the hardness of HfB_2 nanocomposites. This is contrary to the Vickers hardness of bulk SiC and HfB_2, of 25.5 and 30.5 GPa, respectively.[11] The difference might be attributed to the following reasons: a) enhanced hardness of the grains due to SiC incorporation in the grains, b) inverse Hall-Petch occurring occurred for HfB_2 particles smaller than 10 nm.

When varying the concentration of SiC from 0.8 to 2.4 vol%, the average hardness of SiC-Al increases from 40 HV to 43 HV. The large standard deviations for these values must however be underlined. This may be explained by macro-segregation observed at 2.4 vol%. Samples processed with different ultrasound treatment period showed no significant change in hardness for 0.8 and 2.4 vol% SiC-Al samples. This result can be confirmed by their similar microstructure according to the microscopic images.

HfB_2 nanoparticles were dispersed in the $AlSi_7Mg_{0.3}Cu_{0.5}$ foundry alloy as well. When the two-step incorporation method was used, the foundry alloy and pure Al were mixed with a ratio of 1:1. As expected, the hardness of the reference sample prepared by this method without nanoparticles was lower than the hardness of the initial alloy (67.2 HV for the mixed alloy and 97.9 HV for the foundry alloy). The sample with nanoparticles shows similar hardness compared to the reference sample, with a hardness of 71.7 HV. Considering the high standard deviation around 10 HV, this difference is not significant. This result is in accordance with microscopy observations, where the Si-based solute of the alloy is responsible for the hardness, rather than incorporated nanoparticles.

Nanoindentation tests

We then sought deeper understanding of structure-property relationships in the nanocomposites by using nanoindentation to assess the mechanical properties of the matrix and of reinforcement nanoparticles. Based on the the microindentation results, 4 samples (tables 3.3 and 3.4) were analyzed to study the influence of the heterogeneous composition on the hardness and the elastic

modulus of nanocomposites at the sub-microscopic level. The results were compared with reference samples prepared in the same way in the absence of nanoparticles.

Table 3.3 Hardness from nanoindentation (at a depth of 3 μm).

Matrix	NPs	UT (min)	Cooling method	Hardness (GPa)			Hardness of central population (GPa)		
				Average	SD	Median	Average	SD	Median
Al (Ref)		5	Liquid N_2	0.43	0.03	0.42	0.43	0.02	0.42
Al	HfB_2, 0.8 vol% (3 wt%)	5	Liquid N_2	0.53	0.07	0.54	0.49	0.06	0.49
Al	SiC, 0.8 vol% (1 wt%)	30	Liquid N_2	0.52	0.07	0.52	0.52	0.03	0.52
Al	SiC, 2.4 vol% (3 wt%)	5	Liquid N_2	0.80	0.36	0.67	0.68	0.13	0.66
Al+ $AlSi_7Mg_{0.3}Cu_{0.5}$		5	Liquid N_2	0.77	0.14	0.71	0.74	0.06	0.72
Al+ $AlSi_7Mg_{0.3}Cu_{0.5}$	HfB_2, 0.8 vol% (3 wt %)	30	Liquid N_2	0.80	0.20	0.74	0.75	0.09	0.74

SD stands for standard deviation

The average of central population eliminates the 25% lowest values and the 25% highest values

Table 3.4. Elastic modulus from nanoindentation (at a depth of 3 µm).

Matrix	NPs	UT (min)	Cooling method	Elastic modulus (GPa)			Elastic modulus of central population (GPa)		
				Average	SD	Median	Average	SD	Median
Al (Ref)		5	Liquid N_2	79	2	79	79	0.5	79
Al	HfB_2, 0.8 vol% (3 wt%)	5	Liquid N_2	80	4	80	78	3	79
Al	SiC, 0.8 vol% (1 wt%)	30	Liquid N_2	79	2	78	76	1	78
Al	SiC, 2.4 vol% (3 wt%)	5	Liquid N_2	95	10	91	91	4	89
Al+ $AlSi_7Mg_{0.3}Cu_{0.5}$		5	Liquid N_2	88	3	88	88	1	88
Al+ $AlSi_7Mg_{0.3}Cu_{0.5}$	HfB_2, 0.8 vol% (3 wt %)	30	Liquid N_2	86	4	85	86	1	85

SD stands for standard deviation
The average of central population eliminates the 25% lowest values and the 25% highest values

As described in the previous section, SEM images and microindentation showed that the ultrasound treatment time has no significant effect on the microstructure and the hardness of the final material for both SiC and HfB_2 nanocomposites, and the hardness is largely related to the location of aggregates of nanoparticles. This allows us to compare samples prepared with different ultrasound treatment times. The mapping of the mechanical properties correlated with the optical image of the samples is helpful to distinguish the interior of the grains and grain boundaries. 400 measurements were achieved on a matrix of 21*19 with a distance of 10 µm at a depth of 1 µm (figure 3.9). The hardness of several areas could not be reliably measured (black pixels in the hardness maps and values equal to 0) due to the existence of micropores, especially for the sample at 2.4 vol% SiC-Al. These defects could be ascribed to the scratching of nanoparticles during polishing steps, or the presence of micropores in the sample. In fact, with the increase of the load, Al melt tends to be more viscous and micropores are more difficult to be eliminated, further investigations on SEM should be performed to confirm this. Figure 3.9

presents the mapping of mechanical properties of the 0.8% HfB_2-Al nanocomposite. A heterogeneous hardness distribution was observed: a population with a relatively homogeneous hardness corresponding to the grains and a second population significantly higher for the grain boundaries. Similar observations were made for other nanocomposites: SiC-Al and HfB_2-$AlSi_7Cu_{0.5}Mg_{0.3}$ (Appendix 3.14). The high hardness/modulus regions (grain boundaries) and low hardness/modulus regions (grains) will be discussed separately in the following sections.

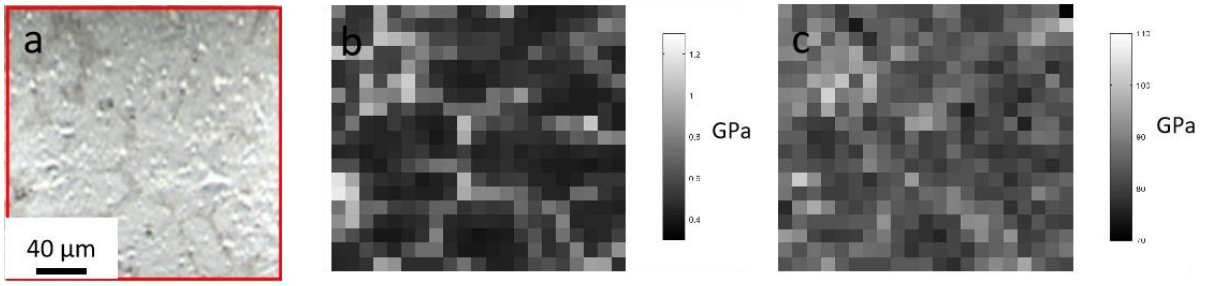

Figure 3.9 (a) Optical microscopy image, corresponding (b) hardness and (c) elastic modulus of a 0.8% HfB_2-Al nanocomposite.

Effect of the nature of nanoparticles on the hardness of pure Al. The hardness was recorded on nanocomposites, pure Al and Al alloy in a matrix of 6*5 with a depth of 3 µm (Table 3.3). The 0.8 vol% SiC-Al composite exhibited higher hardness than the 0.8 vol% HfB_2-Al sample, with values 0.52 and 0.49 GPa, respectively (table 3.3 and distribution figure 3.10a). These results were in agreement with microhardness tests, where nanocomposites containing the same volume percentage of SiC nanoparticles were harder than that of HfB_2. Measurements at a depth of 1 µm were performed 400 times to reach a statistical assessment of mechanical properties. The cumulative distribution curve (figure 3.10b) for the 0.8 vol% SiC-Al composite is above the curve for the 0.8 vol% HfB_2-Al sample, indicating that the reinforcement effect of SiC is more pronounced than HfB_2 on the hardness of the final nanocomposite. Nonetheless, HfB_2 still shows reinforcement of hardness properties compared to bare aluminum (figure 3.10b).

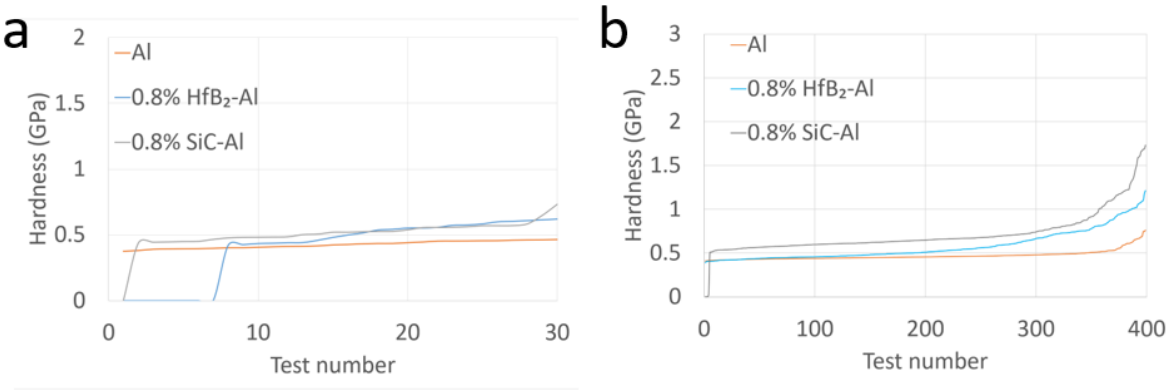

Figure 3.10. Statistic tests for hardness measured at (a) 3 µm and (b) 1 µm for reference Al, 0.8 vol.% HfB_2-Al and 0.8 vol.% SiC-Al

The grain matrix and the intergranular regions were then compared. Measurements at 1 µm depth revealed the reinforcement effect at the extreme surface. In low hardness regions, the middle of the plateau for 0.8 vol% SiC was higher than that of pure Al (0.6 GPa vs 0.43 GPa) (figures 3.10b and 3.11b). Hardness increases in the low hardness regions, correspond the matrix grain boundaries, implies trapping of part of the SiC nanoparticles inside Al grains, which is in accordance with TEM observations described above. Conversely, the hardness distribution for the 0.8 vol% HfB_2-Al at 1 µm depth (figure 3.10b) shows low-hardness regions with hardness values similar to pure Al around 0.45 GPa, confirming that most HfB_2 nanoparticles were segregated towards grain boundaries. The distribution curve for HfB_2-Al (figure 3.10b) deviates towards higher hardness than pure aluminum for more than 50% of measurements (from 200 to 400), which corresponds to reinforced area at grain boundaries according to mapping (figure 3.9). The average of this population is 0.66 GPa (calculated from the highest 200 measurements), clearly higher than pure Al. These measurements indicated that the reinforcement effect of HfB_2 nanoparticles occurs only at grain boundaries.

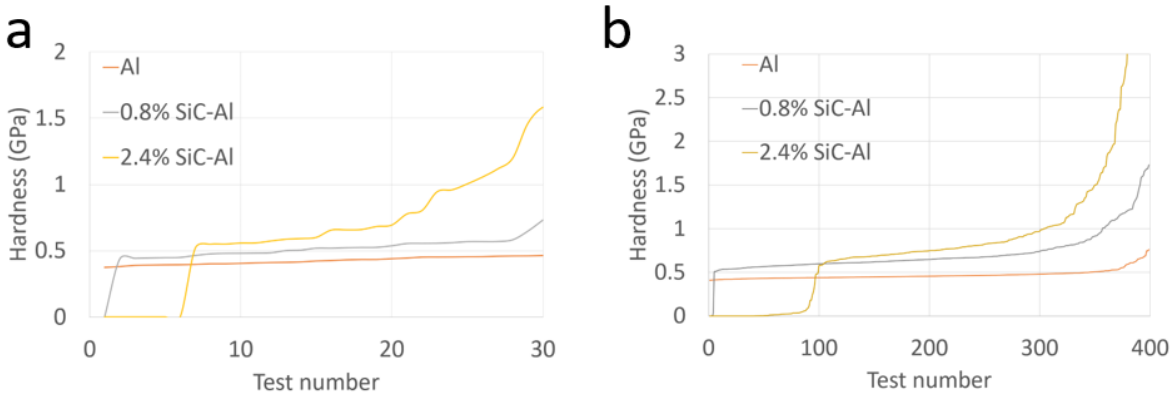

Figure 3.11. Statistical evaluation of hardness measured at 3 µm (a) and 1 µm (b) for 0.8 vol.% SiC-Al, 2.4 vol.% SiC and reference Al

Influence of the content of nanoparticles on the hardness of pure Al. The hardness measured at an indentation depth of 3 µm for the 2.4 vol% SiC-Al composite was on average 0.68 GPa (Table 3.3), significantly higher than for the 0.8 vol% SiC-Al sample. The hardness of 2.4 vol% SiC nanocomposites has been increased by 68% compared to the reference aluminum matrix. However, we should also notice that with the increase of inclusion content, the standard deviation is also higher. The extremely high hardness regions up to 3 GPa were found to be aggregates of SiC. This indicates that the microstructure is more heterogeneous, as observed in microscopy images (figure 3.8a).

Effect of nanoparticles on the hardness of foundry Al alloy. In the case of the $AlSi_7Mg_{0.3}Cu_{0.5}$ foundry alloy, a similar hardness has been observed: 0.79 GPa on average with 0.8 vol% HfB_2 nanoparticles, compared with 0.77 GPa for the reference (table 3.3). The large standard deviation of 0.2 GPa was mainly related to the different hardness values of Al grains and of Si-rich regions in the alloy. The distribution curves (figure 3.12) were drawn from 30 measurements at 3 µm (figure 3.12a) and 400 measurements at 1 µm (figure 3.12n). The latter show an overlapping between the bare matrix and the HfB_2-containing one in the 240 lowest hardness values. On the opposite, a deviation towards higher hardness values is observed for the highest 160 values, a similar fashion as for the Al matrix composites. The tangential midpoint of the distribution curves between the 250^{th} and 400^{th} measurements are 1.8 GPa for the sample with nanoparticles and 1.4 GPa for the reference matrix. Therefore, HfB_2

nanoparticles enhances the hardness, again at the grain boundaries (Appendix 3.14), consistent with the observations for the Al matrix composites.

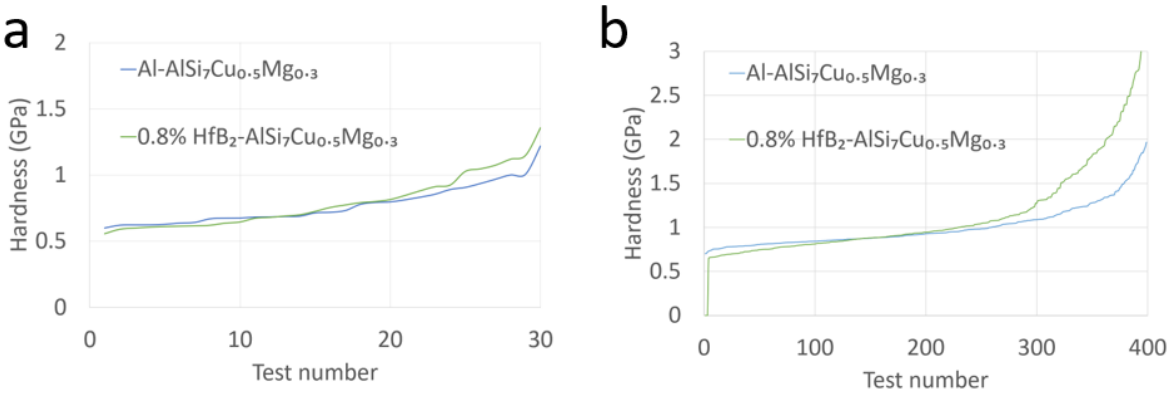

Figure 3.12. Statistic evaluation of hardness measured at 3 µm (a) and 1 µm (b) for reference Al-AlSi$_7$Mg$_{0.3}$Cu$_{0.5}$ and for the 0.8 vol.% HfB$_2$-Al-AlSi$_7$Mg$_{0.3}$Cu$_{0.5}$ nanocomposite

Effect of nanoparticles on the elastic modulus. The elastic modulus has also been measured by nanoindentation (Table 3.4). The mapping of the elastic modulus (figure 3.9) follows the same trend as the hardness mapping. Measurements at 1 µm depth (figure 3.13) reveal that the incorporation of 0.8% nanoparticles of HfB$_2$ and SiC could both improve the average elastic modulus by 13% and 16%, respectively. With the increase of SiC nanoparticles to 2.4%, segregated areas at grain boundaries showed high elastic modulus. On contrary, for measurements at 3 µm, samples containing 0.8% of nanoparticles showed similar elastic modulus with Al reference. The less obvious reinforcement effects at 3 µm could be attributed to the increased analysis volume, where the grain boundary effects are averaged out over the matrix grains. As the nanoindentation measurements (Figure 3.13 and 3.14) only focused on the local modulus, these results presented a high standard deviation and could only serve as a rough estimation of the property of final nanocomposite. Mechanical traction measurements are required to further evaluate the macroscopic behavior of the nanocomposites.

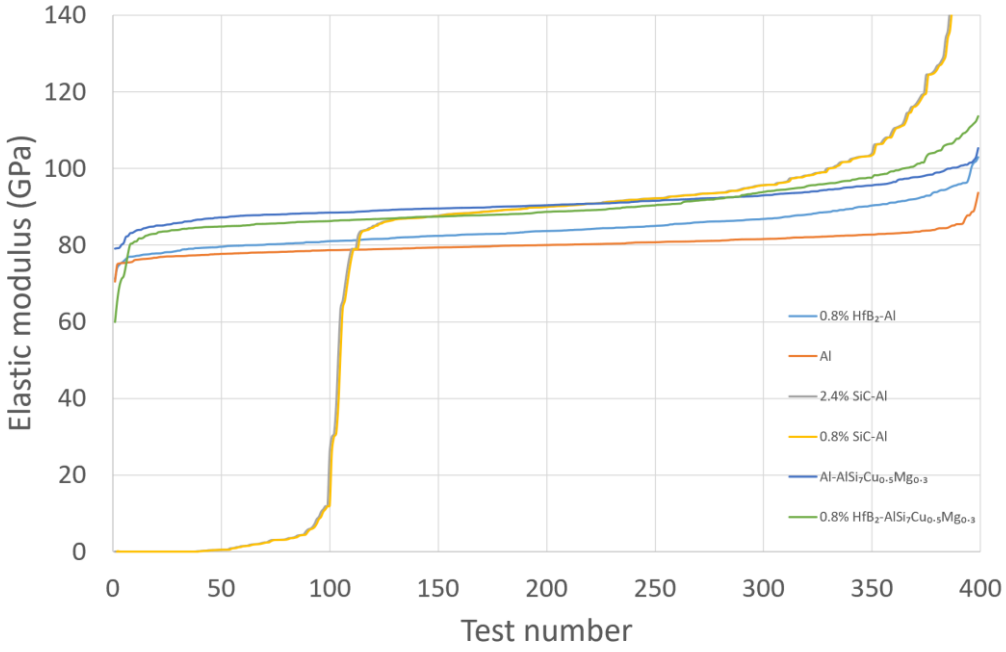

Figure 3.13. Elastic modulus measured at 1 µm

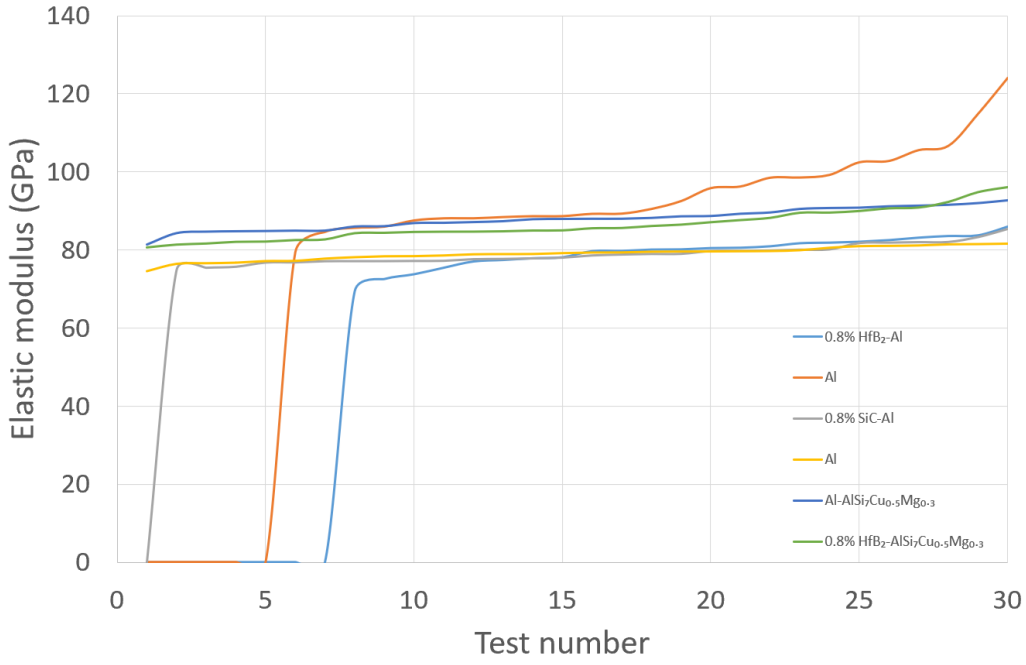

Figure 3.14. Elastic modulus measured at 3 µm

3.4 Conclusion

Herein we have incorporated silicon carbide nanocrystals and HfB_2 nanoparticles synthesized in molten salts in aluminum-based matrices by ultrasounds-assisted liquid metallurgy. Overall, the nanoparticles are stable after heating and aggregated at the grain boundaries. This segregation contributes to a refinement of the microstructure by decreasing the matrix grain size. Mechanical characterization by micro- and nano-indentation delineated the hardness and strength profiles of these composites. The hardness is heterogeneous at the sub-microscale, exhibiting a population with relatively homogeneous hardness corresponding to the matrix grains and a second population with significantly higher hardness for the intergranular zones. The reinforcement effect is less pronounced for HfB_2-based nanocomposites than for SiC-based samples, which could be ascribed to larger segregation of the boride particles at the grain boundaries. Indeed, inside the matrix grains, SiC nanocomposites are harder than pure aluminum, while the HfB_2-based nanocomposites show mechanical properties similar to the Al reference. This further confirms the poor dispersion of HfB_2 particles into aluminum, which is probably due to the initial aggregation state of the starting nanoparticles. Quenching the sample in liquid nitrogen allows refining the microstructure to limit the growth of the aluminum grains. Other quenching methods, previously developed to fabricate amorphous alloys[30] should be explored in the future to obtain better dispersed HfB_2-Al nanocomposite, as well as modified molten salt strategies to design less aggregated boride nanoparticles.

References

1. Casati, R. & Vedani, M. Metal Matrix Composites Reinforced by Nano-Particles—A Review. 65–83 (2014) doi:10.3390/met4010065.
2. Mohanavel, V., Suresh Kumar, S., Sathish, T. & Anand, K. T. Effect of ZrB2 content on mechanical and microstructural characterization of AA6063 aluminum matrix composites. *Mater. Today Proc.* **5**, 13601–13605 (2018).
3. Wang, F., Chu, K., Li, Y. biao & Wang, X. hu. Enhanced Interfacial Bonding and Mechanical Properties of Graphene/Cu Composites: A Matrix-Alloying Method. *Phys. Status Solidi Appl. Mater. Sci.* **215**, (2018).
4. Liu, X., Liu, Y., Huang, D., Han, Q. & Wang, X. Tailoring in-situ TiB2 particulates in aluminum matrix composites. *Mater. Sci. Eng. A* **705**, 55–61 (2017).
5. Liu, W., Cao, C., Xu, J., Wang, X. & Li, X. Molten salt assisted solidification nanoprocessing of Al-TiC nanocomposites. *Mater. Lett.* **185**, 392–395 (2016).
6. Cao, C., Ling, H., Murali, N. & Li, X. In-situ molten salt reaction and incorporation of small (10 nm) TiC nanoparticles into Al. *Materialia* **7**, (2019).
7. Nazari, M., Eskandari, H. & Khodabakhshi, F. Production and characterization of an advanced AA6061-Graphene-TiB2 hybrid surface nanocomposite by multi-pass friction stir processing. *Surf. Coatings Technol.* **377**, (2019).
8. Pan, S. *et al.* Effect of electron concentration on electrical conductivity in in situ Al-TiB2 nanocomposites. *Appl. Phys. Lett.* **116**, (2020).
9. Portehault, D., Delacroix, S., Gouget, G., Grosjean, R. & Chan-Chang, T. H. C. Beyond the Compositional Threshold of Nanoparticle-Based Materials. *Acc. Chem. Res.* **51**, 930–939 (2018).
10. Gupta, S. K. & Mao, Y. Recent Developments on Molten Salt Synthesis of Inorganic Nanomaterials : A Review. (2021) doi:10.1021/acs.jpcc.0c10981.
11. Xie, C. *et al.* Stable and hard hafnium borides: A first-principles study. *J. Appl. Phys.* **125**, (2019).
12. Estruga, M., Chen, L., Choi, H., Li, X. & Jin, S. Ultrasonic-assisted synthesis of surface-clean TiB2 nanoparticles and their improved dispersion and capture in al-matrix nanocomposites. *ACS Appl. Mater. Interfaces* **5**, 8813–8819 (2013).
13. Javadi, A., Pan, S. & Li, X. Fabrication of High Strength Al Nanocomposites with Populous TiB2 Nanoparticles. *Procedia Manuf.* **26**, 629–632 (2018).
14. Internal reference from PSA Groupe.
15. Portehault, D. *et al.* A General Solution Route toward Metal Boride Nanocrystals. *Angew. Chemie* **123**, 3320–3323 (2011).
16. Prasad Reddy, A., Vamsi Krishna, P., Narasimha Rao, R. & Murthy, N. V. Silicon Carbide Reinforced Aluminium Metal Matrix Nano Composites-A Review. *Mater. Today Proc.* **4**, 3959–3971 (2017).
17. Komarov, S. & Kuznetsov, D. Erosion resistance and performance characteristics of niobium ultrasonic sonotrodes in molten aluminum. *Int. J. Refract. Met. Hard Mater.* **35**, 76–83 (2012).
18. Luo, Z. P. Crystallography of SiC/MgAl2O4/Al interfaces in a pre-oxidized SiC reinforced SiC/Al composite. *Acta Mater.* **54**, 47–58 (2006).
19. Wang, X. The Formation of AlB2 in an Al-B Master Alloy. *J. Alloy. Comp.* **403**, 283–287 (2005).
20. Nautiyal, P., Gupta, A., Seal, S., Boesl, B. & Agarwal, A. Reactive wetting and filling

of boron nitride nanotubes by molten aluminum during equilibrium solidification. *Acta Mater.* **126**, 124–131 (2017).
21. Lü, S., Xiao, P., Yuan, D., Hu, K. & Wu, S. Preparation of Al matrix nanocomposites by diluting the composite granules containing nano-SiCp under ultrasonic vibaration. *J. Mater. Sci. Technol.* **34**, 1609–1617 (2018).
22. Hoekstra, J. & Kohyama, M. Ab initio calculations of the β-SiC(001)/Al interface. *Phys. Rev. B - Condens. Matter Mater. Phys.* **57**, 2334–2341 (1998).
23. Dehnavi, M. R., Niroumand, B., Ashrafizadeh, F. & Rohatgi, P. K. Effects of continuous and discontinuous ultrasonic treatments on mechanical properties and microstructural characteristics of cast Al413-SiCnp nanocomposite. *Mater. Sci. Eng. A* **617**, 73–83 (2014).
24. Lü, S., Xiao, P., Yuan, D., Hu, K. & Wu, S. Preparation of Al matrix nanocomposites by diluting the composite granules containing nano-SiCp under ultrasonic vibaration. *J. Mater. Sci. Technol.* **34**, 1609–1617 (2018).
25. Jia, S., Zhang, D., Xuan, Y. & Nastac, L. An experimental and modeling investigation of aluminum-based alloys and nanocomposites processed by ultrasonic cavitation processing. *Appl. Acoust.* **103**, 226–231 (2016).
26. Chen, L. Y., Peng, J. Y., Xu, J. Q., Choi, H. & Li, X. C. Achieving uniform distribution and dispersion of a high percentage of nanoparticles in metal matrix nanocomposites by solidification processing. *Scr. Mater.* **69**, 634–637 (2013).
27. Liang, G., Ali, Y., You, G. & Zhang, M. X. Effect of cooling rate on grain refinement of cast aluminium alloys. *Materialia* **3**, 113–121 (2018).
28. Chen, L. Y., Peng, J. Y., Xu, J. Q., Choi, H. & Li, X. C. Achieving uniform distribution and dispersion of a high percentage of nanoparticles in metal matrix nanocomposites by solidification processing. *Scr. Mater.* **69**, 634–637 (2013).
29. Xuan, Y. & Nastac, L. The role of ultrasonic cavitation in refining the microstructure of aluminum based nanocomposites during the solidification process. *Ultrasonics* **83**, 94–102 (2018).
30. Klement W, Willens RH, D. P. No TNon-crystalline structure in solidified gold–silicon alloys. itle. *Nature* **187(4740)**, 869–70 (1960).
31. Lei, W., Portehault, D., Dimova, R. & Antonietti, M. Boron carbon nitride nanostructures from salt melts: Tunable water-soluble phosphors. *J. Am. Chem. Soc.* **133**, 7121–7127 (2011).
32. Firestein, K. L. *et al.* High-strength aluminum-based composites reinforced with BN, AlB_2 and AlN particles fabricated via reactive spark plasma sintering of Al-BN powder mixtures. *Mater. Sci. Eng. A* **681**, 1–9 (2017).

Chapter 4
Metal matrix nanocomposites with improved thermal properties

ABSTRACT

Metal matrix nanocomposites with low melting point metal inclusions exhibit specific mechanical behavior and unique properties for thermal regulation. In this work, we designed aluminum nanocomposites consisting of phase change nanoparticles dispersed in an aluminum matrix *via* liquid-state processing techniques. To fabricate these composites, we prepared firstly core-shell Bi@SiO_2 nanoparticles by colloidal methods, as described in chapter 2. The nanoparticles were subsequently dispersed in liquid aluminum and the final composites obtained by quenching were characterized by XRD, SEM, TEM and XPS. We demonstrate that the silica shell acted as an efficient barrier against extensive coalescence of particles during the casting process, although the size distribution of bismuth nano-objects widened, which demonstrates mass transfer from one particle to the other. According to heat absorption properties measured by DSC, Bi@SiO_2-Al nanocomposites are able to store heat by melting through a wider range of melting temperatures centred at lower temperature than for the composite obtained without silica. These properties are stable upon cycling. The casting pathway based on core-shell metal-silica nanoparticles was then efficient to design a heat absorption material with low fabrication cost, thus paving the way to new thermal regulation materials.

4.1 Introduction

Phase change materials (PCMs) display a promising range of applications for the thermal control of electronic devices, since they can absorb/release latent heat from the solid-liquid phase transition.[1] The application for battery packs in electric vehicles is especially promising. Indeed, the temperature of Li-ion batteries should be controlled within a certain temperature range to ensure performance, cycling ability and safety. Phase change materials, compared to air/liquid cooling or heat pipe, use less power and they require less complex thermal system design.[2] Jaguemont et al.[3] have reviewed various PCM systems for battery applications and concluded that PCM could be a low-cost, efficient thermal solution if the conductivity of these materials could be improved. Thus, many studies have been performed by mixing phase change materials with metal matrix, possessing better thermal conductivity compared with common polymer matrices. Metallic materials can also provide better flame-retardant properties than organic phase change materials. For instance, metal (Al/Cu) foam coupled with organic PCM

improved cooling efficiency and decreased local heat accumulation.[4,5,6] Abraham et al.[7] have further tried to solve the problem of weakened structural strength when the inclusions melt, by creating an Al matrix nanocomposites with Bi inclusions encapsulated with Al_2O_3. The composite with inclusions encapsulated in alumina shell presents higher yield strength compared to the non-encapsulated sample, and is capable of retaining its structure during cycling. Such encapsulation strategy would then be efficient to increase the mechanical resistance of phase change materials. However, this strategy relies on the reduction of metal oxide (Bi_2O_3) by aluminum, which shows severe limitations. First, the working temperature is limited, as phase change only occurs at the melting temperature of bulk low melting point metal like Bi, Ga, In, Sn. Second, the composite has been fabricated by powder metallurgy which requires long preparation time and high fabrication costs. Further investigations are then needed to develop an alternative encapsulation method and to move the fabrication process to liquid metallurgy in order to reduce the cost.

To alleviate those constraints, we propose to fabricate metal matrix nanocomposites with phase change inclusions by ultrasonic-assisted melt processing: casting the metal matrix over its melting temperature, then dispersing the encapsulated low melting-point metal in the liquid metallic matrix by ultrasonic-assisted treatment.[8] The dispersion of core-shell $Bi@SiO_2$ in pure Al is studied herein as a proof of concept to assess the feasibility of the strategy and to study the reactions occurring between the nanoparticles core, shell and metal matrix under these harsh conditions. Here, aluminum was selected as a matrix due to its light weight, high thermal conductivity and high mechanical properties. Pure Al was used instead of industrial alloys in order to facilitate the understanding of the reactivity between the metal matrix and the inclusions. As Bi nanoparticles (melting point around 250 °C) are molten during the incorporation into the molten metal matrix (melting point 660 °C) and then show a high risk of coalescence, they were encapsulated in a silica shell prior to the composite preparation to prevent coalescence. The choice of silica as protective shell is motivated by polymer-based phase change materials, in which nanoencapsulation of phase change materials by silica has been proven to be an easy and efficient way to control the size of inclusion particles.[9] The synthesis of $Bi@SiO_2$-Al nanocomposites consists in three steps: synthesis of nanoparticles, growth of a silica shell and incorporation in molten metal matrix by ultrasonic-assisted process,

as schematically illustrated in fig. 4.1. The results were compared with a reference sample prepared from bare Bi nanoparticles into molten Al, without a protective shell.

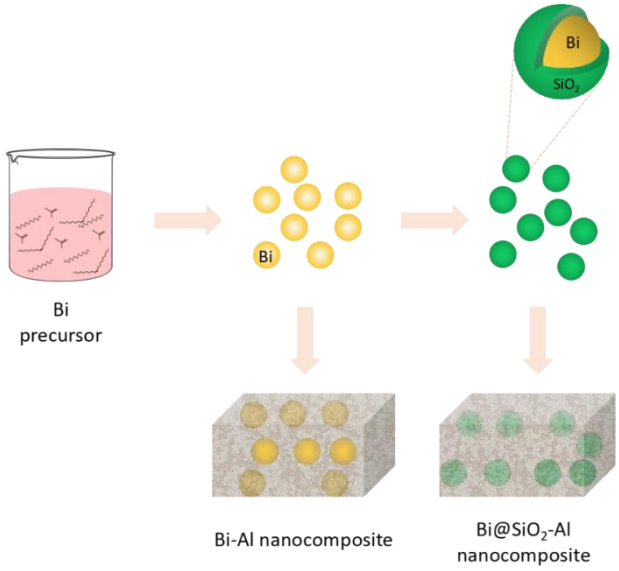

Figure 4.1 scheme of synthesis procedures

4.2 Experimental section

Materials

Bismuth acetate (99.99%), Oleylamine (technical grade, 70%), 1-dodenanethiol (98%), tetraethyl orthosilicate (TEOS, 99.99%), ammonia aqueous solution (28–30%) and aluminum powder (99.99%, 320 mesh) were all purchased from Sigma-Aldrich. Aluminum beads (99.9%, around 3mm diameter) were obtained from Alfa Aesar. The reagents were used as received.

Synthesis of bismuth nanoparticles and silica-coated bismuth nanoparticles

Bismuth nanoparticles were prepared by colloidal synthesis in a mixture of organic solvents based on a previous published protocol and already described in chapter 2.[10] Bismuth acetate (1 mmol) was mixed with 1- dodecanethiol (11.1 mL) and heated to 45 °C for 45 min under vacuum. The reaction flask was purged with N_2 and heated to 60 °C. Oleylamine (22.2 mL) at room temperature was quickly added under stirring and the reaction mixture was further heated for 24 h. Finally, Bi nanoparticles were washed two times by ethanol/chloroform

(20/1 vol./vol.) and re-dispersed in ethanol. The silica-coated bismuth nanoparticles were prepared by the classic Stöber method as follows[11]: tetraethyl orthosilicate (TEOS) was dissolved in absolute ethanol at a concentration of 0.38 M. 10 µL of TEOS solution and 100 µL of ammonia 30% were subsequently added to 1 mL alcoholic bismuth suspension [Bi] = 6.10^{-4} $mol.L^{-1}$ under vigorous agitation. The mixture was heated at 40 °C for 3 hours followed by washing by two cycles of centrifugation-redispersion in ethanol. The final powder was dried in a vacuum oven at 40 °C for 16 hours. In order to evaluate the thermal stability, 20 mg of $Bi@SiO_2$ nanoparticles were annealed in a Naberthem chamber furnace under air condition for 1 h dwell time with a heating rate of 10 °C/min.

Synthesis of Bi-Al nanocomposites

Bi-Al nanocomposites were prepared by ultrasound-assisted casting of a mixture composed of nanoparticles and Al in an induction oven. Briefly, 2 g of aluminum powders and alcoholic bismuth suspension were mixed by sonication at the boiling point for 1 hour to get stoichiometry ratio of 0.3 at. % between Bi and Al. Then the mixture was dried in a vacuum oven at 40 °C for 1 hour, followed by pressing into a 13 mm pellet under 8 tons for 2 minutes. Subsequently, the pellet and 0.4 g of pure Al beads were heated into an alumina crucible by an induction oven (CEIA, power cube 90 serie 200) at 740 °C under argon atmosphere. After dwelling for 1 minute, an ultrasound power of 80 watts (QSonica, Q500A-220, USA) was applied through a sonication horn (Nb tip with 4 mm diameter) to disperse the nanoparticles for 5 minutes. The final composite was obtained by cooling down the melt in the crucible. It was then cut with a diamond wire saw for further analyses.

X-ray diffraction

X-ray diffraction was performed with a D8 Bruker diffractometer operating at the CuKα radiation in the Bragg Brentano configuration. The ICSD reference 64709 was used for the indexation of bismuth nanoparticles.

Electron microscopy

The cut pieces of the samples were observed with scanning electron microscopy (SEM, Hitachi SU-70 microscope) equipped with an Oxford X-Max 50 mm^2 EDS detector. For preparation,

the samples were mounted in polyfast resin (Struers), followed by a series of polishing steps through 1000, 2400, 4800 grit papers (Buchler), then with 3 μm and 1 μm diamond suspensions.

For the observation of nanoparticles in transmission electron microscopy (TEM), the nanoparticles were dispersed in ethanol, then a drop was evaporated on a carbon-coated copper grid. For the composites, TEM thin films were prepared by a parallelepiped rectangle of 3*3*0.5 mm cut in the middle of the sample. Polishing was then performed with a diamond disk to get a 200 μm thick sample. The thickness of the centre of the slab was further reduced to 50 μm by using a precision dimpling instrument (Model 515, South Bay Technology). Ion milling was performed for the final thinning. TEM images were recorded on a Tecnai spirit G2 microscope operating at 120 kV. The STEM images and STEM-EDX mapping were recorded with a JEM 2100Plus UHR microscope and a Tecnai F20 that were both operating at 200 kV. The size distribution of precursor nanoparticles was determined by counting 150 to 200 nanoparticles from TEM images. The size distribution of nanoparticles in the final nanocomposites was determined by counting 70 to 120 particles, from SEM images and TEM images, respectively.

Chemical analysis by Wavelength dispersive X-ray fluorescence spectrometry (WDXRF)

Wavelength dispersive X-ray fluorescence (WDXRF) spectroscopy was performed on the cut pieces of the samples with a Bruker S8 Tiger spectrometer equipped with a Rh tube.

Differential Scanning Calorimetry (DSC)

The DSC analysis was performed in a TA Q20 DSC instrument. In a typical experiment, Around 10 mg of nanoparticles were sealed in an aluminum crucible. In the case of nanocomposites, top, middle and bottom slices of the samples (around 40 mg) were analysed separately to assess the homogeneity of the casted samples. To study the phase transition, the samples were heated to 320 °C and then cooled to 20 °C with a slope of 10 °C·min^{-1} followed by 3 minutes of stabilisation at 20 °C between each cycle. For each sample, At least 3 cycles were performed.

4.3 Results and discussion

4.3.1 Synthesis and characterization of Bi and Bi@SiO_2 nanoparticles

The first step of the composite preparation consists in the synthesis of size controlled bismuth nanoparticles (Figure 4.1), which was performed according the colloidal synthesis previously reported by Scheele et al.[10] The powder X-ray diffraction (XRD) patterns confirmed that Bi nanoparticles were obtained (Figure 4.2a). The TEM images (Figure 4.2b) showed that the sample consists in bismuth nanoparticles around 25 nm with a relatively narrow size distribution.

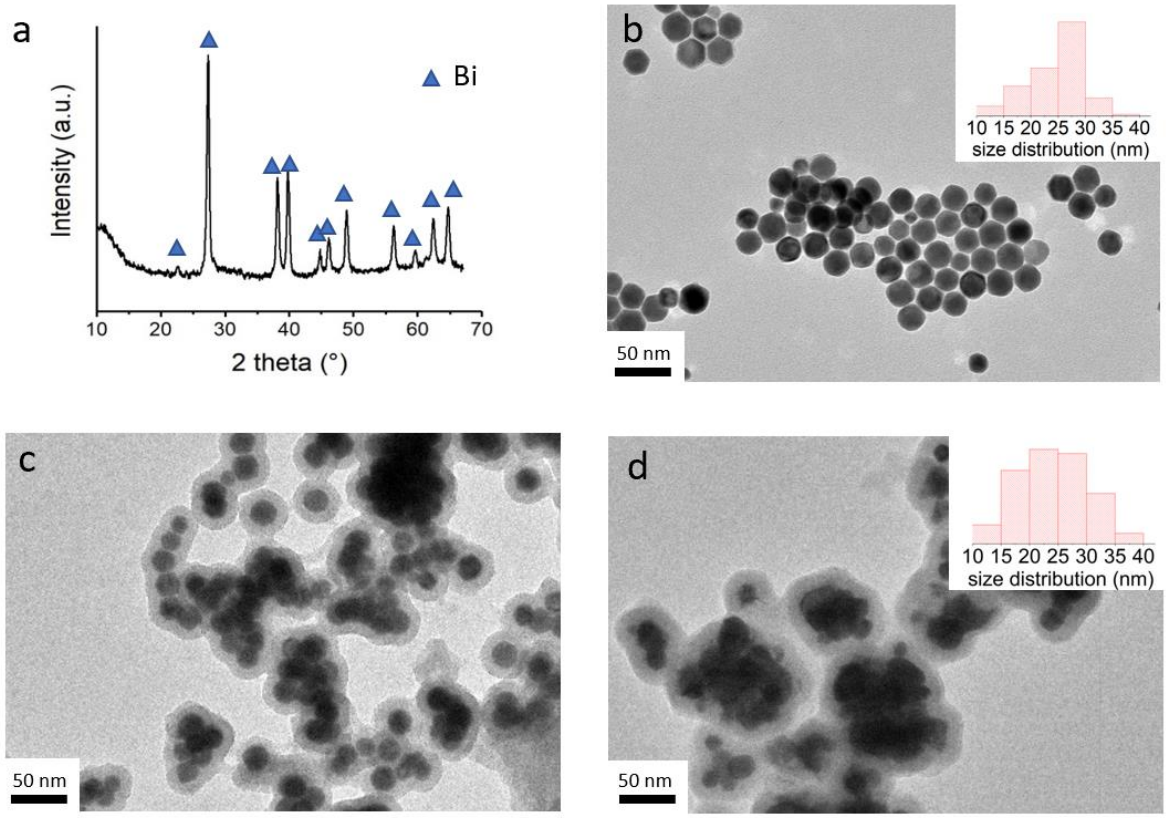

Figure 4.2. (a) Powder XRD pattern and (b) TEM images of Bi nanoparticles, (c) Bi@SiO_2 nanoparticles and (d) Bi@SiO_2 heated at 350 °C for 1 h. Insets in (b) and (d) show the corresponding size distributions of Bi core.

In a second step, the bismuth nanoparticles were coated with a 7 nm thick silica shell by the Stöber method,[11] as demonstrated by TEM, with a lower contrast for the shell than for the

Bi core (Figure 4.2c). TEM (Figure 4.2c) shows that the silica shell actually embeds clusters of several particles, forming aggregates of size up to 160 nm. This aggregation is usual for the encapsulation of small nanoparticles by Stöber process, as suspensions of nanoparticles smaller than 100 nm are poorly stable and show a strong tendency to aggregate in an alcoholic solution.[12] To demonstrate the stabilizing action of the silica shell against coalescence of the bismuth cores, we have heated the core-shell particles and sole bismuth nanoparticles without inorganic shells above the melting point of bulk Bi (271 °C). The bare Bi particles are not stable when heated at 320 °C and undergo extensive coalescence and growth. (Appendix 4.2) In the opposite, the silica shell preserves the Bi cores from coalescence and ensures that the Bi core size distribution is maintained (Figure 4.2d). Although Bi nanoparticles are aggregated inside the silica shell, their size has been preserved when heated over the melting point, thus allowing us to use them in further steps to study the stability of Bi nanoparticles in molten aluminum.

4.3.2 Synthesis and characterization of Bi@SiO_2-Al nanocomposite

Nanocomposites made of an aluminum matrix embedding Bi@SiO_2 (Bi@SiO_2-Al) and Bi (Bi-Al) nanoparticles were achieved by ultrasound-assisted casting. To ensure full incorporation of the nanoparticles in molten aluminum, aluminum and nanoparticles powders were firstly dispersed in ethanol by sonication. The mixture was then dried and pressed into a pellet with Bi loading of 0.25 at.%. The particles were then dispersed in aluminium at 740 °C by ultrasound treatment in an induction furnace that ensures efficient heating and melting of the aluminum matrix. The resulting samples showed metallic aluminum appearance (Appendix 4.1). The Bi/Al ratio was evaluated by WDXRF on the top, middle and bottom parts of each sample. It is about 0.3 at. % in all pieces, which is consistent with the initial precursor ratio and indicates that the nanoparticles are homogeneously distributed into the whole volume of the samples.

SEM images (Figure 4.3a) highlights white areas corresponding to electron-rich bismuth, with a size up to 120 nm. TEM (Figure 4.3b-d) evidences the existence of 10 nm (Figure 4.3b, c) and 60 nm (Figure 4.3d) nanoparticles of bismuth, as demonstrated by high resolution TEM (HRTEM, Figure 4.3c) and selected area electron diffraction (SAED) (Figure 4.3d). Bigger nanoparticles around 120 nm were also observed in TEM-HAADF images presented in Appendix 4.3. The statistical analysis of SEM and TEM images allows the

estimation of the size distributions at two different length scales. The TEM investigation of small nanoparticles displayed a distribution with a mean diameter of ca. 8 nm, while SEM investigation showed a wide distribution with an average of 60 nm. Particles below 10 nm showed spherical shape, while the shape of particles above 30 nm was irregular. Therefore, SEM and TEM evidence a widening of the size distribution from initial 25 nm Bi nanoparticles towards both smaller and larger particles. This behaviour is indicative the Ostwald ripening mechanism during the incorporation process, which indicates partial dissolution of bismuth into molten aluminum as expected from the Bi-Al binary phase diagram, which indicate a ca. 1.5 wt.% solubility of Bi in Al at 700 °C.[13] Note that sonication may also exacerbate Ostwald ripening, as already described on polymer composites.[14,15] In addition to the bismuth particles dispersed in the aluminum grains, we have identified thin Bi regions around 1 nm (Appendix 4.4 e,g) between aluminum grains and conformal to grain boundaries. We attribute this feature to bismuth segregation at the Al grains' solidification front during cooling down.

No silicon was detected by using STEM-EDS analysis on a single bismuth nanoparticle of diameter below 10 nm (Appendix 4.4f). Therefore, bismuth and/or silicon could migrate away from each other in molten aluminum.

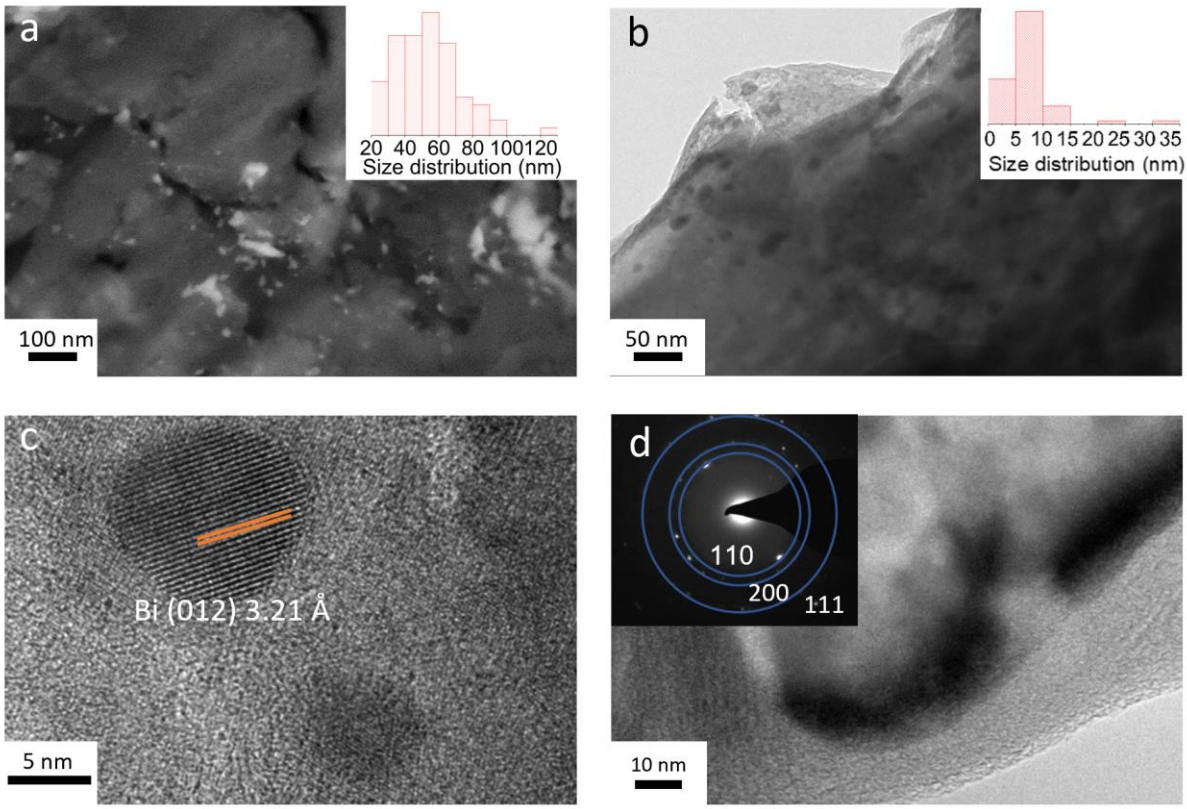

Figure 4.3 SEM and TEM characterization of a Bi@SiO_2-Al nanocomposite. (a) backscattered electron imaging-mode SEM image, bright and dark areas correspond to Bi and Al regions, respectively. (b)-(d) TEM images. Dark and light contrast correspond to Bi and Al, respectively. Insets in (a) and (b) show the corresponding size distributions. The inset in (d) shows the selected-area electron diffraction (SAED) pattern corresponding to image (d) and indexed along the structure of bismuth.

EDS mapping of an area containing a large coalesced bismuth object (figure 4.4a-f) showed that Bi was surrounded by an O-rich area also containing Al, but exempt of Si. Therefore, bismuth is surrounded by alumina. HRTEM (Figure 4.5a, orange square) next to the Bi particle in the Al/O-rich area indicates an Al/O rich rod-like region with non-uniform contrast which highlights crystal defects. The interplanar distance measured by HRTEM (Figure 4.5a,b) is consistent with Al_2O_3 (100) planes. Alumina should arise from aluminothermic reduction of the silica shell of the particles. Therefore, low oxidation state silicon species are expected to form concomitantly.

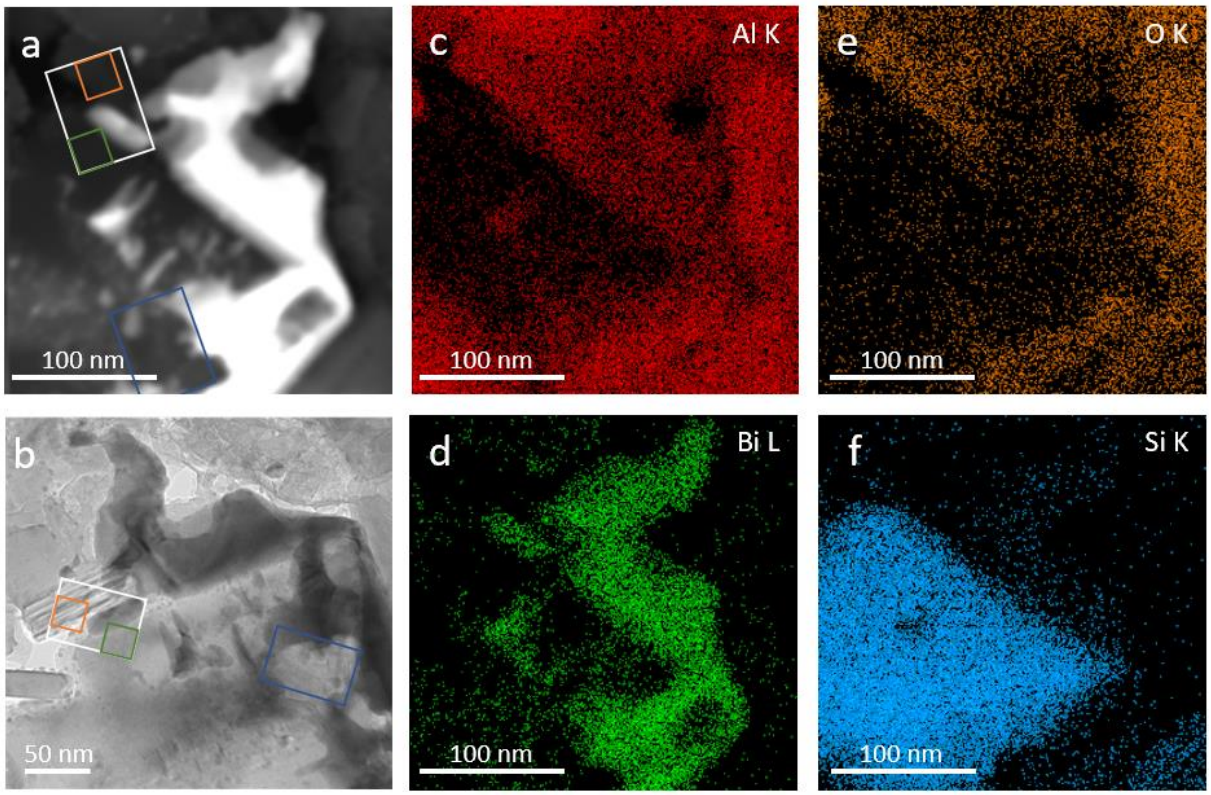

Figure 4.4. (a) STEM-HAADF, (b) STEM images and corresponding STEM-EDS maps of Bi@SiO_2-Al nanocomposite (c-f),

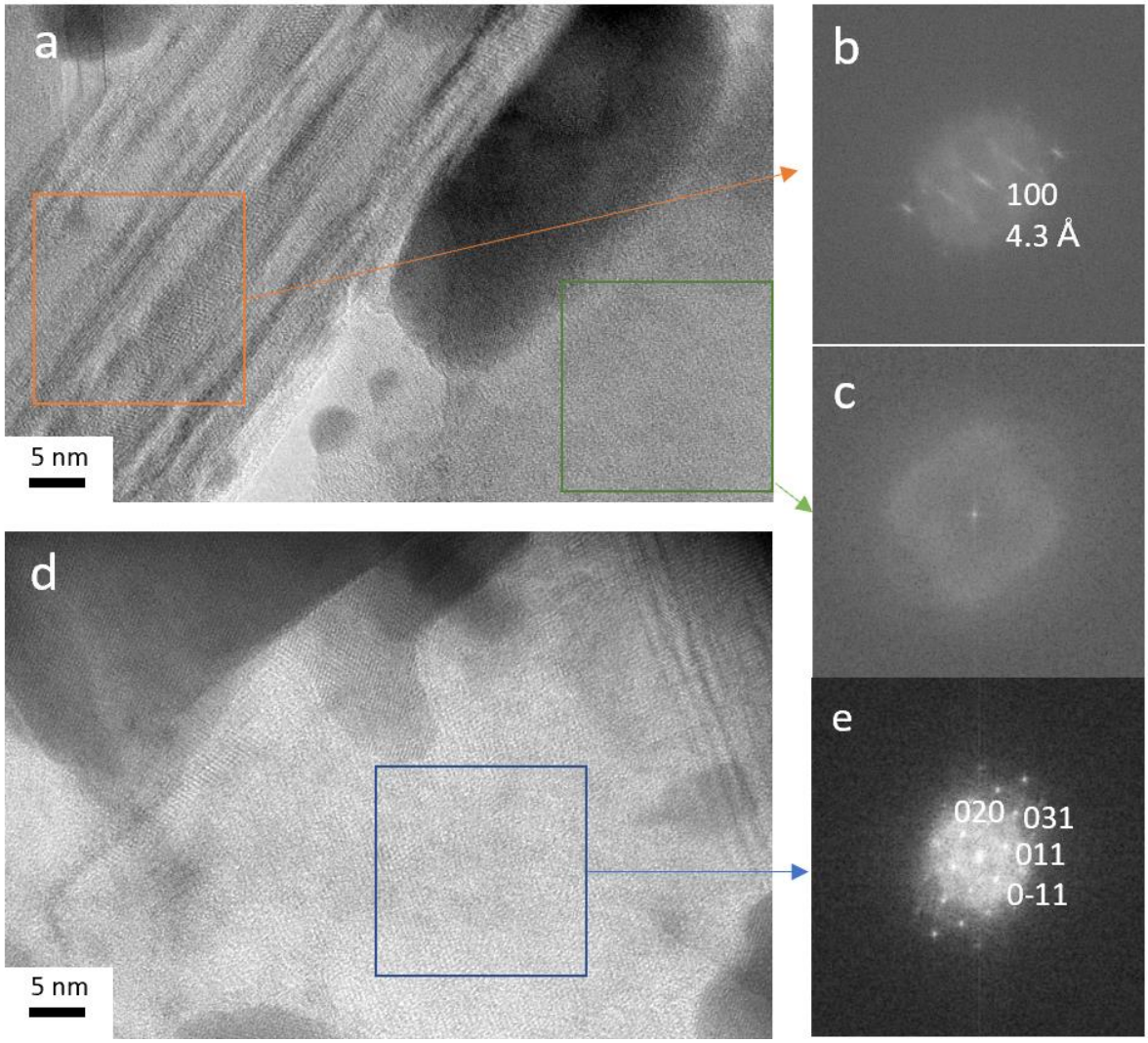

Figure 4.5. TEM images of the analyzed area. Image (a) was taken in the white rectangle in figure 4.4(a,b). The upper-left area corresponds to Al-O rich area and the bottom-right area corresponds to Si rich area. (b) shows the Fast Fourier Transforms (FFTs) corresponding to the orange square in (a) and indexed along the structure of Al_2O_3. (c) presents the FFT of the green square in (a). Image (d) was taken in the blue rectangle in figure 4.4(a,b). Image (e) was taken in the blue square in figure 4.4(b). Figure (e) shows the FFT corresponding to the dashed area in (d) and indexed along the structure of Al_2SiO_5.

The Si map (figure 4.4f) confirms that Si was no longer around Bi nanoparticles: Si migrated out of Bi nanoparticles towards a low contrast area (figure 4.4b and 4.5a,d) with no bismuth. The low overlap between Si and O-rich regions observed in the Si and O maps (figure 4.4f and 4.4e) is consistent with the formation of low oxidation state species of silicon from

aluminothermic reduction. We observed two regions in the Si-rich area: an amorphous-like area (figure 4.5a, green square), with corresponding FFT (figure 4.5c) showing no evidence of crystalline order; and a crystalline region (figure 4.5d, blue square). The corresponding FFT (figure 4.5e) corresponding FFT (Figure 4.5e) is fully consistent with the structure of sillimanite Al_2SiO_5.

EDS performed on a coalesced area (Appendix 4.4 a-d) indicates a Bi:Si atomic ratio of 0.2, well below the initial ratio of 2.0 in the pristine Bi@SiO_2 nanoparticles. This is in agreement with Bi and Si elements migrating away from each other during the incorporation of the particles.

In order to further understand redox processes involving the aluminum matrix and the silica shell, the surface states of a cut piece were analysed by XPS in the Si 2s (figure 4.6a) and Si 2p (figure 4.6b) regions. The spectrum of pure aluminum was recorded as a reference (figure 4.6). The Al plasmonic peak overlaps with the Si 2p binding energy regions between 99 eV and 102 eV (figure 4.6b). The Si 2s area was then chosen to identify the Si chemical states (figure 4.6a). Although a wide Al plasmon peak is also observed in the Si 2s region at 147.4 eV, it does not significantly overlap with the Si 2s signal at about 150-155 eV. For the Bi@SiO_2-Al composite (red line, figure 4.6a), the most intense peak at 155.1 eV is ascribed to the Si 2s binding energy for Si-O bonds of SiO_2.[16] We observe an additional contribution between 154 eV and 150 eV that is not observed for pure aluminum. This contribution is suggests the presence of other silicon species at lower binding energy than for SiO_2, which is consistent with low oxidation state Si species and/or an aluminosilicate.[17] Note that oxidation of low oxidation state Si species could also occur during the preparation of the sample for XPS measurements and exposure to the air. Hence, we can hypothesize that silicon may be more reduced in the pristine sample than indicated by XPS.

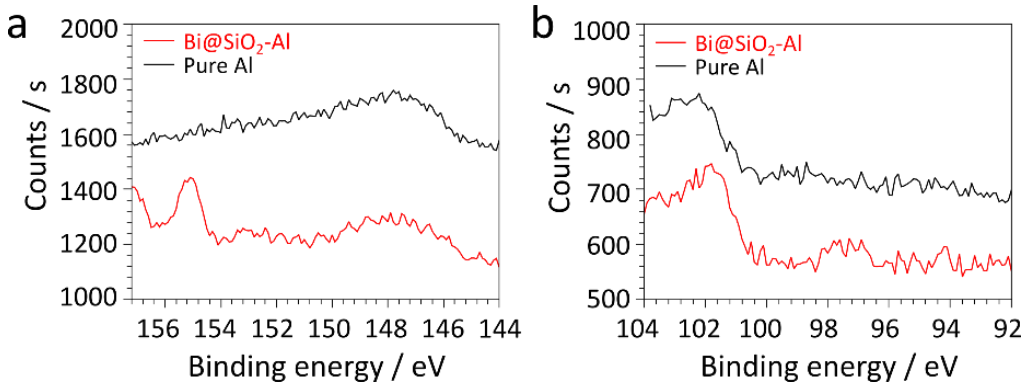

Figure 4.6. XPS analysis of Bi@SiO_2-Al nanocomposites (red) and pure Al (black). (a) shows the Si 2s area; (b) displays the Si 2p area.

The reduction process of SiO_2 (about 30 μm) by molten aluminum has been studied by Wang et al.[18] In the Al-SiO_2 system, the reduction of silica by aluminum is thermodynamically favourable (reaction 1 below). Once alumina is formed, it can react with silica and then form mullite or other aluminosilicates (reaction 2), evolving finally towards alumina and silicon (reaction 3).

$$4\ Al + 3\ SiO_2 \rightarrow 2\ Al_2O_3 + 3\ Si \quad (1)$$

$$3\ Al_2O_3 + 2\ SiO_2 \rightarrow Al_6Si_2O_{13} \quad (2)$$

$$8Al + 3Al_6Si_2O_{13} \rightarrow 13Al_2O_3 + 6\ Si \quad (3)$$

Wang et al.[18] also demonstrated that after 30 min of reaction at 700 °C after a 5 °C·min^{-1} heating rate, a 5 μm-thick shell of alumina was found surrounding unreacted silica particles, while silicon was within the aluminum matrix and formed rod-like Si inclusions. In our study, the silica component consisted in silica shell with a thickness of 7 nm, three orders of magnitude lower that the silica particle size investigated by Wang et al.,[18] which supports full reaction of the silica shell at a similar temperature. Nonetheless, aluminothermic reduction in our case is not complete as Si(IV) is not fully reduced in Si(0). On the opposite, the reaction is stopped at an intermediate stage, thus delivering an intermediate aluminosilicate. This behaviour can be attributed to shorter reaction times, as our experiments rely on induction heating at a rate of 350 °C·min^{-1} and reaction time of 10 min. We achieved sillimanite as intermediate phase. Generally, sillimanite forms above 776 °C,[19] 40 °C over the experimental heating temperature.

This high-temperature phase may be induced by intense local heating provided by ultrasound treatment.[20]

The formation of an aluminosilicate should be accompanied with the silicon, although no crystallized silicon was observed by TEM. The amorphous-like area we have highlighted (green square in STEM-EDS mapping in figure 4.4a,b and figure 4.5a) is then attributed to amorphous silicon. Note that this area could also correspond to crystalline silicon with an orientation away from diffraction conditions. Further analysis needs to be performed to confirm this.

Overall, we propose the following reaction mechanism: the pristine silica shell is reduced by aluminum that is concomitantly oxidized and reacts with remaining silica to form an aluminosilicate intermediate. During ultrasound-assisted heating for the nanocomposite preparation, the silica shell separates from the Bi core during, leading to leaching of Bi droplets which then undergo Ostwald ripening and develop into two populations.

4.3.3 Synthesis and characterization of Bi-Al nanocomposite

A comparative study of uncoated Bi nanoparticles dispersed in molten aluminum was performed. Figure 4.7 displays the HAADF and TEM images of such a Bi-Al composite. Similar to the observations made for the Bi@SiO_2-Al composite, the particle size evolved towards two populations due to Ostwald ripening: coalesced particles around several micrometres and detached particles around 5 to 30 nanometres. Thus, the particle size was no longer maintained at the nanoscale.

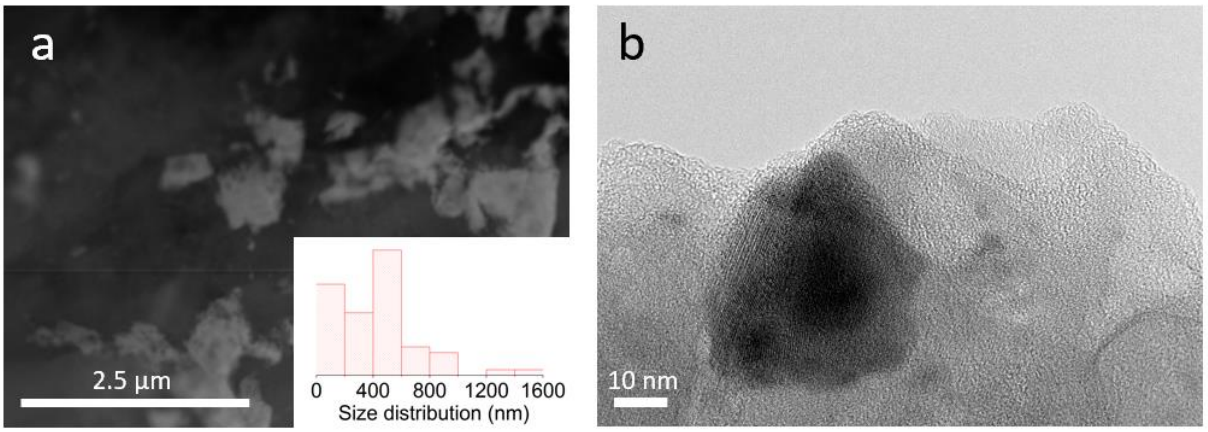

Figure 4.7. HAADF (a) andTEM image(b) of a Bi-Al nanocomposite and size distribution.

The comparison between Bi-Al and Bi@SiO_2-Al samples show that although the silica shell underwent chemical reaction and local mobilisation, it acted efficiently against coalescence of the cores occurring in the sample without protective shell. Consequently, a nanocomposite with wide size distribution at the nanoscale was generated.

4.3.2 Heat absorption ability evaluated by DSC measurements

DSC analysis for nanoparticles

To assess the heat absorption ability, DSC was performed for both precursor nanoparticles and final nanocomposites. Figure 4.8 displays the melting behaviour of the 3rd heating cycle for pristine Bi and Bi@SiO_2 nanoparticles. Bi@SiO_2 showed an endothermic peak at ~242 °C, lower than the melting temperature of bulk Bi at 271.3°C, which is in agreement with the depression of the melting point with particle size decrease.[21] The melting point measured for 25 nm silica coated Bi nanoparticle is in accordance with the results of Bi-carbon nanocomposites.[22] Contrary to the similar melting behaviour for Bi@SiO_2 nanoparticles upon cycling (figure 4.8b), the bare bismuth particles displayed a small exothermic peak at ~245 °C, followed by two sharp endothermic peaks at ~263 °C and 271 °C after 3 cycles, the latter corresponding to bulk Bi melting. The first two endothermic peaks are attributed to the melting temperature depression with the particle size.[21] The appearance of the peaks at higher temperature indicates that the nanoparticles coalesced and large particles up to bulk were

formed. The results for both samples are consistent with TEM observations after analysis. (Appendix 4.2)

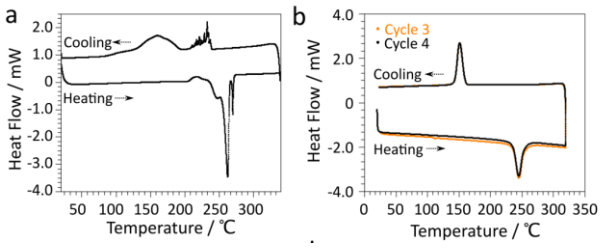

Figure 4.8. Differential Scanning Calorimetry (DSC) analysis of Bi (a) and Bi@SiO_2 (b) nanoparticles

DSC analysis for nanocomposites with phase change inclusions

The DSC curves for the composites (Figure 4.9a) also show endothermic peaks during heating and an exothermic peak during cooling indicating solidification of undercooled bismuth. The high temperature regions of DSC curves (Figure 4.9b) show that the melting peaks significant differ from those for the initial particles described above. The Bi@SiO_2-Al nanocomposite exhibits two endothermic peaks with an onset temperature at 251°C: a broad melting peak at 263 °C corresponding to nanoparticles' melting and a low intensity sharp peak at 271 °C corresponding to bulk bismuth. The shift of these peaks to higher temperatures compared to unreacted nanoparticles confirms that some of the nanoparticles coalesced during the incorporation of the particles in the melt. The enthalpy ratio for the peaks at 263 °C and at 271 °C is 9:1, indicating that around 90% of Bi element are still nanoscaled, assuming that the melting latent heat of nanoscale Bi is close to the value for bulk Bi. The heat absorption ability evaluated by the enthalpy of the melting process was 0.38 $J \cdot g^{-1}$, close to the expected value based on the chemical composition at 0.47 $J \cdot g^{-1}$ and the melting latent heat fo bulk Bi. This value is 100 times lower compared to Bi@Al_2O_3-Al prepared by powder metallurgy,[23] but we may improve it by increasing the amount of inclusion particles within the matrix. DSC over 15 consecutive heating-cooling cycles between 20 and 300 °C shows the cycling ability of the Bi core after melting, as the DSC curves remained unchanged during cycling.

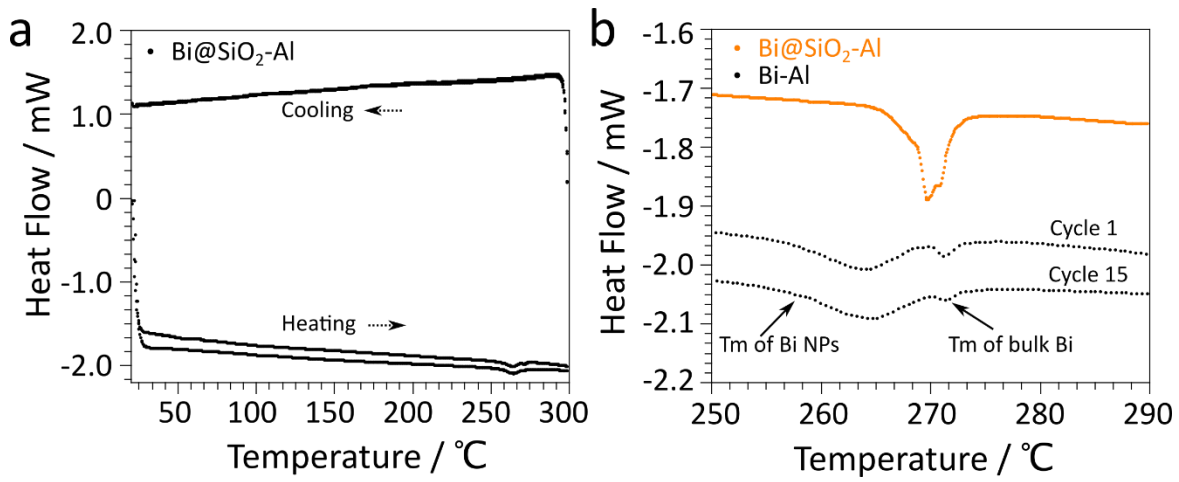

Figure 4.9. DSC analysis of a Bi@SiO2-Al nanocomposite (a) with zoom in the area 250-290 °C during heating (b). for the 1st and 15th cycles. The DSC analysis of a reference Bi-Al sample is also shown for the first cycle in (b) (orange).

We did not detect by DSC the phase change of small nanoparticles around 8 nm expected from TEM observations, which occurred at around 240 °C in Ag matrix.[21] This could be explained by the decreased enthalpy with the particle size[24] or the low volume fraction of nanoparticles smaller than 10 nm. These hypothesis need to be studied by further experiments.

DSC further confirms the efficient role of the silica shell to limit the coalescence of Bi nanoparticles, since the Bi-Al nanocomposite showed three endothermic peaks at 262, 269 and 271 °C overlapping together and shifted to higher temperature compared to the Bi@SiO2-Al nanocomposite, which implies the progressive coalescence of nanoparticles into bulk particles during cycling.

Compared to a Bi-Al composite prepared by powder metallurgy[7] at the same heating rate and with micron and nano-sized bismuth inclusions, the distribution of melting temperatures for Bi@SiO2-Al prepared by our liquid metallurgy process is broader and shifted to lower temperatures. This demonstrates a decreased Bi particle size achieved through our protocol. The small initial nanoparticle size, the protective silica shell, the ultrasound treatment induced disruption of Bi droplets and rapid thermal treatments by induction heating are the keys to achieve small inclusion nanoparticles with a wide phase transition temperature range, which

is a considerable advantage for the final application as they can provide progressive heat absorption in a wide temperature range.

4.4 Conclusions

In conclusion, we have successfully developed an ultrasound assisted casting synthesis of phase change metal matrix nanocomposites. The phase change nanoparticles were embedded within a silica shell, which acts as a barrier against extensive coalescence of the metal cores, which are molten during the incorporation process.

We have made several attempts for *in situ* fabrication of $Bi/Al_2O_3/Al$ by ultrasound-assisted casting method (see Appendix S4.1 and S4.2). The formation of encapsulated inclusions by aluminoreduction proved difficult to be applied to other types of inclusions such as $In/Al_2O_3/Al$: the reaction conditions must be adjusted with the Gibbs free energy for the formation of metal oxide. An additional challenge of prime importance relates to the decrease of the melting point of the PCM nanoparticles. Reaching other phase transition temperatures with metal alloy inclusions will require an indepth work in the future. We believe that such light-weight aluminum-based functional materials with high heat dissipation ability, wide and tunable phase transition temperature and low fabrication costs will be a relevant model from the point of view of thermal control of vehicle battery.

References

(1) Wu, M. S.; Liu, K. H.; Wang, Y. Y.; Wan, C. C. Heat Dissipation Design for Lithium-Ion Batteries. *J. Power Sources* **2002**, *109* (1), 160–166. https://doi.org/10.1016/S0378-7753(02)00048-4.

(2) Offer, G.; Patel, Y.; Hales, A.; Bravo Diaz, L.; Marzook, M. Cool Metric for Lithium-Ion Batteries Could Spur Progress. *Nature* **2020**, *582* (7813), 485–487. https://doi.org/10.1038/d41586-020-01813-8.

(3) Jaguemont, J.; Omar, N.; Van den Bossche, P.; Mierlo, J. Phase-Change Materials (PCM) for Automotive Applications: A Review. *Applied Thermal Engineering*. Elsevier Ltd March 2018, pp 308–320. https://doi.org/10.1016/j.applthermaleng.2017.12.097.

(4) Qu, Z. G.; Li, W. Q.; Tao, W. Q. Numerical Model of the Passive Thermal Management System for High-Power Lithium Ion Battery by Using Porous Metal Foam Saturated with Phase Change Material. *Int. J. Hydrogen Energy* **2014**, *39* (8), 3904–3913. https://doi.org/10.1016/j.ijhydene.2013.12.136.

(5) Alipanah, M.; Li, X. Numerical Studies of Lithium-Ion Battery Thermal Management Systems Using Phase Change Materials and Metal Foams. *Int. J. Heat Mass Transf.* **2016**, *102*, 1159–1168. https://doi.org/10.1016/j.ijheatmasstransfer.2016.07.010.

(6) Wu, W.; Yang, X.; Zhang, G.; Ke, X.; Wang, Z.; Situ, W.; Li, X.; Zhang, J. An Experimental Study of Thermal Management System Using Copper Mesh-Enhanced Composite Phase Change Materials for Power Battery Pack. *Energy* **2016**, *113*, 909–916. https://doi.org/10.1016/j.energy.2016.07.119.

(7) Abraham, A.; Schoenitz, M.; Dreizin, E. L. Energy Storage Materials with Oxide-Encapsulated Inclusions of Low Melting Metal. *Acta Mater.* **2016**, *107*, 254–260. https://doi.org/10.1016/j.actamat.2016.01.074.

(8) Mohanty, P.; Mahapatra, R.; Padhi, P.; Ramana, C. H. V. V.; Mishra, D. K. Ultrasonic Cavitation: An Approach to Synthesize Uniformly Dispersed Metal Matrix Nanocomposites—A Review. *Nano-Structures and Nano-Objects* **2020**, *23*, 100475. https://doi.org/10.1016/j.nanoso.2020.100475.

(9) Shchukina, E. M.; Graham, M.; Zheng, Z.; Shchukin, D. G. Chem Soc Rev Nanoencapsulation of Phase Change Materials for Advanced Thermal Energy Storage Systems. **2018**, 4156–4175. https://doi.org/10.1039/c8cs00099a.

(10) Scheele, M.; Oeschler, N.; Meier, K.; Kornowski, A.; Klinke, C.; Weller, H. Synthesis and Thermoelectric Characterization of Bi2Te 3 Nanoparticles. *Adv. Funct. Mater.* **2009**, *19* (21), 3476–3483. https://doi.org/10.1002/adfm.200901261.

(11) STOBER, W. Sagittal Plane Spinal Mobility Is Associated with Dynamic Balance Ability of Community-Dwelling Elderly People. *J. Colloid Interface Sci.* **1968**, *26* (1), 62–69. https://doi.org/10.1016/0021-9797(68)90272-5.

(12) Wang, J.; Shah, Z. H.; Zhang, S.; Lu, R. Silica-Based Nanocomposites via Reverse Microemulsions: Classifications, Preparations, and Applications. *Nanoscale* **2014**, *6* (9), 4418–4437. https://doi.org/10.1039/c3nr06025j.

(13) Manasijević, D.; Minić, D.; Balanović, L.; Premović, M.; Gorgievski, M.; Živković, D.; Milisavljević, D. Experimental Investigation and Thermodynamic Prediction of the Al–Bi–In Phase Diagram. *J. Alloys Compd.* **2016**, *687*, 969–975. https://doi.org/10.1016/j.jallcom.2016.06.262.

(14) Thompson, J. A.; Chapman, K. W.; Koros, W. J.; Jones, C. W.; Nair, S. Sonication-Induced Ostwald Ripening of ZIF-8 Nanoparticles and Formation of ZIF-8/Polymer

Composite Membranes. *Microporous Mesoporous Mater.* **2012**, *158*, 292–299. https://doi.org/10.1016/j.micromeso.2012.03.052.
(15) Dirix, Y.; Bastiaansen, C.; Caseri, W.; Smith, P. Preparation, Structure and Properties of Uniaxially Oriented Polyethylene-Silver Nanocomposites. *J. Mater. Sci.* **1999**, *34* (16), 3859–3866. https://doi.org/10.1023/A:1004614604641.
(16) Barr, T. L. An XPS Study of Si as It Occurs in Adsorbents, Catalysts, and Thin Films. *Appl. Surf. Sci.* **1983**, *15* (1–4), 1–35. https://doi.org/10.1016/0378-5963(83)90003-X.
(17) Hughes A.E., Hedges M.M., S. B. A. Reactions at the Al/SiO2/SiC Layered Interface. *J. Mater. Sci.* **1990**, *25*, 4856.
(18) Deqing, W.; Ziyuan, S. Aluminothermic Reduction of Silica for the Synthesis of Alumina-Aluminum-Silicon Composite. *J. Mater. Synth. Process.* **2001**, *9* (5), 241–246. https://doi.org/10.1023/A:1015295200586.
(19) Salje, E. Heat Capacities and Entropies of Andalusite and Sillimanite: The Influence of Fibrolitization on the Phase Diagram of the Al_2SiO_5 Polymorphs. *Am. Mineral.* **1986**, *71* (11–12), 1366–1371.
(20) Suslick, S.; Fang, M. Acoustic Cavitation and Its Chemical Consequences. *Phil. Trans. R. Soc. Lond.* **1999**, No. 1927, 335–353.
(21) Liu, M.; Ma, Y.; Wu, H.; Wang, R. Y. Metal Matrix-Metal Nanoparticle Composites with Tunable Melting Temperature and High Thermal Conductivity. Liu M, Ma Y, Wu H, Wang RY. *ACS Nano* **2015**, *9* (2), 1341–1351. https://doi.org/10.1021/nn505328j.
(22) Tran, N.; Zhao, W.; Carlson, F.; Davidson, J. H.; Stein, A. Metal Nanoparticle − Carbon Matrix Composites with Tunable Melting Temperature as Phase-Change Materials for Thermal Energy Storage. **2018**. https://doi.org/10.1021/acsanm.8b00290.
(23) Khan, Z.; Khan, Z.; Ghafoor, A. A Review of Performance Enhancement of PCM Based Latent Heat Storage System within the Context of Materials, Thermal Stability and Compatibility. *Energy Convers. Manag.* **2016**, *115*, 132–158. https://doi.org/10.1016/j.enconman.2016.02.045.
(24) Fu, Q.; Zhu, J.; Xue, Y.; Cui, Z. Size- and Shape-Dependent Melting Enthalpy and Entropy of Nanoparticles. *J. Mater. Sci.* **2017**, *52* (4), 1911–1918. https://doi.org/10.1007/s10853-016-0480-9.
(25) N. Birks, G. H. Meier and F. S. Pettit. Introduction to the High Temperature Oxidation of Metals. *Cambridge Univ. Press* **2006**, *003*, 17.
(26) Caroli, V. G. M. and S. *Tables of Standard Electrode*; 1978; Vol. 2.

General conclusions and perspectives

The electrical vehicle is expanding due to the gradual awareness and national policies of reducing fuel consumption and emissions of pollutants. But until now, there are still challenges that must be addressed to improve its performances and enable wide spread application. Long endurance as one important concern that requires the decrease of the vehicle's weight. Electrification of the whole vehicle also encounters several challenges, particularly with regard to heat regulation. Improving the thermal management of batteries is a particularly important issue to ensure safety on board, to optimize cell aging and to preserve its performances. It is on these topics that the work in this thesis focused: fabrication of a metal matrix nanocomposites HfB_2-Al with enhanced mechanical properties, and fabrication of a metal matrix nanocomposite with phase-transition inclusions made of phase change Bi cores encapsulated in silica, as a proof of concept for thermal regulation. The fabrication process applied in this work is liquid metallurgy assisted by ultrasound treatment that could be scaled up and implemented in current work flows for the production of aluminum alloys.

We have addressed the incorporation of nanoparticles synthesized in molten salts into aluminum-based matrices by ultrasound-assisted liquid metallurgy. An experimental set-up was designed and the process was carefully engineered to achieve total incorporation of nanoparticles in the matrix with decreased porosity and homogeneous chemical composition over the whole volume at the micron scale.

Several experiments were then performed by dispersing in molten aluminum 0.8 vol.% of HfB_2 nanoparticles synthesized in molten salts. Commercial SiC nanocomposites were also assessed as references. According to electron microscopy, both types of nanoparticles are able to maintain their size and morphology after the high temperature melting process, but nanoparticles were segregated at the grain boundaries. HfB_2 particles were only located at the boundaries, but SiC nanoparticles were also observed inside the Al grains, indicating better dispersion. Liquid nitrogen quenching was then applied to refine the microstructure. Parameters regarding the improvement of wettability (composition of the matrix, type of the nanoparticles, coating of the nanoparticles) or the quenching step (in particular other protocols developed to manufacture amorphous alloys) might be explored to gain further control over the dispersibility.

The strengthening effect of the nanoparticles was studied with nanoindentation tests. The mapping of the mechanical properties correlated with the optical image, which showed

heterogeneous hardness at the micro scale: a population with a relatively homogeneous hardness corresponding to the matrix grains and a second population with significantly higher hardness for the intergranular zones, in line with the high concentration of nanoparticles of hard phases at grain boundaries. The same phenomenon is also observed in other nanocomposites such as SiC-Al, HfB_2-$AlSi_7Cu_{0.5}Mg_{0.3}$. The average hardness of the sample with the inclusion of HfB_2 nanoparticles was improved by 14%. This value is lower than that of SiC nanocomposite with the same volume ratio (21%), probably due to the difference in segregation state. The elastic modulus measured by nanoindentation showed no difference between pure Al and nanocomposites with 0.8 vol% loading of nanoparticles (SiC and HfB_2). The tensile strength might also be measured to reveal the differences of elastic modulus at the macroscale.

Three main pathways were explored to fabricate bismuth-aluminum composites by liquid metallurgy. Firstly, Bismuth oxide was dispersed in molten Al and further reduced *in situ* into metallic bismuth by aluminoreduction. This process was proven hard to be replicated for other inclusions with are more difficult to be reduced, such as In or metallic alloys. Secondly, bismuth nanoparticles were directly incorporated in the Al matrix. Nanoparticles underwent large extent Ostwald ripening during the dispersion in molten Al, forming two groups of particles with diameters below 10 nm and about several micrometers, respectively. Thirdly, we have developed an encapsulation method by designing core-shell $Bi@SiO_2$ nanoparticles, to incorporate in molten Al. The nano-inclusions also underwent size distribution widening towards smaller and larger sizes by Ostwald ripening, but to a smaller extent than the non-encapsulated sample since the maximal particle size of the enlarged particles was about only 200 nm. This result indicates that although the silica shell underwent chemical reaction and local mobilization, it acted efficiently against core coalescence. We have also demonstrated that the silica shell underwent aluminothermic reduction, which led to silicon and an aluminosilicate as intermediate. Thermal analysis indicated that around 90% of Bi element are still in nanoscale. The average phase-transition temperature is lower than the Bi-Al_2O_3 nanocomposite prepared by powder metallurgy described in the literature.[2] Based on these results, the next tracks to further explore is the major challenge of reaching phase change nanoparticles suitable for thermal management of Li-ion battery, with an operating temperature at 60-80 °C. This could be achieved by incorporating nanoparticles of low melting point alloys, such as Bi-In alloys. By this method, we could expect to widen the phase transition temperature range to achieve

progressive heat absorption with the increase of the battery's temperature. The next step would then be to select low-cost elements and materials that would render the approach viable for an industrial process.

These proofs of concept nonetheless appear to be very encouraging steps towards the development of new metal matrix nanocomposites. Thanks to its adaptability, the described process could be used for boride-based light-weight materials or for thermal management materials for electronic/electrical device through the choice of appropriate inclusions and metal matrix.

Appendix

S3.1 Design of the process for the preparation of nanocomposites

S3.1.1 Incorporation methods

The nanoparticles were first incorporated to the molten metal following the same procedure as described in the literature,[1] that is to say direct incorporation of the powders. Attempts have been made by using BN nanosheets,[31] SiC and HfB_2 nanoparticles, and Bi_2O_3 microparticles (several micrometres). Despite the removal of the native aluminum oxide layer at the surface of the metal matrix grains prior to melting, we were not able to incorporate all the nanoparticles inside the matrix by simple stirring methods (Appendix 3.1). For samples dispersed by 5 minutes ultrasound treatment, a loss of more than 90% of initial particles was detected by WDXRF analysis (Appendix 3.2). Such a low inclusion content compared to the initial ratio could be due to the precipitation of nanoparticles since brown powders were observed at the bottom of the crucible. The difficulties to incorporate the nanoparticles into the melt lie in the poor wettability and the high volume fraction between the nanoparticles powder and liquid aluminum.

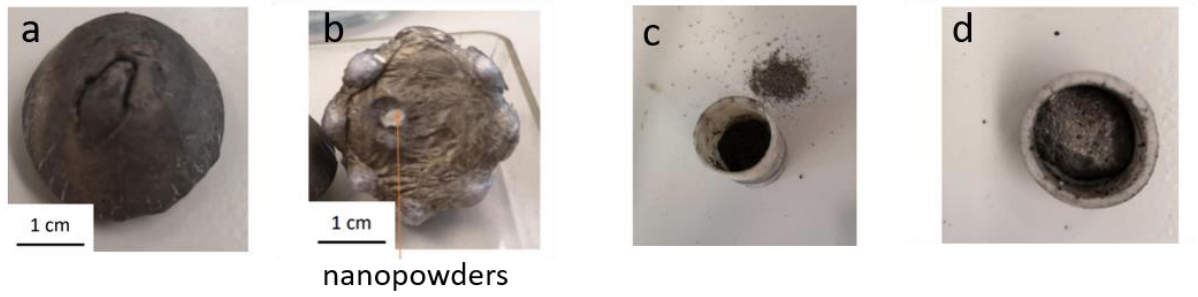

Appendix 3.1. (a) Al ingot after melting in an induction furnace, (b) Al ingot with BN nanoparticles after melting in induction furnace. (c) Direct incorporation of SiC nanopowders in pure molten aluminum with 5 min ultrasound treatment. Brown powders were found at the bottom of the crucible. (d) Direct incorporation of HfB_2 powders in pure molten aluminum with 5 min ultrasound treatment.

Nanoparticles	Matrix	UST	WDXRF approx. wt.%					
			Al	Ti	Bi	Hf	Si	B
	$AlSi_7Cu_{0.5}Mg_{0.3}$	No	92	/	/	/	7	/
2 wt% BN	$AlSi_7Cu_{0.5}Mg_{0.3}$	No	92	/	/	/	7	Not detected
	Al	Ti tip, 5 mins	94	1.4	/	/		/
2 wt% HfB_2	Al	Ti tip, 5 mins	80	5.5	/	300 ppm	/	Detected
30 wt% Bi_2O_3	Al	Ti tip, 5 mins	91	1.5	3.3	/	/	/
2 wt% SiC	Al	Ti tip, 5 mins	78	0.9	/	/	0.6	/

Appendix 3.2. WDXRF analysis of samples with direct incorporation of nanoparticles in molten Al

A master nanocomposite method was proposed by the group of Li *via* sintering of nanoparticles and Al micropowder (50 wt % loading) together at 900 °C leading to a robust and compact pellet.[5] In our study, this method cannot be directly applied because of the cohesion of the nanoparticles and of the potential reactivity between Al micron scale grains and the particles' boron-rich shell before dispersion. An alternative two-step processing method was then developed. Nanoparticles were dispersed in absolute alcohol in the presence of the aluminum powder. This suspension was dried in an ultrasound bath to ensure its homogeneous deposition over aluminum powder. The mixture was pressed into a pellet, then diluted in an aluminum melt for ultrasound dispersion. This additional step of compaction of the nanopowder with aluminum enhanced the overall incorporation. The macroscale homogeneity of the as-synthesized nanocomposites was evaluated by WDXRF. For a HfB_2-Al nanocomposite, the

chemical composition of 3 cut pieces was identical, and the inclusion ratio (Hf/Al) was close to the expected value (Appendix 3.3a,b). The slight difference between expected and measured values could be explained by the presence of Ti impurity.

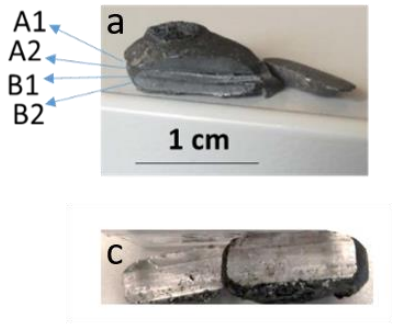

b

Piece code	Hf/Al at. ratio
Expected	0.025
Original	0.02
A1	0.02
B2	0.02
Bottom	0.02

Appendix 3.3. Two-step synthesis for a 0.8 vol.% HfB_2-Al nanocomposites: (a) Photograph of the sample, (b) WDXRF analysis on different cross sections. (c) Photograph of 0.8 vol.% HfB2/Al nanocomposites.

The maximum load of inclusions prepared by this method was evaluated by increasing the nanoparticle ratio in the pellet. The sedimentation of particles at the bottom part of the matrix was observed in the case of HfB_2-Al nanocomposites with nanoparticle content over 2 vol.% (Appendix 3.3c). Furthermore, when the loading of inclusion was over 5 vol.%, either for SiC or for HfB_2, it was impossible to press nanoparticles/Al powder mixtures into a cohesive pellet under our experimental conditions (8 tons for 2 minutes). A loose and fragile pellet was obtained. Therefore, we chose to study nanocomposites with volume fraction < 2.4 vol.%. It could also be noticed that at this concentration, it is impossible to detect nanoparticles by XRD.

S3.1.2 Improvement of the ultrasonic treatment setup

High intensity ultrasonic waves generate cavitation and acoustic streaming, which is most likely to refine the microstructure, break aggregates and homogenize the distribution of nanoparticles. However, as mentioned in chapter 1, this method requires a good control of processing condition such as ultrasonic power, ultrasonic treatment time, erosion state of the tip and the

depth of dipping of the tip in liquid metal. Here we designed an experimental set-up adapted to small volume of aluminum melt around 2 mL to optimize these conditions.

Concerning the choice of the tip, most of the commercial microtips are made of titanium alloy. In our study, titanium tip brought around 1 wt. % of Ti after 10 minutes of ultrasound treatment in pure aluminum. Besides, titanium is a strong boride former that could react with the boron shell of HfB_2 nanoparticles, leading to an increased ratio of Ti in WDXRF analysis. Komarov *et al.* studied the erosion resistance of Nb tip and demonstrated a good stability over 10 hours of ultrasound treatment.[32] Thus, a niobium tip with 4 mm of diameter has been designed on purpose by the supplier to replace the classic titanium alloy tip. EDS analysis of samples treated with Nb tip showed no presence of Nb pollution (Appendix 3.4).

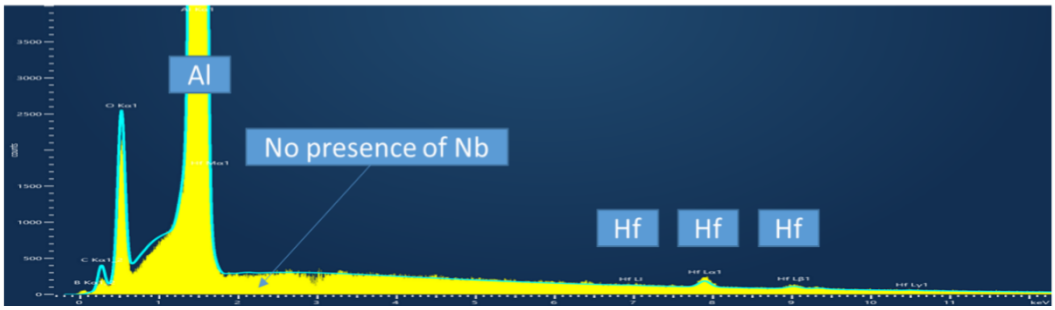

Appendix 3.4 EDS analysis of HfB_2-Al nanocomposites treated by Nb ultrasonic probe for 5 minutes

The form of the crucible was specially designed as well to increase the dipping depth of the ultrasonic tip (3 mm). Compared to the extremely large batches (*ca.* 1 L) described in previous studies, this set-up is suitable for preliminary studies without needs to scale up the synthesis of nanoparticles.

Previous works have proven that mechanical properties of nanocomposites obtained by discontinuous ultrasonic treatments were better improved than with continuous ultrasonic treatments for 20 min period.[16] An interval of 5s on/ 5s off was then applied for all experiments. This interval time could also prevent overheating of the ultrasound generator. Furthermore, it was necessary to assess the influence of the ultrasound treatment power. A power varying from 10 to 40% of the nominal power was applied during the preparation of HfB_2-Al samples. Strong ultrasonic power over 40% resulted in the splash of liquid on the upper crucible wall leading to

a loss of around 42% of the sample. Intermediate ultrasonic power caused less liquid splash, but pores with size varying from 0.05 to 1 mm were formed at the top part of the sample. The formation of these bubbles could be explained by confinement of the cavitation bubbles during solidification process. According to these observations, the best compromise was to use an ultrasound power of 30% for ultrasonic dispersion, followed by 30 s degassing with a power of 10%. These conditions could act as a model to study the interactions between nanoparticles and matrix environment.

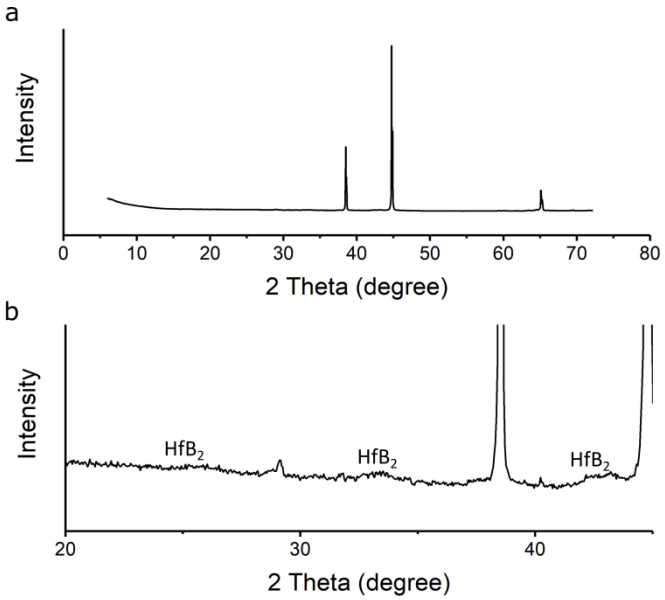

Appendix 3.5. XRD patterns of a 0.8 vol.% HfB_2-Al nanocomposite prepared with ultrasound treatment through a Nb tip for 30 minutes, and a zoom between 21° and 46°. The peak at 29° and 41° could be attributed to AlB_{12}.

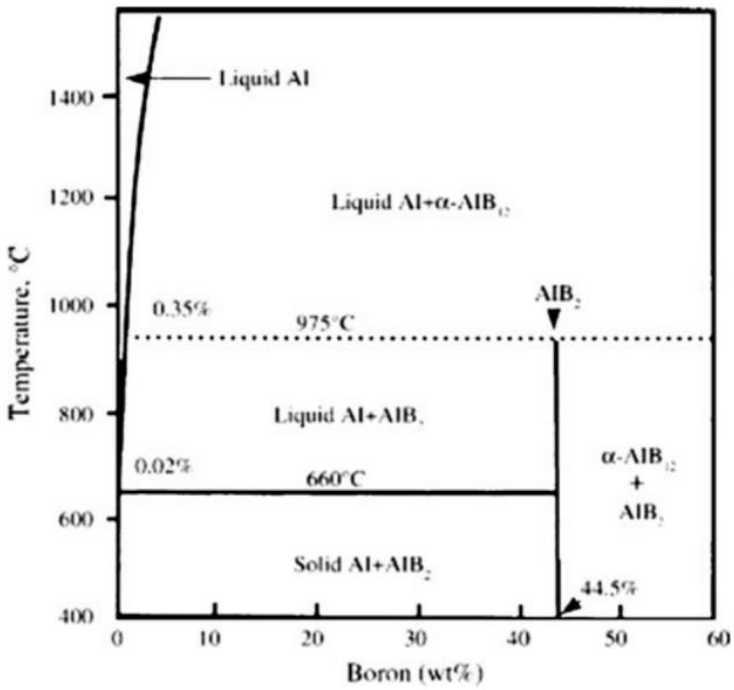

Appendix 3.6 Al-B Phase diagram [19]

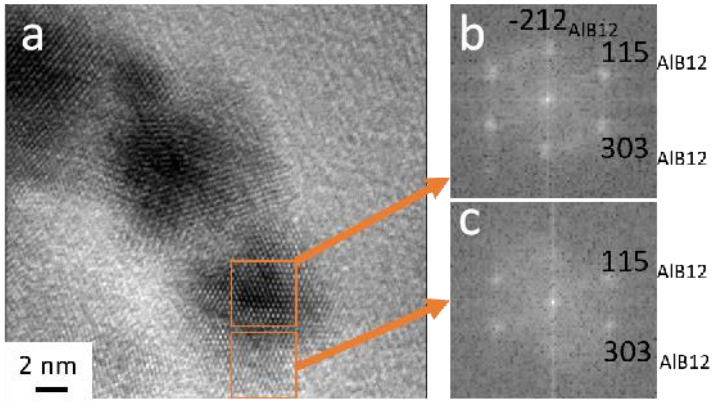

Appendix 3.7. HRTEM image and corresponding Fast Fourier Transforms (FFTs) indexed along the AlB_{12} structure for a 0.8 vol.% HfB_2/Al nanocomposite prepared with ultrasound treatment through a Nb tip for 30 minutes.

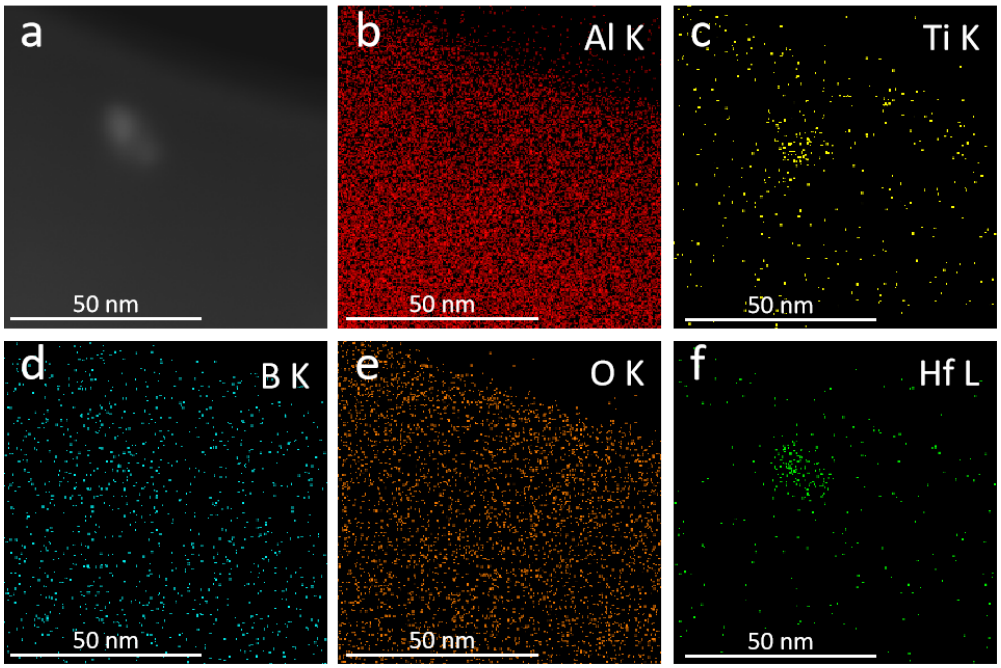

Appendix 3.8. STEM-EDS mapping of a 0.8 vol% HfB_2/Al nanocomposite prepared with ultrasound treatment by a Ti tip for 5 minutes and cooled down in liquid nitrogen.

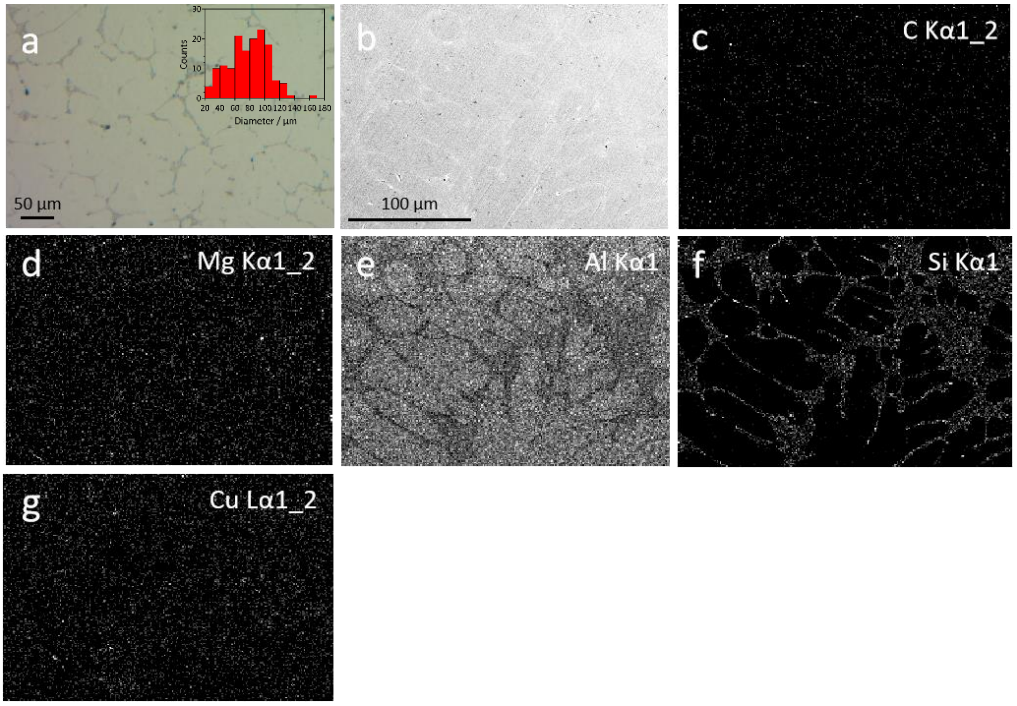

Appendix 3.9. SEM-EDS mapping and optical microcopy images for Al:$AlSi_7Mg_{0.3}Cu_{0.5}$ 1:1 treated at 600°C for 5 minutes

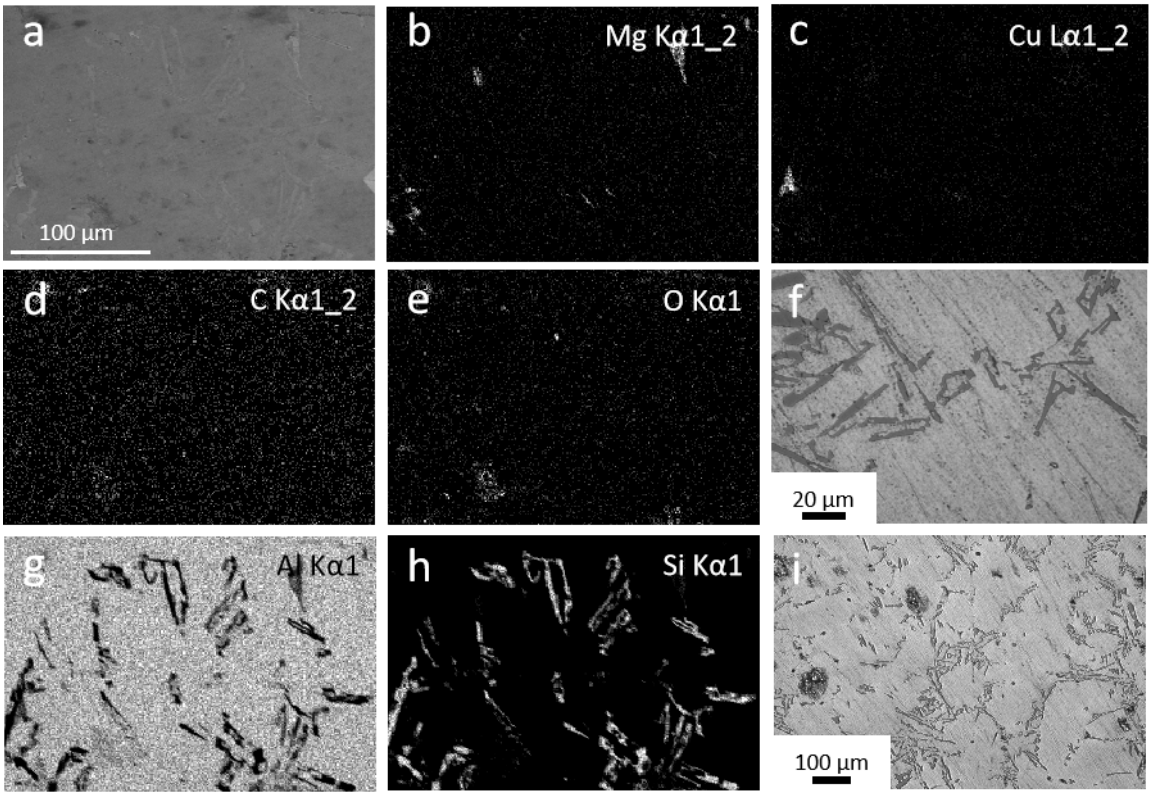

Appendix 3.10. (a-e,g,h) SEM-EDS mapping and (f,i) optical microscopy images for pristine $AlSi_7Mg_{0.3}Cu_{0.5}$

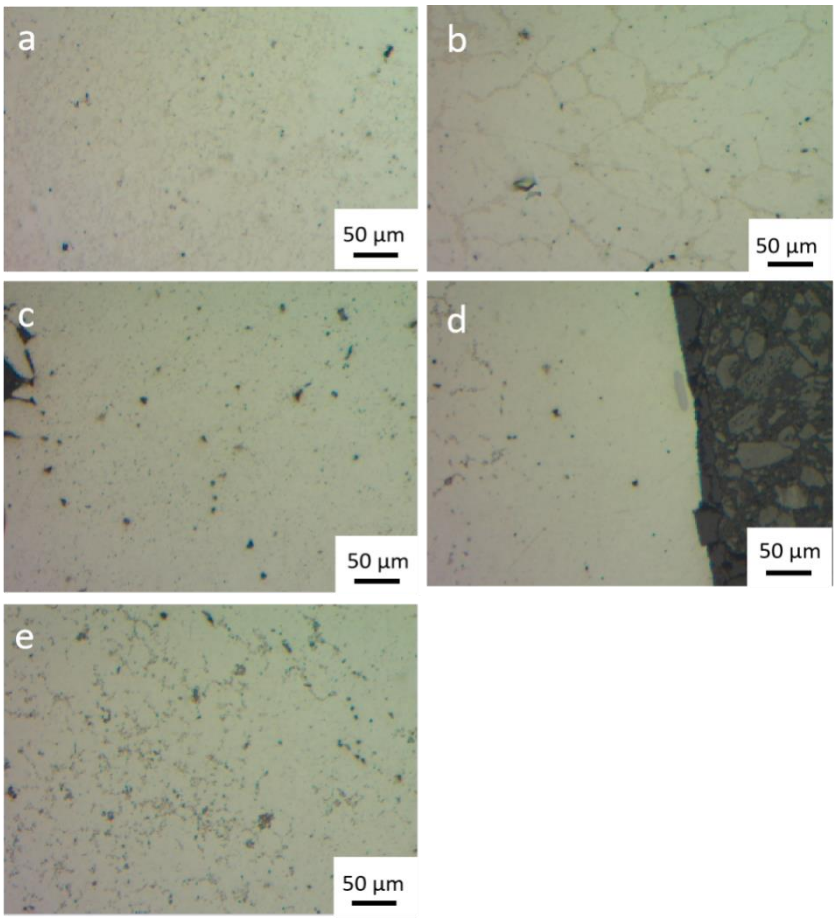

Appendix 3.11. Optical microscopy images of a 0.8 vol% HfB_2-Al nanocomposite prepared with ultrasound treatment through a Nb tip for 5 minutes and cooled down in liquid nitrogen. The observations were made on a vertical cross section. (a) Center of the section, (b) bottom of the section. Images of a 0.8 vol% SiC-Al nanocomposite prepared with ultrasound treatment through Nb tip for 5 minutes and cooled down in the liquid nitrogen. (c) Near the surface, (d) bottom near the crucible and (e) center part

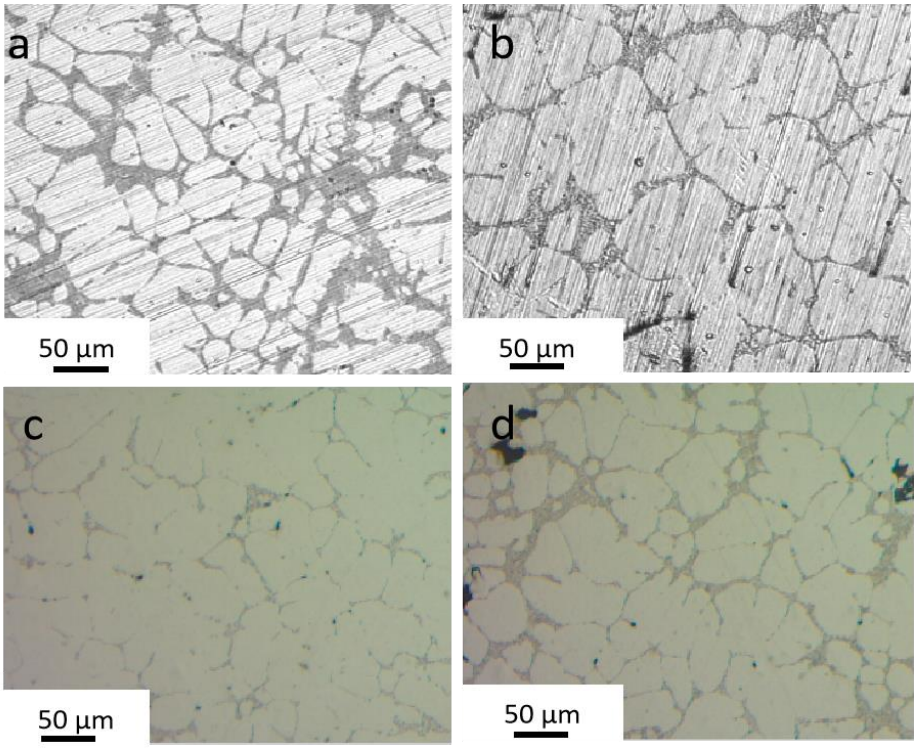

Appendix 3.12. Optical microcopy images of (a) a Al/AlSi$_7$Mg$_{0.3}$Cu$_{0.5}$ mixture prepared with ultrasound treatment through a Nb tip for 5 minutes and cooled down in the water; (b) a Al/AlSi$_7$Mg$_{0.3}$Cu$_{0.5}$ nanocomposite prepared with ultrasound treatment through a Nb tip for 5 minutes and cooled down in liquid nitrogen, (c) a 0.8 vol% HfB$_2$-AlSi$_7$Mg$_{0.3}$Cu$_{0.5}$ nanocomposite prepared with ultrasound treatment through a Nb tip for 5 minutes and cooled down in water; (d) a 0.8 vol% HfB$_2$-AlSi$_7$Mg$_{0.3}$Cu$_{0.5}$ nanocomposite prepared with ultrasound treatment through a Nb tip for 5 minutes and cooled down in the liquid nitrogen.

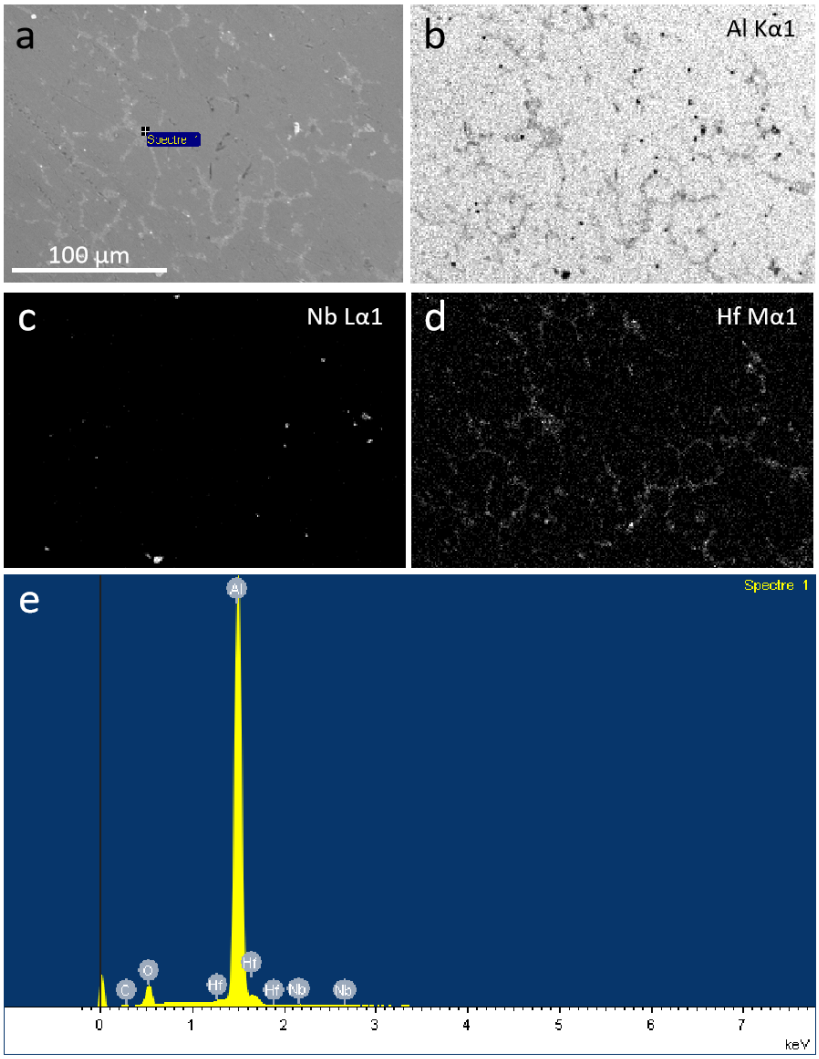

Appendix 3.13. SEM observations and EDS mapping of 0.8 vol.% HfB_2/Al nanocomposite prepared with ultrasound treatment through a Nb tip for 30 minutes and cooled down in liquid nitrogen

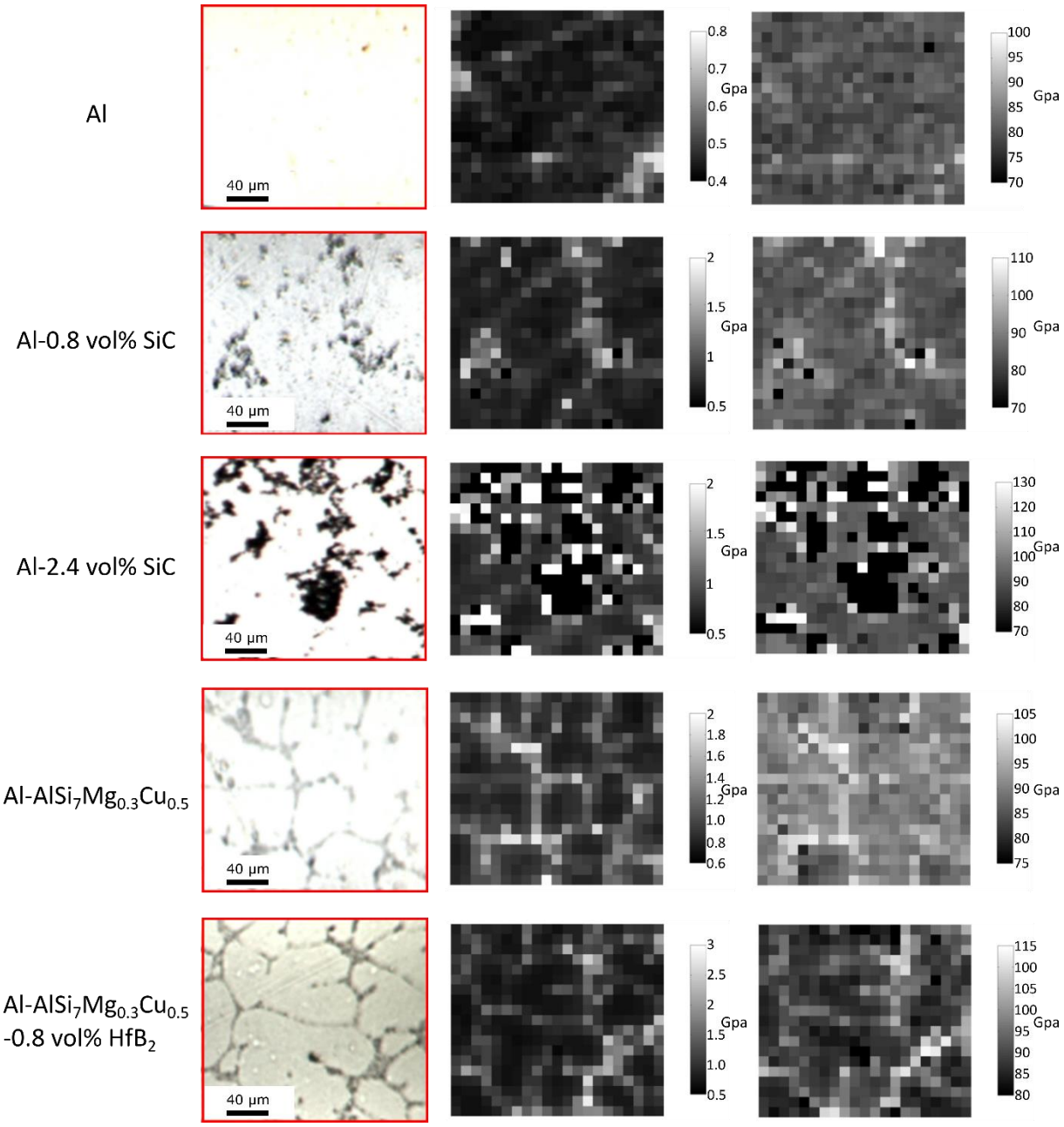

Figure S7. *Optical images (left) and nanoindentation mapping of (middle) hardness and (right) elastic modulus of Al (reference), 0.8 vol% SiC-Al, 2.4 vol% SiC-Al, Al-AlSi$_7$Mg$_{0.3}$Cu$_{0.5}$, 0.8 vol% HfB$_2$-Al-AlSi$_7$Mg$_{0.3}$Cu$_{0.5}$.*

Appendix 4.1. Image of Bi@SiO_2-Al sample

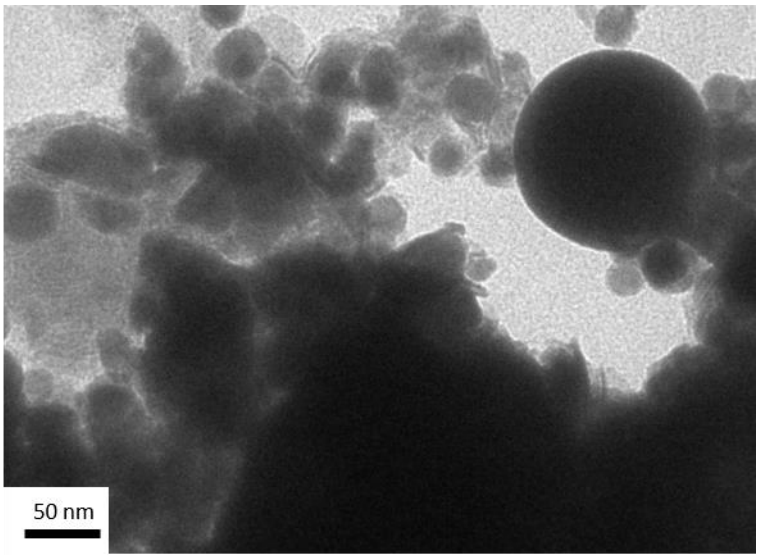

Appendix 4.2. TEM of bare Bi nanoparticles heated to 320°C after DSC experiments

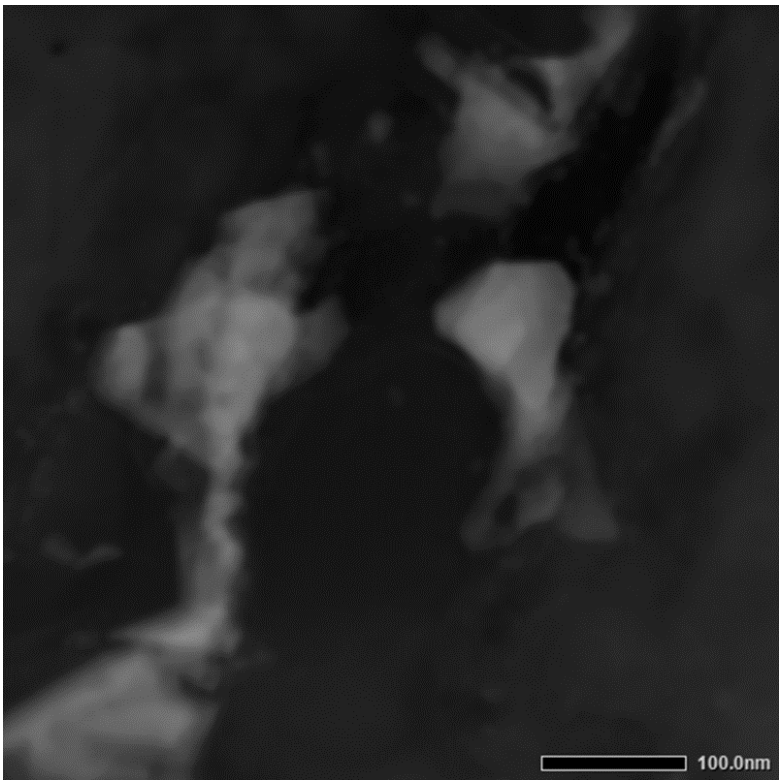

Appendix 4.3. TEM-HAADF image of Bi@SiO_2-Al nanocomposite

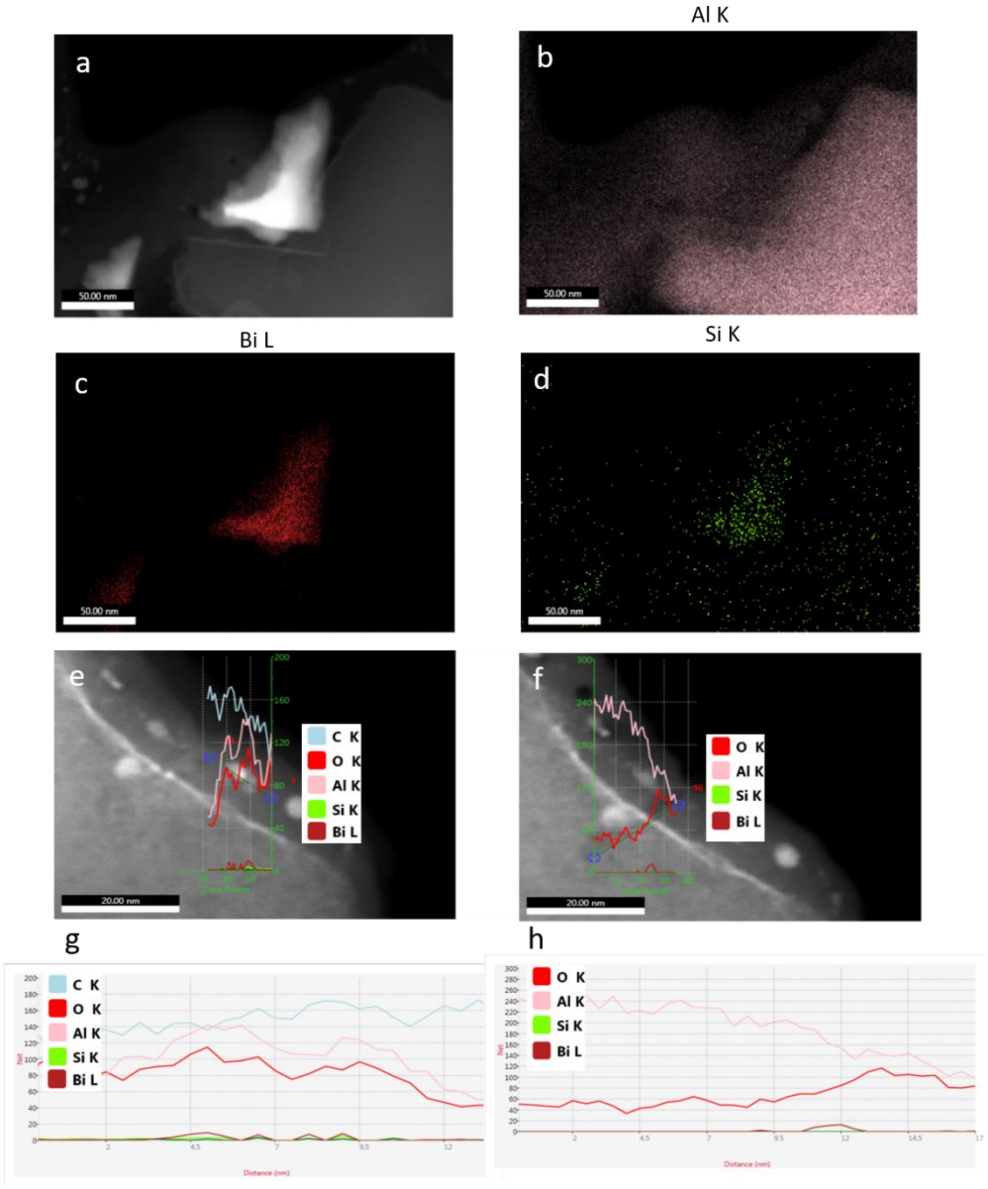

Appendix 4.4. a-d. STEM-EDS mapping and e-h. EDS line profile analysis of a thin slice in a Bi@SiO_2-Al sample.

Appendix S4.1 Fabrication of metal matrix nanocomposites by aluminum reduction of Bi_2O_3 *via* casting method

Fabricating composites by reducing high melting point oxides of a low melting point metal *via* liquid metallurgy particles has been proposed as a way to fabricate metal matrix phase change materials by solid metallurgy.[7] We have attempted a similar process by liquid metallurgy assisted by induction heating and ultrasonication. As in the work of Abraham et al.,[7] the dispersion of commercial 2.4 at. % Bi_2O_3 particles about 1 to 5 micrometres has been firstly carried out with similar process as described in above in section 4.2 for Bi@SiO_2/Al nanocomposites.

XRD patterns (Appendix 4.6) displaying metallic Bi and Al phase confirmed the success of aluminothermic reduction. An unidentified phase was also detected and could not be attributed to alumina. This is assigned to contamination from the ultrasonic tip. STEM-EDS mapping (Appendix 4.6) showed that the reduced Bi_2O_3 particles were located at the aluminum grain boundaries. STEM-EDS maps of a single nanoparticle (Appendix 4.5 c-f) presented an oxygen layer around 0.2 µm surrounding the Bi core, consistent with the formation of alumina during the reduction process.

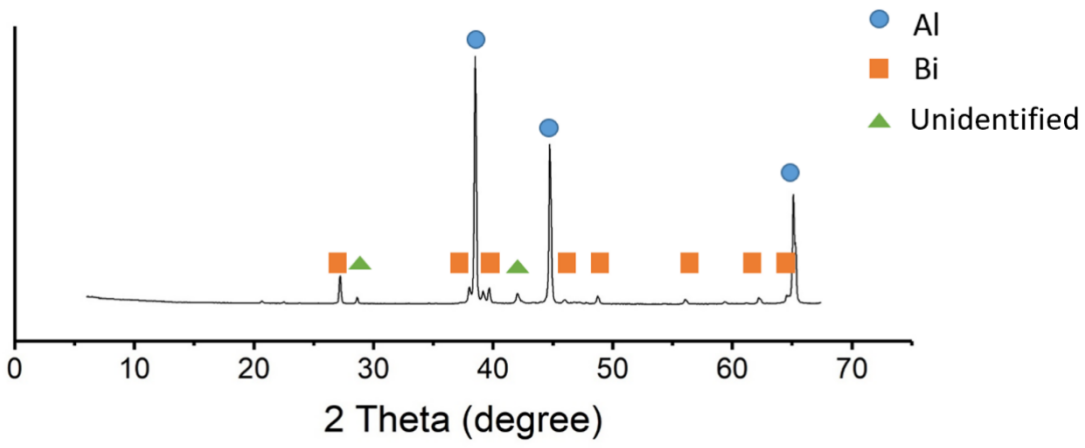

Appendix 4.6. XRD patterns of Bi_2O_3 /Al nanocomposite

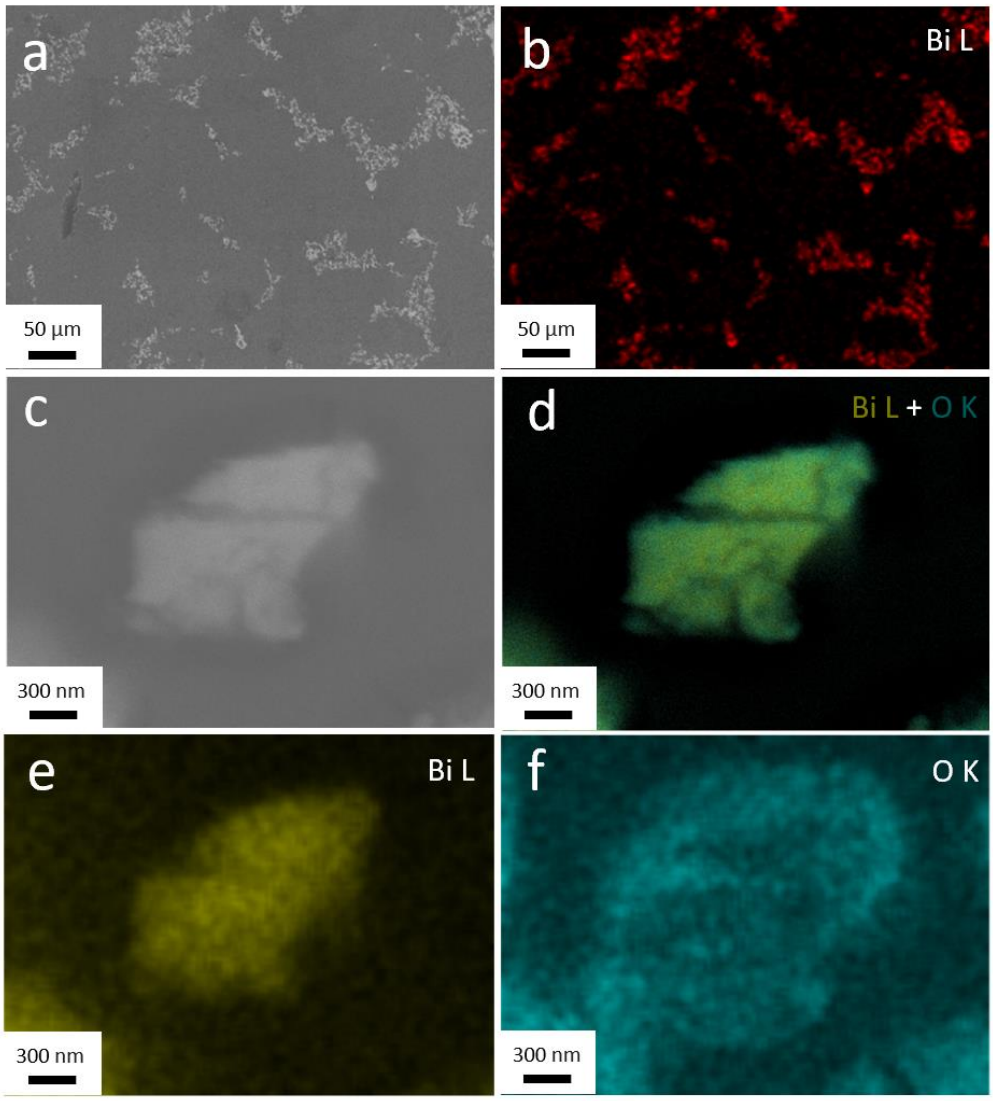

Appendix 4.7 SEM images (a, c) and SEM-EDS (b, d-f) maps of a Bi_2O_3-Al nanocomposite

DSC analysis was also performed for this sample in the same conditions as those described previously in 4.3.3.(figure Appendix 4.8) The intense peak centred at 271 °C during the heating ramp was in accordance with the melting process of bulk Bi.

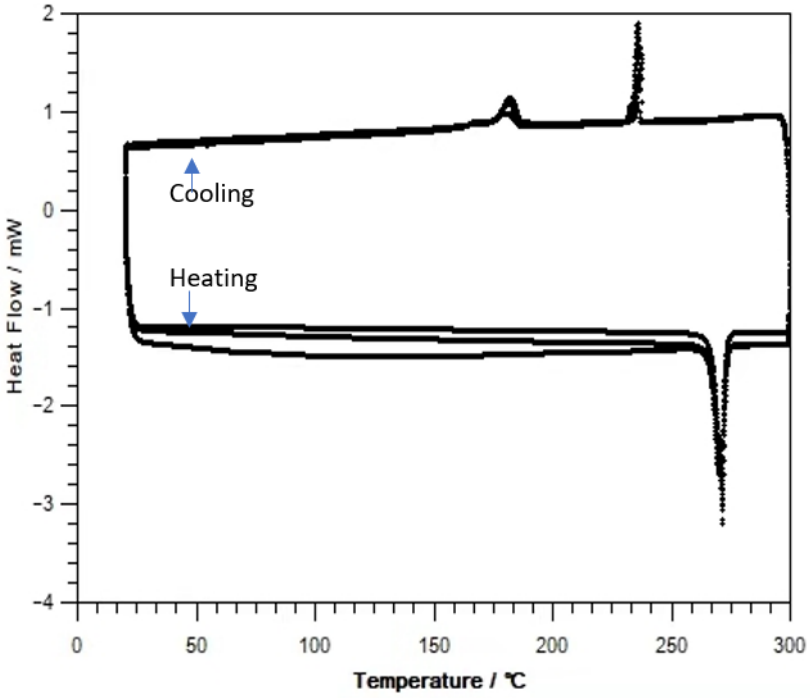

Appendix 4.8 DSC analysis of a Bi_2O_3-Al nanocomposite.

Appendix S4.2 Fabrication of metal matrix nanocomposites by aluminothermal reduction of In_2O_3 *via* casting method

In the objective of varying the melting temperature of inclusion particles, we have attempted to incorporate indium inclusions into an aluminium matrix, by dispersing commercial indium oxide nanoparticles (Sigma-Aldrich, around 75 nm) in molten aluminum. Examination of Ellingham diagrams[25] (Gibbs free energy vs temperature) indicates that the Gibbs free energy for the formation of In_2O_3 is less negative than that of Al/Al_2O_3, so In_2O_3 is expected to be reduced by Al.

According to XRD patterns (Appendix 4.11), indium was mostly in its oxidized state and the peak of metallic In presented a very low intensity. Indium oxide was not totally reduced by Al for the reaction with 10 minutes dwell time at 740 °C. This lower reduction kinetic compared

with Bi_2O_3 could be explained by the lower difference of Gibbs free energy between In_2O_3 and Al, as predicted in Ellingham diagram (Appendix 4.10).[26] On the heating DSC curve (Appendix 4.12), reduced metallic In is accounted for the broad peak centred at 157 °C, with an onset temperature at 146 °C. The melting temperature of bulk In is 156.5°C. The asymmetric peak shape could be assigned to the nano-size In inclusion showing lower melting temperature compared with bulk In.

These experiments proved the feasibility of *in situ* fabrication of $Bi/Al_2O_3/Al$ by a casting method. However, the formation of encapsulated inclusions by aluminoreduction is difficult to be applied to other types of inclusions: the reaction condition needs to be adjusted with the redox potential of the metal oxide and it is difficult to achieve other transition temperature. However, our concept of direct incorporation of inclusion metal@SiO_2 nanoparticles in molten Al presents a promising pathway to widen the nature of inclusions.

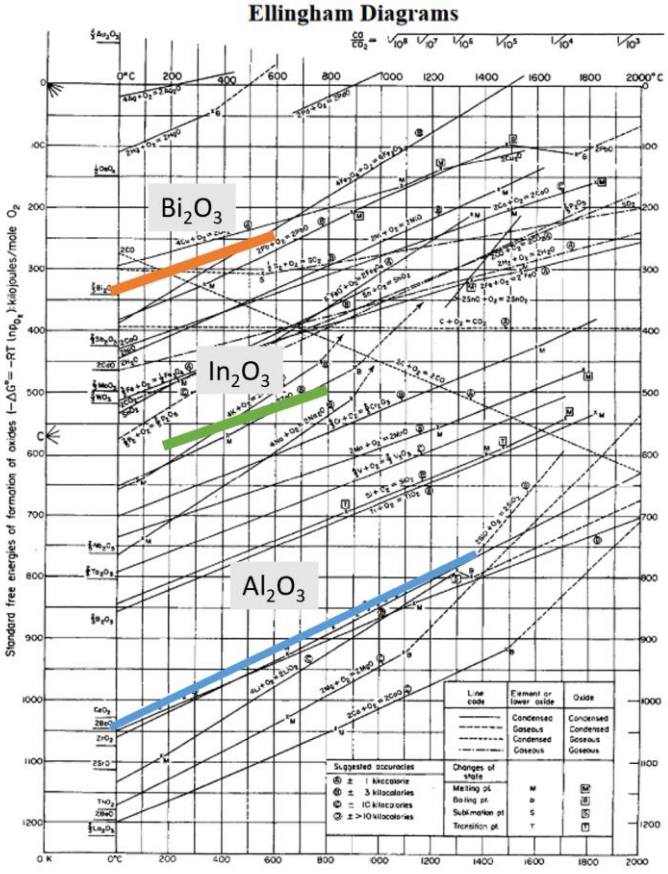

Appendix 4.10. Ellingham diagram[25]

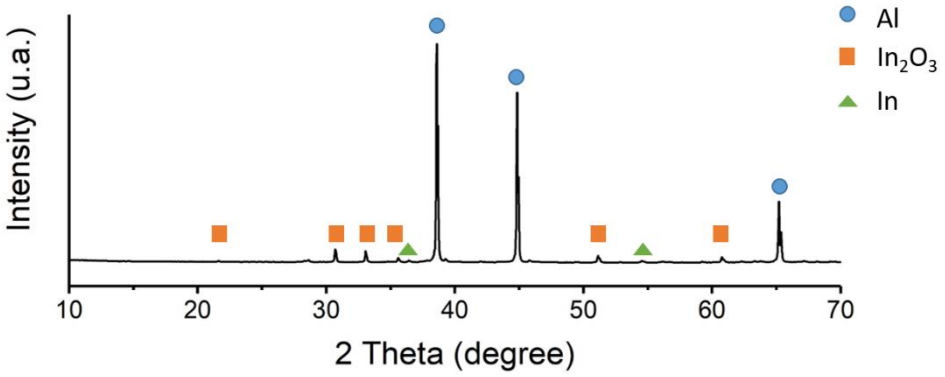

Appendix 4.11 XRD pattern of a In_2O_3-Al nanocomposite.

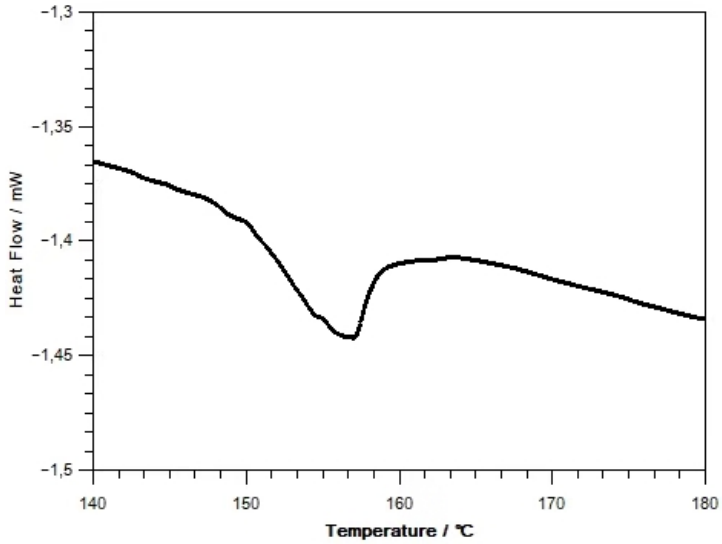

Appendix 4.12 DSC analysis of a In_2O_3-Al nanocomposite.

Résumé en Français

Introduction

Face aux défis énergétiques et environnementaux, le Groupe PSA investit depuis plusieurs années dans la fabrication de véhicules plus respectueux de l'environnement. Pour mener à bien cette stratégie, le groupe souhaite inventer et fabriquer de nouveaux matériaux légers, peu coûteux, à haute ductilité et possédant également de bonnes propriétés thermiques. Dans ce contexte, ce travail de thèse vise à étudier les nanocomposites à matrices métalliques (*metallic matrix nanocomposites* MMnCs) avec des propriétés mécaniques et thermiques améliorées. En particulier, les procédés de fabrication doivent être conçus pour répondre aux besoins du processus actuel de coulée de l'alliage.

Parmi les techniques de fabrication des nanocomposites métalliques, la métallurgie liquide assistée par ultrasons peut répondre à ces exigences. [1,2] L'utilisation du traitement par ultrasons est un bon moyen pour améliorer la dispersion des nanoparticules pendant le processus de moulage de l'alliage d'aluminium. Ce procédé offre également des avantages tels qu'un faible coût, un processus de moulage facile et une adaptabilité à la fabrication à grande échelle. [1]

L'examen de la littérature sur les MMnC actuels ouvre de nombreuses possibilités pour le développement de nouveaux matériaux. En ce qui concerne les propriétés mécaniques des MMnCs, les nanoparticules inorganiques commerciales se sont avérées utiles pour améliorer efficacement la résistance et le module d'Young de la matrice métallique.[3] Les nanoparticules de renforcement doivent être conçues pour satisfaire les mécanismes de renforcement et les conditions de la métallurgie à haute température. Les nanoparticules de borure synthétisées par des sels fondus sont de bons candidats car elles sont de petite taille, légères, dures et stables à haute température.[4] À notre connaissance, ce type de nanomatériaux n'a jamais été incoroporé au sein de nanocomposites. Une bonne dispersion des nanoparticules, essentielle pour les propriétés mécaniques finales peut être obtenue par le contrôle des paramètres de composition (mouillabilité de la matrice, nature des composés) ou par la modification des paramètres de mise en œuvre (procédé de chauffage, puissance du traitement par ultrasons, vitesse de chauffage/refroidissement). Cette partie du travail sera explorée en partie 1.

Les matériaux à changement de phase ont une application limitée dans le contrôle thermique de la température des batteries des véhicules en raison de leur faible conductivité thermique et de leur faible résistance aux vibrations.[5] L'incorporation de matériaux à changement de phase dans une matrice métallique suscite un grand intérêt dans l'industrie automobile en raison de la haute conductivité thermique, de leurs propriétés mécaniques élevées et de la large gamme de températures de fonctionnement des matrices métalliques.[6] Dans ce cas, le matériau à changement de phase est en général un métal à bas point de fusion. Les stratégies conventionnelles, notamment la métallurgie des poudres, nécessitent des coûts de fabrication élevés pour ce type de composites.[7] De plus, la température de travail est également limitée : le changement de phase ne se produit qu'à la température de fusion du métal pur. Pour surmonter ces problèmes, une méthode en phase liquide est proposée : les nanoparticules métalliques (Bi) seront encapsulées dans une enveloppe de SiO_2 pour empêcher l'immersion dans la matrice. Ensuite, ces nanoparticules seront incorporées dans la matrice métallique fondue par un procédé assisté par ultrasons. Cette partie du travail sera présentée dans la partie 2.

Partie 1. Nanocomposites à matrice métallique HfB_2-Al et ses propriétés mécaniques

Un montage combinant un four à induction et un ultrasonicateur opérant à haute température a été développé pour la préparation des nanocomposites par métallurgie liquide. Plusieurs paramètres tels que le protocole d'incorporation des nanoparticules, la nature du creuset, la forme du creuset, la puissance des ultrasons, l'intervalle du traitement ultrasons et la rampe du chauffage ont été étudiés afin d'identifier les meilleures conditions pour la synthèse des nanocomposites :

- L'incorporation des particules est réalisée en deux étapes afin d'assurer un transfer quantitatif des particules dans la matrice métallique : 1) mélanger les nanoparticules et l'aluminium à l'état de poudres puis presser ce pré-mélange en pastille, 2) diluer la pastille dans l'Al fondu.
- Un creuset en alumine a été spécialement conçu pour augmenter la hauteur du métal fondu et la résistance au choc thermique.
- Une canne à ultrasons en niobium a été conçue par le fournisseur afin d'éviter la pollution des matériaux finaux par la sonotrode usuelle (alliage de titane).
- Un intervalle on/off du traitement d'ultrason a été appliqué afin d'améliorer la dispersion et de refroidir la sonotrode.

- La puissance d'ultrasons est maintenue à 30% de la puissance maximale de l'appareil pendant le traitement, puis le milieu est traité à 10% afin d'éviter la formation de bulles avant la solidification. En effet, une haute puissance d'ultrasons (> 40% de la puissance maximale) proboque des projections de métal fondu à l'extérieur de la zone de chauffage. Néanmoins, la puissance d'ultrasons à 30% conduit aussi à de la porosité dans le matériau final, induite par la cavitation provoquée par le traitement ultrasons.

Les nanoparticules de HfB_2 ont été d'abord synthétisée en sels fondus.[8] Les clichés de microscopie électronique en transmission (TEM, Figure 1a) montrent que la morphologie est de type cœur-coquille, avec un cœur de HfB_2 de diamètre variant entre 4 et 14 nm, et une couche de bore amorphe d'environ 3 nm qui recouvre les nanoparticules de HfB_2. Les diagrammes de rayon X confirment la phase de HfB_2.

Plusieurs expériences ont ensuite été réalisées en dispersant 0,8 vol.% de nanoparticules de HfB_2 dans de l'Al en utilisant les meilleures conditions définies précédemment. Des nanocomposites Al/SiC ont aussi été réalisés comme références.

Les images TEM (Figure 1d) pour l'échantillon 0,8 vol.% HfB_2-Al (traitement aux ultrasons par une pointe en niobium pendant 5 minutes, suivi d'une trempe dans l'azote liquide) montrent que les nanoparticules forment des agrégats submicroniques entre les grains d'aluminium. Les nanoparticules de HfB_2 ont pu conserver leur taille après le processus de fusion à haute température. Néanmoins, leur morphologie a légèrement changé, passant de particules rondes à des particules facettés (figure 1c). La phase HfB_2 a été confirmée par HRTEM, indiquant également la stabilité thermique des nanoparticules HfB_2.

Ces échantillons ont ensuite été analysés par microscopie électronique en balayage (SEM) couplée à l'EDS. L'agglomération des particules de HfB_2 a été observée le long des joints de grain de l'aluminium plutôt qu'une distribution uniforme dans la matrice. Les mesures d'analyse EDS donnent une composition hétérogène aux joints de grains : les nanoparticules de HfB_2 ont ségrégé vers ces zones. Les nanocomposites à base de nanoparticules commerciales de carbure de silicium dispersées dans l'aluminium suivent la même tendance.

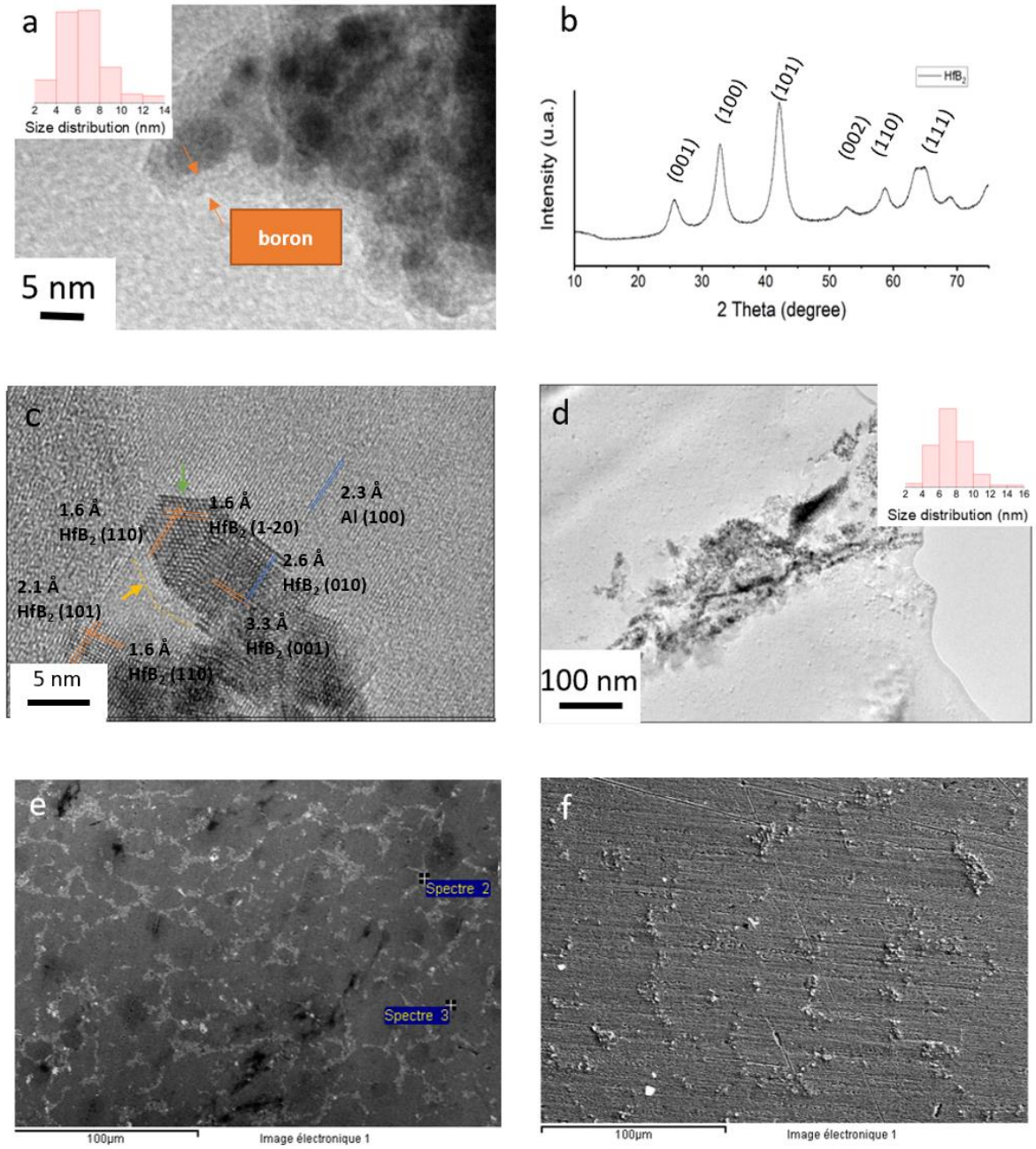

Figure 1. a) Clichés TEM des nanoparticules de HfB_2 avant incorporation. b) Diagramme de DRX de la poudre constituée de nanoparticules HfB_2. c-d) Clichés TEM du nanocomposite 0,5% HfB_2-Al. e) Clichés de SEM du nanocomposite 0,5% HfB_2-Al. e) Clichés SEM du nanocomposite 0,5% SiC-Al.

L'analyse de la taille moyenne des grains d'aluminium révèle un raffinement de la microstructure, avec des grains de plus petite taille que les grains initiaux avant chauffage. Des échantillons de HfB_2/Al à 0,5 vol.% ont été refroidis à différentes vitesses de refroidissement. La taille moyenne des grains est de 120 µm, 78 µm et 20 µm respectivement pour les taux de

refroidissement de 6, 18 et 100°C min^{-1}. Le refroidissement par azote liquide permet un refroidissement d'environ 100°C min^{-1} s'avère donc être la meilleure pour affiner la microstructure des MMnCs.

L'effet de renforcement des nanoparticules ont été étudié avec des tests en nanoindentation. La dureté moyenne de l'échantillon avec l'inclusion des nanoparticules HfB_2 est de 0,53 GPa, plus élevé que la référence de l'aluminium pur préparée dans les mêmes conditions à 0,42 GPa. Plus de 50% des mesures montrent une dureté plus élevée que l'aluminium pure, correspondant la zone renforcée entre les joints de grains. La moyenne de cette population est de 0,66 GPa, nettement supérieur à l'aluminium pur. Ces mesures confirment l'effet renfort des nanoparticules HfB_2.

La cartographie des propriétés mécaniques corrélée avec l'image optique permet de mieux visualiser la différence entre l'intérieur des grains et les joint de grains (figure 2). On observe une dureté hétérogène : une population avec une dureté relativement homogène correspondant aux grains et une deuxième population sensiblement plus élevée pour les zones intergranulaires. Ce phénomène est aussi observé dans d'autres nanocomposites tel que SiC-Al, HfB_2-$AlSi_7Cu_{0.5}Mg_{0.3}$.

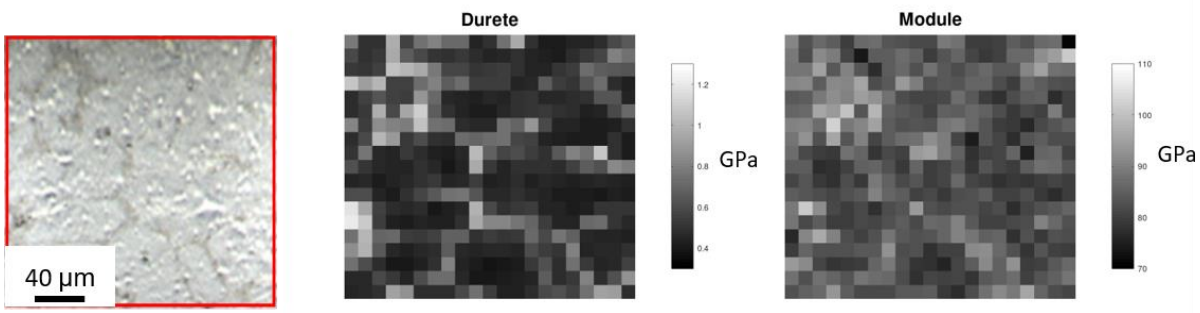

Figure 2. Cliché de microscopie optique (gauche) correlé à la cartographie des propriétés mécaniques (dureté, module d'élasticité) du nanocomposite 0,5% HfB_2-Al.

Pour conclure cette partie 1, nous avons testé l'incorporation des nanoparticules synthétisé en sels fondus dans la matrice de l'Al par la métallurgie liquide assistée par ultrasons.

Les nanoparticules sont stables après le chauffage et agrégées au niveau du joint de grain. Ceci permet de raffiner la microstructure et d'augmenter les propriétés mécaniques entre les joint-grains. Cependant, l'effet de renforcement est moins marqué avec HfB_2 comparé aux nanocomposites à base de nanoparticules SiC commercial. Dans la littérature[4], la dureté Vickers du SiC en vrac est de 25,5 GPa et celle du HfB_2 est de 30,5 GPa. Cette différence ne pourrait pas être expliquée par la dureté entre les nanomatériaux. En outre, les grains de matrice pour les nanocomposites contenant des nanoparticules de SiC sont plus durs que pour l'aluminium pur, alors les mêmes grains dans les nanocomposites à base de HfB_2 sont de même ordre de grandeur que la référence d'aluminium, ce qui indique que les grains contiennent aussi des particules de SiC, au contraire de HfB_2 qui ségrège totalement. Cette mauvaise dispersion est probablement due à l'état d'agrégation des nanoparticules de départ (après la synthèse en sels fondus) et à la mouillabilité de HfB_2 par l'aluminium, que l'on suppose faible. La trempe de l'échantillon dans l'azote liquide permet d'affiner la microstructure de limiter la croissance des grains d'aluminium. D'autres protocoles de trempe, développés notamment par P. Duwez pour fabriquer des alliages amorphes,[9] seraient envisageable pour obtenir un nanocomposite HfB_2-Al mieux dispersé.

Partie 2. Nanocomposites à matrice métallique Bi@SiO_2-Al avec des propriétés de la gestion thermique

La première étape de la préparation du composite consiste en la synthèse de nanoparticules de bismuth avec une taille contrôlée (Figure 3a). Celle-ci a été réalisée selon une procédure de chimie colloïdale précédemment rapportée par Scheele et al.[10] Des nanoparticules de bismuth d'environ 25 nm avec une distribution de taille relativement étroite ont été synthétisées.

Dans un deuxième temps, les nanoparticules de bismuth ont été recouvertes d'une coquille de silice de 7 nm d'épaisseur par la méthode de Stöber.[11] Les nanoparticules de Bi sont encapsulées dans les coquilles et forment des amas de plusieurs particules. Les agrégats ont une taille allant jusqu'à 160 nm (Figure 3b).

Des nanocomposites d'aluminium dans lesquels sont incorporées des nanoparticules de Bi@SiO_2 cœur-coquille (Bi@SiO_2-Al) et de Bi (Bi-Al) ont été obtenus par le procédé décrit

précédemment en partie 1. Les images SEM (Figure 3c) montrent que les zones riches en bismuth fortement contrastées ont une taille allant jusqu'à environ 100 nm. Les observations TEM (Figure 4d) met en évidence l'existence de nanoparticules de bismuth d'environ 10 nm (Figure 4.3d) et 60 nm. L'élargissement de la distribution de taille des particules après incorporation, vers les tailles plus petites et plus grosses peut être expliquée par le mécanisme de maturation d'Ostwald au cours du processus d'incorporation, qui vient de la dissolution partielle du bismuth dans l'aluminium fondu, comme attendu d'après le diagramme de phase Bi-Al.[12] Nous avons pu mettre en évidence la réduction *in situ* de la coque de silice par aluminoréduction, qui conduit à du silicium et à un aluminosilicate. Pendant le chauffage assisté par un traitement aux ultrasons, la coquille de silice est séparée du noyau de Bi, cela conduit à la lixiviation des gouttelettes de Bi qui ont subi une maturation d'Ostwald et ont évolué en deux populations de taille.

Le nanocomposite Bi-Al contient des particules de Bi de plusieurs micromètres. Ce résultat indique que bien que la coquille de silice ait subi une réaction chimique et une mobilisation locale, elle a agi efficacement contre la coalescence des cœurs par rapport à l'échantillon sans coquille de silice.

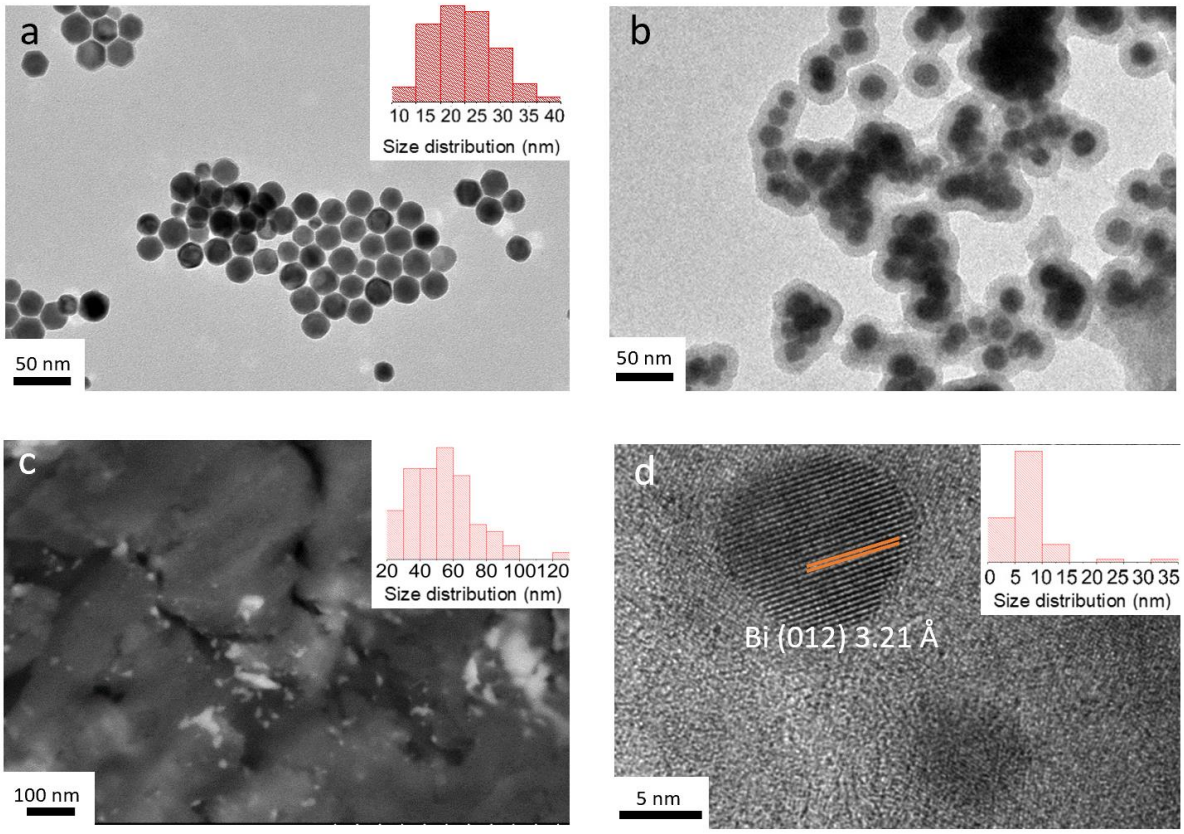

Figure 3. a) Cliché TEM des nanoparticules de Bi initiales. b) Cliché TEM des nanoparticules de Bi@SiO_2. c) Cliché SEM du nanocomposite 0,25% Bi@SiO_2-Al. d) Cliché TEM du nanocomposite 0,25% Bi@SiO_2-Al.

Les courbes d'analyse colarimétrique différentielle (DSC) des composites (Figure 4) présentent des pics endothermiques pendant le chauffage et un pic exothermique pendant le refroidissement. Le nanocomposite Bi@SiO_2-Al présente deux pics endothermiques avec une température de démarrage de la fusion à 251 °C : un pic large à 263 °C correspondant à la fusion des nanoparticules et un pic de faible intensité à 271 °C correspondant au bismuth massif. Le déplacement de ces pics vers des températures plus élevées par rapport aux nanoparticules de 30 nm confirme que certaines des nanoparticules ont coalescé pendant le processus de fusion. Le rapport d'enthalpie pour les pics à 263 °C et à 271 °C est de 9:1, ce qui indique qu'environ 90 % des éléments Bi sont encore à l'échelle nanométrique. La capacité d'absorption de chaleur évaluée par l'enthalpie du processus de fusion est de 0,38 J g^{-1}, proche de la valeur attendue

basée sur la composition chimique (0,47 J g^{-1}). les courbes DSC sont restées inchangées après 15 cycles de chauffage-refroidissement entre 20 et 300 °C, ce qui montre la bonne stabilité au cyclage du matériaux.

Le nanocomposite Bi-Al présente trois pics endothermiques à 262, 269 et 271 °C au chauffage, et déplacés vers une température plus élevée par rapport au Bi@SiO_2-Al, ce qui implique la coalescence progressive des nanoparticules en particules massives pendant le cyclage sans la coquille de SiO_2.

Par rapport au composite Bi-Al préparé par métallurgie des poudres dans la littérature,[6] la distribution des températures de fusion pour Bi@SiO_2-Al préparé par notre procédé de métallurgie liquide est plus large et décalée vers des températures plus basses. Cela démontre une diminution de la taille des particules de Bi obtenue par notre protocole. La petite taille initiale des nanoparticules, l'enveloppe protectrice en silice, et le chauffage rapide par le four en induction sont les points clés pour obtenir des petites inclusions avec une large gamme de température de transition, ce qui est un avantage considérable pour l'application finale.

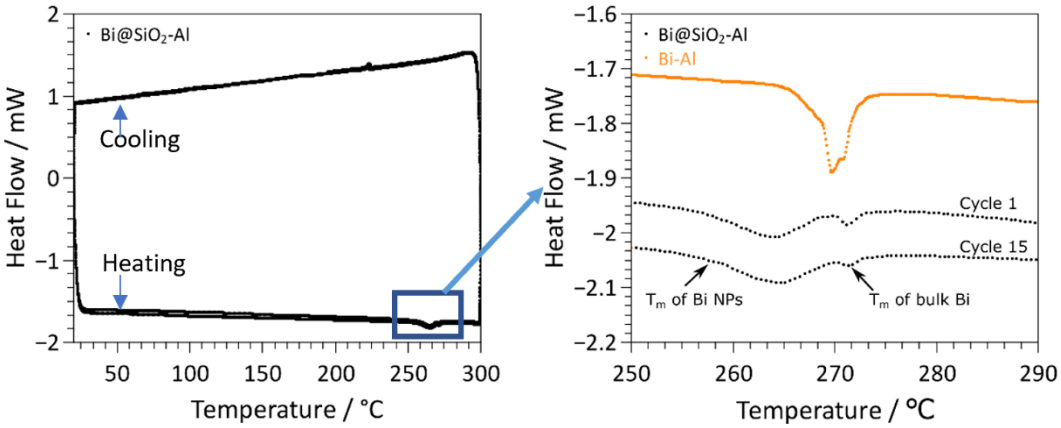

Figure 4. Analyse DSC des nanocomposites Bi@SiO_2-Al (gauche) avec aggrandissement d'une zone au chauffage (droite) pour les 1er et 15e cycles. Anaylse DSC (droite, courbe orange) pour un composite de reference Bi-Al.

Nous avons ainsi étudié plusieurs méthodes de fabrication *in situ* de Bi/Al_2O_3/Al par la métallurgie liquide assistée par ultrasons. La formation d'inclusions encapsulées par

aluminoréduction est difficilement applicable à d'autres types d'inclusions comme In/Al_2O_3/Al : les conditions de réaction doivent être ajustées en fonction du potentiel redox de l'oxyde métallique. En outre, il est difficile d'atteindre une autre température de transition de phase avec une inclusion d'alliage métallique par la voie de la co-réduction des oxydes.

Notre concept de nanocomposite métal/SiO_2-Al, sans nécessité de passer par le processus de réduction, ouvre la voie à l'obtention de nanocomposites à matrices métalliques avec d'autres nanoparticules en inclusions, notamment des nanoparticules d'alliage métallique qui ne sont pas miscibles avec l'aluminium liquide. Ces matériaux fonctionnels à base d'aluminium présentent une capacité de dissipation de la chaleur relativement importante pour cette classe de matériaux, une température de transition de phase réglable et un faible coût de fabrication. Ils peuvent servir de modèle pertinent pour le contrôle thermique des appareils électriques.

Conclusion

Plusieurs méthodes de dispersion de nanoparticules dans des matrices métalliques ont été développées. En particulier, des expériences ont été réalisées en faisant varier les paramètres tels que la puissance d'ultrason, le temps de traitement et la température de chauffage. Ainsi, les conditions optimales du processus d'incorporation ont pu être identifiées. Ce travail permet d'établir un protocole pour l'obtention de nanocomposites en utilisant des approches en voie liquide. En particulier, un nouveau dispositif d'ultrasons a été mis en place pour l'amélioration de la dispersion de nanoparticules dans les matrices métalliques tout en évitant les contaminations.

Concernant la fabrication et la caractérisation des propriétés mécaniques sur les nanocomposites contenant des inclusions de SiC et de HfB_2, les tests de nanoindentation et de microindentation ont permis de quantifier la dureté aux échelles microscopique et macroscopique. Une hétérogénéité des propriétés mécaniques a été observée sur les échantillons à matrices aluminium avec des nanoparticules de HfB_2 et de SiC. Si nous avons pu mettre en évidence une augmentation significative de la dureté par rapport à la matrice seule, des efforts sont encore nécessaires pour améliorer la dispersion et atteindre des propriétés mécaniques comparables avec la littérature en utilisant d'autres protocoles plus coûteux.[1]

En outre, nous avons développé avec succès une synthèse de nanocomposites métalliques à changement de phase par la métallurgie liquide assistée par ultrasons. Les nanoparticules à changement de phase ont été incorporées dans une coquille de silice, qui agit comme une barrière contre la coalescence des cœurs fondus pendant le processus d'incorporation.

Des mesures de propriétés d'absorption de chaleur sont réalisées pour les composites Bi@SiO_2-Al et Bi-Al. Ces études révèlent la diminution du point de fusion avec la réduction de la taille des inclusions dans l'échantillon Bi@SiO_2/Al. Ce résultat a aussi confirmé que la couche de silice permet de protéger partiellement les particules de bismuth de la coalescence lors du traitement d'ultrason dans l'aluminium fondu.

Ces matériaux restent néanmoins des preuves de concept encourageant en vue de l'élaboration de matériaux légers et fonctionnels pour le monde de l'automobile. Les nanocomposites des borures décrits pourront être amélioré pour renforcer l'alliage de l'Al. Grâce à l'adaptabilité du procédé de synthèse des Bi@SiO_2-Al, des matériaux sur mesure pourraient être crées pour la gestion thermique des pièces électriques ou électroniques.

Références

1. Casati, R. & Vedani, M. Metal Matrix Composites Reinforced by Nano-Particles—A Review. 65–83 (2014) doi:10.3390/met4010065.
2. Prasad Reddy, A., Vamsi Krishna, P., Narasimha Rao, R. & Murthy, N. V. Silicon Carbide Reinforced Aluminium Metal Matrix Nano Composites-A Review. *Mater. Today Proc.* **4**, 3959–3971 (2017).
3. Firestein, K. L. *et al.* High-strength aluminum-based composites reinforced with BN, AlB_2 and AlN particles fabricated via reactive spark plasma sintering of Al-BN powder mixtures. *Mater. Sci. Eng. A* **681**, 1–9 (2017).
4. Xie, C. *et al.* Stable and hard hafnium borides: A first-principles study. *J. Appl. Phys.* **125**, (2019).
5. Li, W. Q., Qu, Z. G., He, Y. L. & Tao, Y. B. Experimental study of a passive thermal management system for high-powered lithium ion batteries using porous metal foam saturated with phase change materials. *J. Power Sources* **255**, 9–15 (2014).
6. Abraham, A., Schoenitz, M. & Dreizin, E. L. Energy storage materials with oxide-encapsulated inclusions of low melting metal. *Acta Mater.* **107**, 254–260 (2016).
7. Mohanty, P., Mahapatra, R., Padhi, P., Ramana, C. H. V. V. & Mishra, D. K. Ultrasonic cavitation: An approach to synthesize uniformly dispersed metal matrix nanocomposites—A review. *Nano-Structures and Nano-Objects* **23**, 100475 (2020).
8. Portehault, D. *et al.* A General Solution Route toward Metal Boride Nanocrystals. *Angew. Chemie* **123**, 3320–3323 (2011).
9. Klement W, Willens RH, D. P. No TNon-crystalline structure in solidified gold–silicon alloys. itle. *Nature* **187(4740)**, 869–70 (1960).
10. Scheele, M. *et al.* Synthesis and thermoelectric characterization of Bi2Te 3 nanoparticles. *Adv. Funct. Mater.* **19**, 3476–3483 (2009).
11. STOBER, W. Sagittal plane spinal mobility is associated with dynamic balance ability of community-dwelling elderly people. *J. Colloid Interface Sci.* **26**, 62–69 (1968).
12. Manasijević, D. *et al.* Experimental investigation and thermodynamic prediction of the Al–Bi–In phase diagram. *J. Alloys Compd.* **687**, 969–975 (2016).

Nanoparticules dans des matrices métalliques pour des applications en automobiles

Résumé

Ce travail porte sur l'élaboration de nanocomposites à matrices métalliques pour des applications automobiles. Le procédé de fabrication repose sur la dispersion de nanoparticules ayant des capacités de renforcement ou d'absorption de chaleur dans un métal par métallurgie liquide. Après une étude bibliographique pour situer le sujet, le manuscrit porte d'abord sur l'élaboration des nanoparticules comme briques élémentaires, en particulier des particules cœur-coquille $Bi@SiO_2$ à bas point de fusion. Ensuite, plusieurs méthodes sont étudiées pour trouver les meilleures conditions d'incorporation des particules, qui reposent sur le couplage entre le chauffage à induction et le traitement ultrasons dans la matrice fondue. Des nanocomposites combinant des matrices à base d'aluminium et des nanoparticules de SiC ou de HfB_2 sont ainsi fabriqués pour renforcer les propriétés mécaniques. La microscopie électronique révèle la ségrégation des particules aux joints de grains. Les mesures de nanoindentation et de microindentation permettent de quantifier la dureté à l'échelle microscopique, révélant ainsi une hétérogénéité des propriétés mécaniques entre les grains et les joints de grains, plus durs en raison de leur forte concentration en particules. Enfin, des nanocomposites métalliques à changement de phase sont élaborés en dispersant dans l'aluminium les particules $Bi@SiO_2$ préalablement synthétisées. L'étude par microscopie électronique de l'interface particules/matrice met en évidence les mécanismes d'incorporation. La coquille de silice protège partiellement les particules de bismuth de la coalescence lors du traitement ultrasons, permettant un abaissement de leur point de fusion. Grâce à cette méthode, nous pourrions élargir la plage de température de transition pour obtenir une absorption progressive de la chaleur avec l'augmentation de la température des batteries.

Mots clés : [Nanocomposites, matériaux à changement de phase, propriétés thermiques]

Aluminum matrix nanocomposites for applications in automobile industry

Abstract

This PhD work is dedicated to the synthesis of metal matrix nanocomposites for automotive applications, by dispersing functional nanoparticles in an aluminum matrix by liquid metallurgy to improve mechanical and thermal regulation properties. After a bibliographic study to set the context, we describe the preparation of the initial nanoparticles as building blocks, especially core-shell $Bi@SiO_2$ nanoparticles with low melting point. Then, several dispersion methods are explored to find the best conditions for the particle's incorporation, which relies on ultrasonication in the molten matrix during induction heating. We then prepare nanocomposites combining Al-based matrices with SiC or HfB_2 nanoparticles, to improve mechanical properties. Electron microscopy study reveals segregation of the nanoparticles at grain boundaries. Nanoindentation and microindentation measurements enable the quantification of the hardness at the microscopic scale, showing a heterogeneity of mechanical properties, with higher hardness at the grain boundaries that are concentrated in nanoparticles. We then explore the fabrication of phase change nanocomposites by incorporating in aluminium the above described $Bi@SiO_2$ particles. An electron microscopy study of the Al/nanoparticle interface sheds light on reaction mechanisms during the incorporation. The silica shell partially protects the nanoparticles against coalescence during the ultrasonic treatment in molten aluminum. We then assessed the role of the inclusion size on the melting point of Bi, evidencing a decrease of the melting point with the particle size. By this method, we could then widen the phase transition temperature range to achieve progressive heat absorption with the increase of the battery temperature.

Key words: [Nanocomposites, phase change materials, thermal properties]